INFORMATION TO USERS

This manuscript has been reproduced from the microfilm master. UMI films the text directly from the original or copy submitted. Thus, some thesis and dissertation copies are in typewriter face, while others may be from any type of computer printer.

The quality of this reproduction is dependent upon the quality of the copy submitted. Broken or indistinct print, colored or poor quality illustrations and photographs, print bleedthrough, substandard margins, and improper alignment can adversely affect reproduction.

In the unlikely event that the author did not send UMI a complete manuscript and there are missing pages, these will be noted. Also, if unauthorized copyright material had to be removed, a note will indicate the deletion.

Oversize materials (e.g., maps, drawings, charts) are reproduced by sectioning the original, beginning at the upper left-hand corner and continuing from left to right in equal sections with small overlaps. Each original is also photographed in one exposure and is included in reduced form at the back of the book.

Photographs included in the original manuscript have been reproduced xerographically in this copy. Higher quality 6" x 9" black and white photographic prints are available for any photographs or illustrations appearing in this copy for an additional charge. Contact UMI directly to order.

U·M·I

University Microfilms International
A Bell & Howell Information Company
300 North Zeeb Road, Ann Arbor, MI 48106-1346 USA
313/761-4700 800/521-0600

INVESTIGATION OF ISOVECTOR GIANT RESONANCES USING THE (^{7}Li,^{7}Be) CHARGE-EXCHANGE REACTION AT 50 MeV/u

by

Thilina Nilasiya Annakkage

A dissertation submitted in partial fulfillment
of the requirements for the degree of
Doctor of Philosophy
(Physics)
in the University of Michigan
1995

Doctoral Committee:

Professor Joachim Jänecke, Chairman
Professor Frederick Becchetti
Professor Karl T. Hecht
Professor Jean P. Krisch
Professor David Wehe

To my parents, Gunasili Piyadasa and H. K. D. A. Piyadasa.

ACKNOWLEDGMENTS

Initial thanks go to my chairman, Dr. J. Jänecke for his valuable guidance and support throughout this work.

Thanks also go to Drs. N. Anantaraman, F. Becchetti, G. P. A. Berg, J. Brown, G. Crawley, S. Danczyk, K. T. Hecht, J. P. Krisch, M. Y. Lee, D. Mercer, K. Pham, D. Roberts, J. Stasko, D. Wehe, J. S. Winfield and G. H. Yoo for their support of this work.

I express thanks to my friend, Ellen Lust-Okar for proofreading this thesis.

Special thanks to my parents, Gunasili Piyadasa and H. K. D. A. Piyadasa and my brothers, Udaya Annakkage and Sepala Annakkage for their support and encouragement throughout my academic carrier.

This research was supported in part by the National Science Foundation Grant PHY-9208468.

TABLE OF CONTENTS

LIST OF FIGURES

LIST OF TABLES

Table

CHAPTER 1

INTRODUCTION

Nuclear physics is a challenging field with many unsolved questions and problems. The obstacle to answering these questions lies in two facts: (a) the fundamental force law is complicated; it is based on quark-quark interactions, but elementary particle theory has so far not provided an expression; (b) the nucleus is a complicated many-body system, for which it is not possible to find an exact solution. Different models have been developed which successfully explain some but not all of the nuclear properties. The present work describes an investigation of certain collective properties of this many-body system involving the collective motion of nucleons inside nuclei.

One of the simplest models to explain nuclear properties is the liquid-drop model suggested by C. V. Weiszäcker in 1935 [Weiszäcker, 1935]. In this model, the size, mass and binding energy of a nucleus is assumed to resemble a liquid drop. The volume of the nucleus is proportional to the number of nucleons, and the binding energy is approximately proportional to the mass of all the nucleons. The nucleons are not treated individually, rather the effect of individual nucleons are averaged over the nucleus. This model successfully explains the average binding energy per nucleon. However, it does not explain the observed so-called neutron and proton magic numbers of nuclei. Although the shell-model explains the magic numbers, it can not explain the average binding energy per nucleon.

In the shell-model, nucleons are assumed to move in an average harmonic oscillator potential. In 1949 M. Mayer [Mayer, 1948, 1949, 1950] and J. Jensen [Haxel, 1949, 1950] independently proposed that in addition to the harmonic oscillator potential a nuclear

interaction of orbital angular momentum and spin (**l.s**) can account for the observed magic numbers. The energy levels of the harmonic oscillator are split due to the nuclear spin-orbit interactions. The shift in level order when a spin-orbit potential is added to a central force harmonic oscillator potential is shown in figure 1.1.

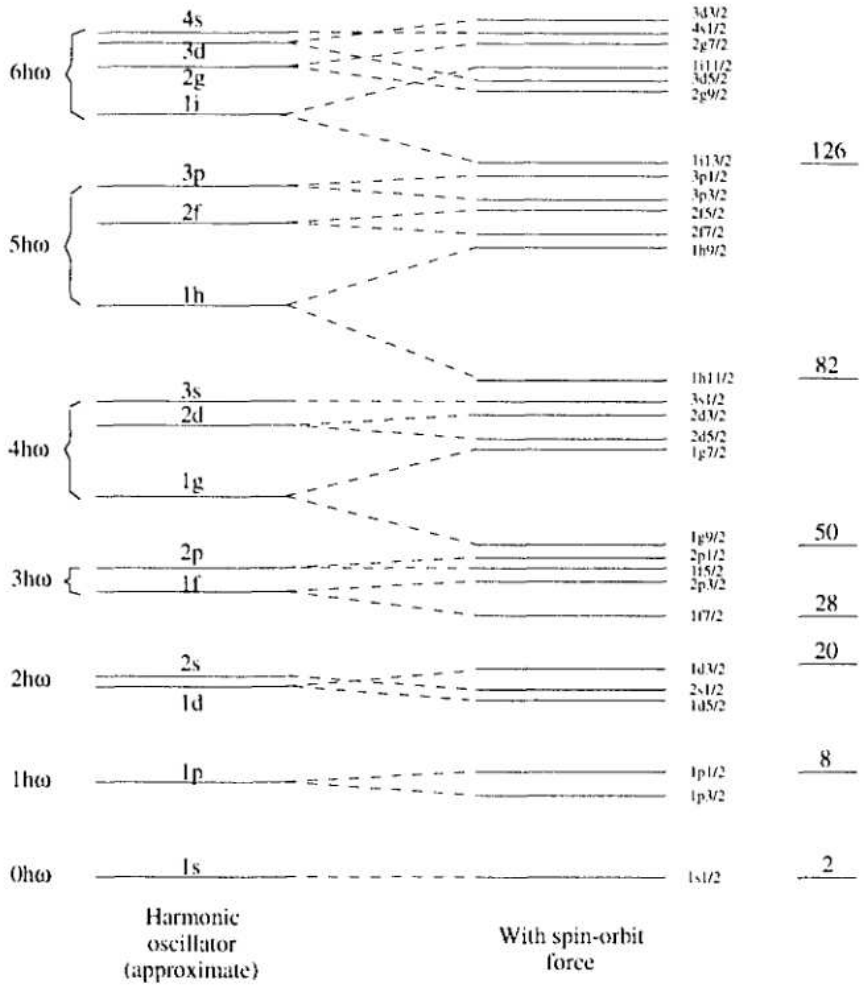

Figure 1.1 The shift in level order when a spin-orbit potential is added to a central harmonic oscillator potential.

In spherically symmetric nuclei, where only one or few valence protons or neutrons fill orbits above the major shell, low-lying states are obtained by single-particle excitations where one proton or one neutron is excited into a higher-energy orbit within the same major shell. In nuclei where only one or a few protons or neutrons are missing

before a major shell is filled, the low-lying states are obtained by single-hole excitations where the holes are filled by one proton or neutron from a lower shell within the same major shell. These low-lying excited states are discrete. Figure 1.2 gives a schematic representation of single-particle and single-hole excitations of a nucleus.

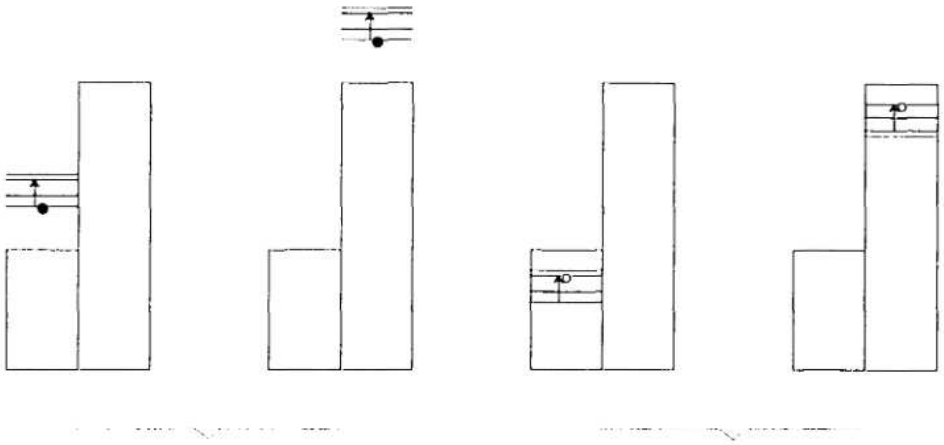

Figure 1.2 A schematic representation of single-particle and single-hole excitations in a hypothetical neutron-rich nucleus.

Nuclei which have many neutrons and protons outside a major shell are usually deformed, and the states of low excitation energies are based on rotational and also vibrational motions.

At higher excitation energies one observes giant resonances which are highly collective modes of nuclear excitations. They can be described macroscopically as collective vibrations of shape and density of a nucleus with small amplitudes and high frequencies. The frequencies of these oscillations are in the order of 10^{21} Hz, and the amplitudes are a fraction of 1 fm. Alternatively, they can be represented microscopically as a coherent superposition of many particle-hole excitations. Various types of giant resonances have been observed in most of the nuclei presented in the nuclide chart. The excitation energies and the energy widths of giant resonances varies relatively smoothly

with nuclear mass number for each class of giant resonances. Figure 1.3 shows typical features of excited states of a nucleus.

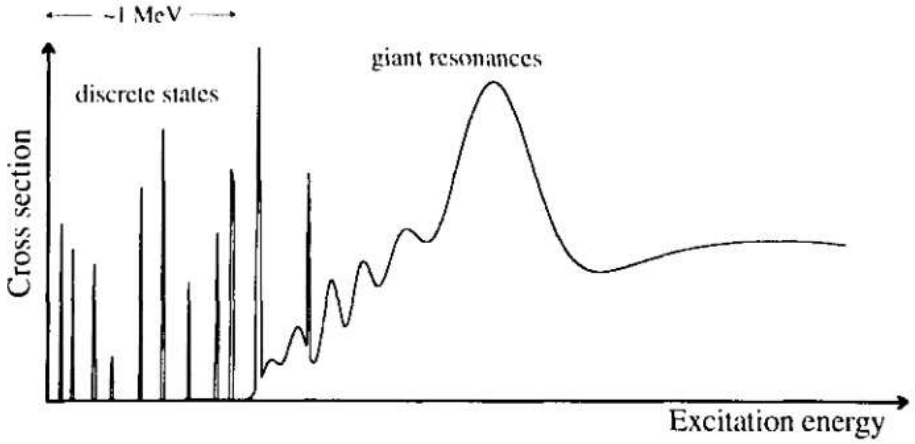

Figure 1.3 Typical features of excited states of a nucleus.

Giant resonances can be classified according to their spin and isospin characteristics: electric ($\Delta S=0$) , magnetic ($\Delta S=1$) , isoscalar ($\Delta T=0$) and isovector ($\Delta T=1$) resonances, where $\Delta S = 0$ and 1 denote non-spin-flip and spin-flip resonances, respectively, and $\Delta T = 0$ and 1 denote non-isospin-flip (isoscalar) and isospin-flip (isovector), respectively. Isovector resonances are also called charge-exchange resonances. Therefore, there are four main types of giant resonances: electric isoscalar ($\Delta S=0,\Delta T=0$) , electric isovector ($\Delta S=0,\Delta T=1$) , magnetic isoscalar ($\Delta S=1,\Delta T=0$) and magnetic isovector ($\Delta S=1,\Delta T=1$) resonances. A further classification requires the use of the angular momentum L with L=0 (monopole), L=1 (dipole), L=2 (quadrupole) and so on.

In 1947 Baldwin and Klaiber [Baldwin, 1947, 1948] discovered the first giant resonance thereby opening up a new research field in nuclear physics. This resonance was the giant dipole resonance with $\Delta S=0$, $\Delta T=1$ and L=1 observed in photo-nuclear reactions (γ,n). The next giant resonance found in 1971 in inelastic electron scattering [Pitthan,

1971] and proton scattering [Lewis, 1972] experiments, was the isoscalar giant quadrupole resonance with $\Delta S=0$, $\Delta T=0$ and $L=2$. Then, in 1977 Harakeh et al. [Harakeh, 1977] and Youngblood et al. [Youngblood, 1977, 1978] observed the isoscalar giant monopole resonance with $\Delta S=0$, $\Delta T=0$ and $L=0$. The isovector Gamow-Teller resonance with $\Delta S=1$, $\Delta T=1$ and $L=0$, was discovered in 1980 in (p,n) charge-exchange reactions at E=200 MeV [Goodman, 1980, 1981]. Several other resonances have been observed in the meantime in various reactions and extensive data have been accumulated. Most of these investigations are for isoscalar resonances, mostly from inelastic scattering, and for isovector resonances, mostly from (p,n)-type reactions, leading to proton-rich nuclei. Less information is available for isovector giant resonances of neutron-rich nuclei. This is due to the limited availability of beams for (n,p)-type reactions.

The study of giant resonances enhances the understanding of the role of the degrees of freedom for protons and neutrons in the collective motions in nuclei. Isovector giant resonances in neutron-rich nuclei from (^{7}Li,^{7}Be) charge-exchange reactions were investigated in the present work using a special particle - γ coincidence method, a method which was introduced earlier by S. Nakayama et al. [Nakayama, 1992]. The (^{7}Li,^{7}Be) reaction leads to residual nuclei on the neutron-rich side of the stable nuclei. The (^{7}Li,^{7}Be) charge-exchange reaction is a useful spectroscopic tool to investigate the isovector giant resonances for several reasons: (a) ^{7}Li and ^{7}Be are mirror nuclei; they therefore have identical intrinsic configuration; (b) the first excited state of ^{7}Be at 0.429 MeV is the only particle stable excited state, and the high-lying states decay by the emission of ^{3}He, α and protons; the 0.429 MeV state has the mean lifetime of 192 ± 25 fsec [Ajzenberg-Selove, 1988] and decays only by emission of γ-rays; (c) the (^{7}Li,^{7}Be) reactions selectively excite isovector resonances with $\Delta T_z=+1$.

The ^{7}Li and ^{7}Be ground states have spin and parity of $3/2^-$. The ^{7}Be first excited state has spin and parity of $1/2^-$. Therefore, the transition to the ^{7}Be first excited state, ^{7}Li ->^{7}Be$_{ex}$, is a pure spin-flip transition, while the transition to the ^{7}Be ground state, ^{7}Li

->$^{7}Be_{gs}$, has both spin-flip and non-spin-flip contributions. Hence the spin-flip and the non-spin-flip components of transitions can be decomposed by detecting separately transitions to the ground state and the excited state. This can be achieved by measuring ^{7}Be in coincidence with the 0.43MeV γ-rays from the deexcitation of the ^{7}Be first excited state.

A sequence of accelerator experiments has been performed using a beam of $^{7}Li^{+3}$ projectiles of 350 MeV (50 MeV/u) from the K1200 cyclotron at the National Superconducting Cyclotron Laboratory at the Michigan State University. The outgoing particles were analyzed with the S320 magnetic spectrograph [Winfield, 1992] or the A1200 beam analyzer and fragment separator [Winfield, 1994], and the 0.43 MeV γ-rays were detected by an array of 12 Bismuth Germanate (BGO) detectors close to the target (see chapter 4). The main components of the present thesis work include: (a) the construction and calibration of the γ-detector array; (b) setting up the electronics and the data acquisition system; (c) the execution of the experiments; (d) the off-line data reduction; (e) the interpretation and discussion of the results.

This thesis is organized as follows. The properties of giant resonances are discussed in chapter 2. A review of known isovector giant resonances is given in chapter 3. The experimental procedures including properties of the S320 magnetic spectrograph, the γ-ray detection system, the particle-γ coincidence technique, and the data reduction are discussed in chapter 4. The timing and energy performance of BGO detectors are discussed in chapter 5. The results are presented in chapter 6. Theoretical consideration including the reaction mechanism are outlined in chapter 7 followed by the discussion in chapter 8. Finally, the conclusions are given in chapter 9.

CHAPTER 2

PROPERTIES OF GIANT RESONANCES

2.1 Hydrodynamic-model description of giant resonances

After the discovery of giant dipole resonances, several models have been developed to describe the properties of this resonance. The earliest theoretical descriptions of giant dipole resonances are the hydrodynamic models developed by Goldhaber and Teller [Goldhaber, 1948]. They discussed two models: (1) a non-deformed sphere of protons oscillates against a non-deformed sphere of neutrons; (2) density oscillations of a neutron fluid and a proton fluid within a common non-deformed surface. In both models, the nucleus is considered to be a two-component ideal-fluid droplet. The former model is referred to as the Goldhaber-Teller model, and the latter model, elaborated by Steinwedel and Jensen, is referred to as the Steinwedel-Jensen model [Steinwedel, 1950].

In the Goldhaber-Teller model, the nucleus is considered to consist of non-deformed, incompressible proton and neutron spheres oscillating against each other. The resonances are then modeled by oscillations of the shape of the nucleus with the restoring force which is provided by the symmetry potential trying to produce the maximum overlap between the proton and neutron distributions. The restoring force is proportional to the surface symmetry energy, and the excitation energy is therefore $E_x \propto A^{-1/6}$.

In the Steinwedel-Jensen model, the nucleus is viewed as a sphere with a fixed surface, and both the neutron and proton fluids are slightly compressible. The neutron fluid oscillates against the proton fluid inside the sphere. The resonances are oscillations of the nucleon density within the nucleus. The restoring force is proportional to the volume

symmetry energy. The excitation energy becomes $E_x \propto A^{-1/3}$. Diagrams of giant dipole oscillations in the Goldhaber-Teller model and the Steinwedel-Jensen model are shown in figure 2.1.

Goldhaber-Teller model Steinwedel-Jensen model

Figure 2.1 Schematic representation of giant dipole resonance in the Goldhaber-Teller model and the Steinwedel-Jensen model.

These two models successfully explain properties of giant dipole resonances, however they fail to explain other resonances. Subsequent researchers discovered giant resonances with different multipolarities, and the Goldhaber-Teller and the Steinwedel-Jensen models were extended to explain these resonances. The macroscopic picture of giant dipole resonances is neither a purely Goldhaber-Teller model nor a Steinwedel-Jensen model but the combination of both models.

All giant resonances can be categorized according to three features depending on their spin and isospin characteristics: non-spin flip ($\Delta S=0$), spin flip ($\Delta S=1$), isoscalar ($\Delta T=0$) and isovector ($\Delta T=1$) resonances. Thus, there are four main modes of resonances: isoscalar, non-spin-flip ($\Delta T=0$, $\Delta S=0$), isovector, non-spin-flip ($\Delta T=1$, $\Delta S=0$), isoscalar, spin-flip ($\Delta T=0$, $\Delta S=1$), and isovector, spin-flip ($\Delta T=1$, $\Delta S=1$). Each of these four modes can be further classified according to their angular momentum, L: monopole (L = 0), dipole (L = 1), quadrupole (L = 2), etc. In monopole resonances, nucleons oscillate radially inward and outward; in dipole resonances, they oscillate between two poles; and in quadrupole resonances, they oscillate between oblate and prolate shapes around spherical equilibrium shape. Monopole resonances are high energy compression modes. In isoscalar modes neutrons and protons oscillate in phase, whereas in isovector mode

neutrons and protons oscillate in opposite phase. (See figure 2.2.) Therefore, excitation energies of isovector resonances are much higher than those of the corresponding isoscalar resonances, since additional energy is needed to separate the neutrons and protons. In non-spin-flip mode, which is also known as electric, nucleons with spin up and nucleons with spin down oscillate in phase whereas in spin-flip mode (magnetic) nucleons with spin up oscillate against nucleons with spin down.

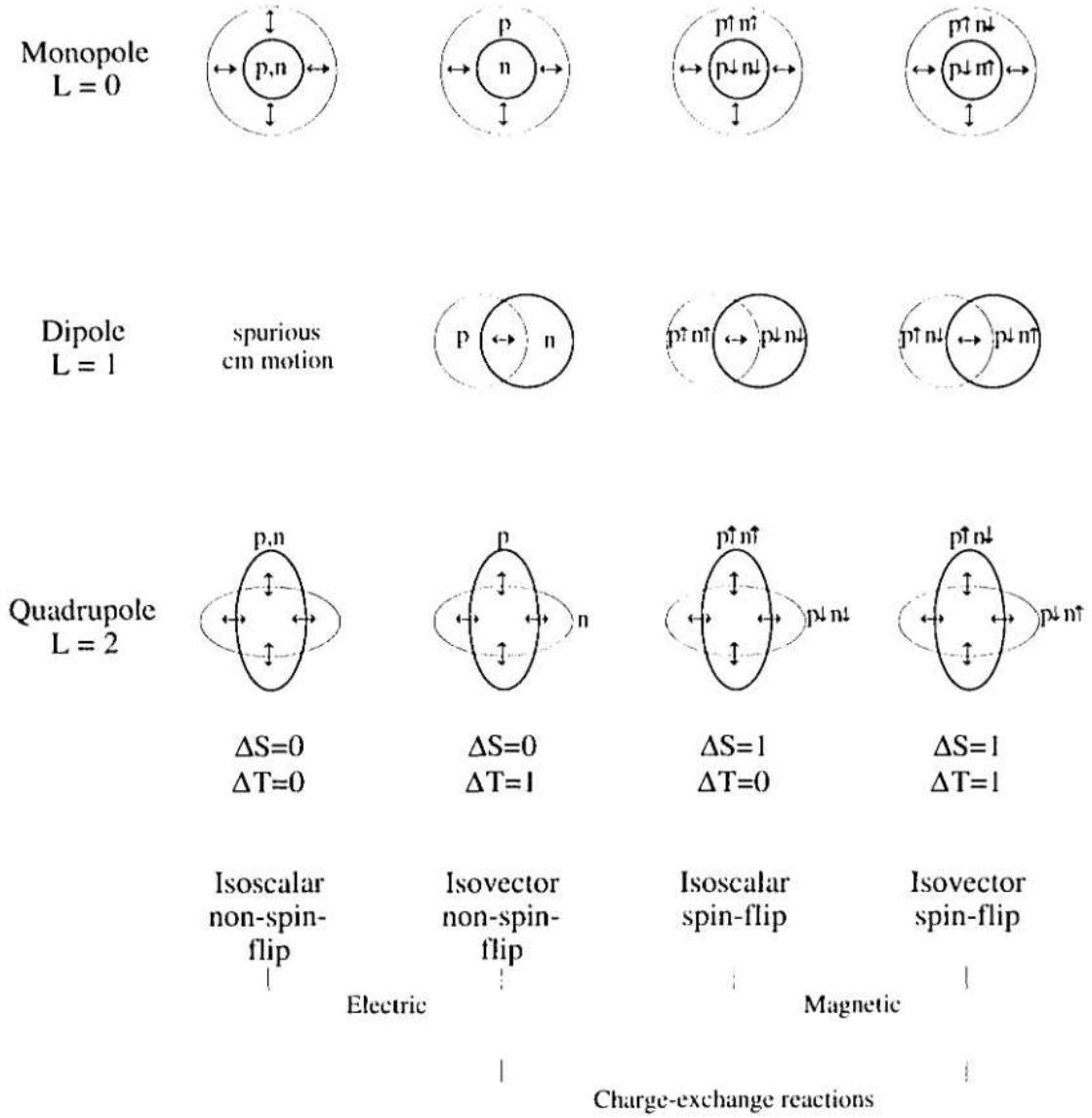

Figure 2.2 Classification of giant resonances according to their angular momentum, spin and isospin.

For example, in isovector, non-spin-flip resonances, neutrons oscillate in opposite phase with protons according to the corresponding angular momentum without any differentiation of spin. In isoscalar, spin-flip resonances, nucleons with spin up oscillate against the nucleons with spin down according to the corresponding angular momentum without any differentiation of charge. Additional so-called "soft giant resonances" have also been discussed in recent years for very light neutron "halo nuclei".

In the hydrodynamic model, the excitation energies of giant resonances depend on compression. The energy width of giant resonances due to damping is described as a viscous process. The collisions among nucleons are frequent since the nucleon mean free path is in the order of the nuclear radius. Therefore, giant resonances decay due to collisions of nucleons.

2.2 Shell-model description of giant resonances

Collective oscillations of giant resonances can also be described microscopically in terms of the shell-model. In this model, the nucleons are assumed to move in a collective harmonic oscillator potential. At low energies the nuclear excitations result from single-particle or single-hole transitions. These low-lying states are discrete. At higher energies many such single-particle and single-hole excitations coherently superpose to give rise to giant resonances.

Parity changes in giant dipole resonances, result from particle-hole transitions from one major shell to the next. Figure 2.3 gives a schematic representation of particle transitions between shell-model states. Thus, giant dipole resonances are built up of $1\hbar\omega$ transitions, and it is therefore expected to be located at the excitation energy of $\sim 41A^{-1/3}$ MeV. However, experimentally, isovector giant dipole resonances are located at $\sim 77A^{-1/3}$ MeV. This difference is due to the spin and isospin dependence of the nucleon-nucleon

interactions. In general, isoscalar, non-spin flip states are shifted down in energy and isovector, spin flip states are shifted up in energy from the expected excitation energies.

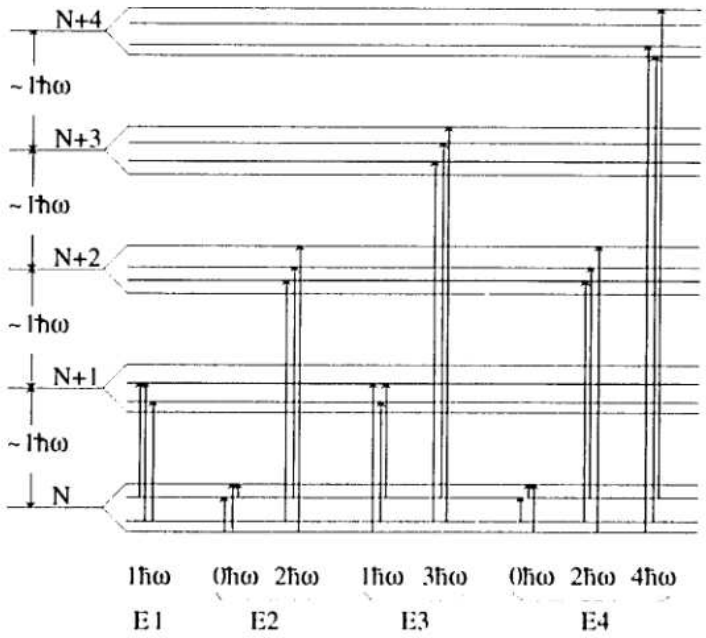

Figure 2.3 Schematic representation of electric multipole transitions between shell-model states in a hypothetical nucleus.

E2 transitions are comprised of two different components, namely those within the same major shell , $0\hbar\omega$ transitions, and those between shells N and N+2, $2\hbar\omega$ transitions. These will be shifted up or down in energy for isovector and isoscalar resonances, respectively. The $2\hbar\omega$ transitions associated with giant quadrupole resonance carry most of the energy-weighted sum rule. E3 transitions consist of $1\hbar\omega$ and $3\hbar\omega$ transitions, and E4 transitions include the $0\hbar\omega$, $2\hbar\omega$ and $4\hbar\omega$ transitions.

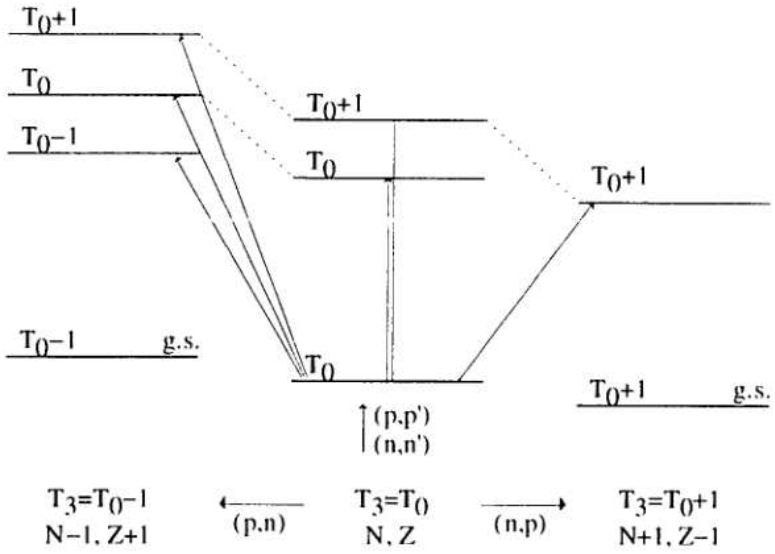

Figure 2.4 Allowed isospin transitions for isovector resonances.

Isospin transitions in nuclei are shown in figure 2.4 As shown in the figure each resonance is fragmented into different isospin components. This splitting is due to the coupling of the τ=1 isovector excitations with the $\mathbf{T}=T_0$ core, where T_0 is the ground state isospin of the target. Isoscalar resonances are not fragmented since τ=0. In these resonances the transitions occur in the same nucleus between states of the same isospin, from $\mathbf{T}=T_0 \rightarrow T_0$. In the isovector resonances transitions occur from $\mathbf{T}=T_0 \rightarrow T_0$-1 , T_0, T_0+1 and from $T_z=T_0 \rightarrow T_z=T_0$-1 , T_0, T_0+1 with T=0 to T=0 excluded. Transitions to isovector resonances from nuclei with proton numbers Z to Z-1 consist of a singlet; transitions within the same nucleus are doublets; and transitions from Z to Z+1 nuclei are triplets. Hence in (n,p) reactions, one can see only the T_0+1 component, and in (p,n) reactions, one can see the T_0+1, T_0 and T_0-1 components. The isospin splitting between the T_0 and $T_>$ components for giant dipole resonance is given by [Sterrenburg, 1980]

$$\Delta E^* = E(T+1) - E(T) \tag{2.1}$$

$$= (T+1)\left[E_v + (2T-1)E_t\right] \tag{2.2}$$

and the isospin splitting between the T_0 and $T_<$ components for giant dipole resonance is given by

$$\Delta E^{-} = E(T) - E(T-1) \tag{2.3}$$

$$= T\left[E_v - (2T+3)E_t\right] \tag{2.4}$$

where E_v and E_t are isovector and isotensor symmetry energy contributions, respectively, and $E_v \approx 60/A$ MeV.

Several experimental and theoretical investigations confirm the existence of isospin splitting. One of the earliest experiments is the photo-nuclear reaction on ^{13}C performed by J. W. Jury et al. [Jury, 1979].

Since giant resonances are located at energies higher than the particle emission threshold, they can decay predominantly via emission of charged particles or neutrons. In light nuclei they decay by emission of either charged particles or neutrons, whereas in heavier nuclei they decay preferentially by emission of neutrons due to the Coulomb barrier. γ decay is also possible, but the relative decay branching ratio ($\Gamma_\gamma / \Gamma_{total}$) is typically about 10^{-3} - 10^{-5}. The direct decay of particles from the 1p1h components of the resonance leads to a hole state in the residual nucleus. It gives rise to the escape width $\Gamma\uparrow$. Figure 2.5 shows this decay as the direct decay.

Instead of decaying directly into the hole state by emission of particles, the resonance can also decay by coupling its 1p1h components to 2p2h states, which are known as doorway states, and then to 3p3h states etc. until an equilibrium state is reached. The final equilibrium state is the compound nucleus which has the same excitation energy, spin and parity as the giant resonance. Each intermediate pre-equilibrium state can decay by particle emission. The compound nucleus decays statistically. This cascade decay gives rise to the spreading width $\Gamma\downarrow$,which consists of two terms: the pre-equilibrium decay width $\Gamma\downarrow\uparrow$ and the statistical decay width $\Gamma\downarrow\downarrow$. This is also illustrated in Figure 2.5

In the simple schematic model described above, it is assumed that all the 1p1h states couple to the doorway state. But some 1p1h states can already be fragmented, and thus

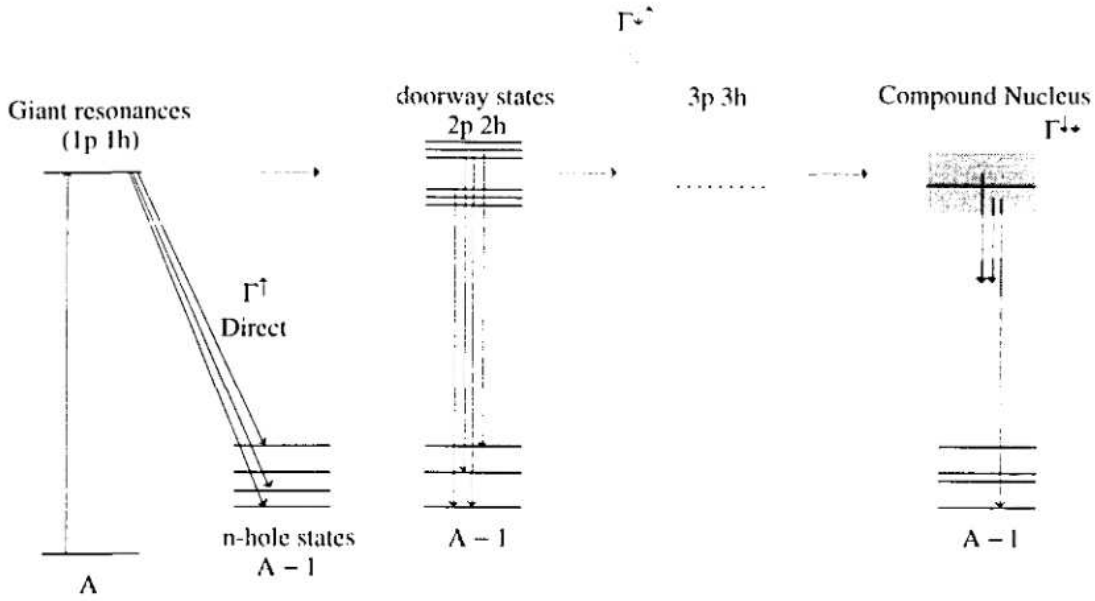

Figure 2.5 Schematic representation of various possible particle decay modes of giant resonances.

unable to couple to the doorway state. This results in Landau damping, $\Delta\Gamma$. Hence the total energy width of a giant resonance can be written as

$$\Gamma = \Gamma\uparrow + \Gamma\downarrow + \Delta\Gamma \tag{2.5}$$

where $$\Gamma\downarrow = \Gamma\downarrow\uparrow + \Gamma\downarrow\downarrow \tag{2.6}$$

The escape width, $\Gamma\uparrow$, is associated with the life time for direct neutron emission. The spreading width, $\Gamma\downarrow$, is associated with the life time for the spreading into the doorway states. The total width, Γ, can often be represented by a gaussian line shape representing the distribution of underlying 1p1h states.

CHAPTER 3

REVIEW OF KNOWN ISOVECTOR GIANT RESONANCES

3.1 Review of known isovector giant resonances observed in charge-exchange reactions to neutron-rich nuclei

Charge-exchange reactions selectively excite isovector resonances, hence they are good probes for the study of such resonances. The present work investigates isovector resonances using (^{7}Li,^{7}Be) charge-exchange reactions. In this section giant resonances observed by other authors in some of the charge-exchange reactions to neutron-rich nuclei will be summarized. The reactions include (π^-,π^0), (n,p), (^{7}Li,^{7}Be), (^{13}C,^{13}N) and (^{12}C,^{12}N). The excitation energies are given relative to the ground state of the target nuclei but actually represent excited states in the respective residual nuclei. The values in parentheses listed below and in tables 3.1(a) to 3.1(f) are the excitation energies relative to the ground states of the respective residual nuclei.

3.1.1 Pion charge-exchange reaction (π^-,π^0).

A pion charge-exchange reaction (π^-,π^0) was undertaken at Los Alamos Meson Physics Facility (LAMPF) by A. Erell et al. [Erell, 1986]. The π^- beam of 165 MeV was used to bombard ^{40}Ca , ^{60}Ni, ^{90}Zr, ^{120}Sn, ^{140}Ce and ^{208}Pb targets. Isovector giant monopole resonances have been seen in ^{40}K, ^{60}Co, ^{90}Y, ^{120}In, ^{140}La and ^{208}Tl at excitation energies of 24.1 MeV, 25.2 MeV, 22.0 MeV, 21.4 MeV, 19.9 MeV and 12.0 MeV, respectively. Giant dipole resonances have been observed in ^{40}K, ^{60}Co, ^{90}Y and ^{120}In at excitation energies of 13.8 MeV, 13.5 MeV, 10.4 MeV and 9.6 MeV, respectively.

The (π^-,π^0) reaction was also studied at bombarding energies of 120 MeV, 165 MeV and 230 MeV [Irom, 1986]. For the bombarding energy of 120 MeV, isovector monopole resonances have been seen in ^{40}K, ^{60}Co and ^{120}In at excitation energies of 27.0 MeV, 23.2 MeV and 20.6 MeV, respectively. Isovector giant dipole resonances have been observed in ^{40}K and ^{60}Co at excitation energies of 14.6 MeV and 12.4 MeV, respectively. For the bombarding energy of 165 MeV, isovector monopole resonances have been seen in ^{40}K, ^{60}Co and ^{120}In at excitation energies of 24.1 MeV, 25.2 MeV and 21.4 MeV, respectively. Isovector giant dipole resonances have been observed in ^{40}K, ^{60}Co and ^{120}In at excitation energies of 13.8 MeV, 13.5 MeV and 9.6 MeV, respectively. For the bombarding energy of 230 MeV, isovector monopole resonances have been seen in ^{40}K, ^{60}Co and ^{120}In at excitation energies of 26.1 MeV, 25.2 MeV and 21.3 MeV, respectively. Isovector giant dipole resonances have been observed in ^{40}K and ^{60}Co at excitation energies of 14.9 MeV, 13.7 MeV, respectively.

3.1.2 (n,p) reactions

Isovector, spin dipole resonances have been seen in ^{90}Zr(n,p)^{90}Y at 198 MeV [Raywood, 1990]. Four peaks have been seen at excitation energies of 15.8 (2.7) MeV, 18.6 (5.5) MeV, 23.1 (10.0) MeV and 28.6 (15.5) MeV. Here, the excitation energies relative to the final nuclei are given in parentheses. They have energy widths of 2.3 MeV, 2.6 MeV, 4.6 MeV and 3.8 MeV, respectively. Spin dipole transitions dominate in the first three peaks. The fourth peak exhibits a differential cross section which resembles qualitatively that of the isovector, spin monopole angular distribution. However, the measured angular distribution is significantly lower than the calculated one.

Isovector, spin dipole resonances, spin monopole resonances and spin quadrupole resonances were seen in ^{208}Pb(n,p)^{208}Tl reaction at 198 MeV [Moinester, 1989]. Four peaks were seen at excitation energies of ~25.6 (2.7) MeV, ~28.0 (5.1) MeV, ~31.2 (8.3) MeV and ~36.5 (13.6) MeV. The peak at 28.0 MeV has an angular distribution similar to

those of spin dipole (1^-) and spin quadrupole (2^+) distributions. The peak at 36.5 MeV has an angular distribution similar to those of spin monopole (1^+) and spin quadrupole (1^+) distributions. The peaks at 25.6 MeV and 31.2 MeV have flat angular distributions and they appear not to be associated with a single multipolarity.

Giant dipole resonances were observed in ^{6}Li(n,p)^{6}He and ^{7}Li(n,p)^{7}He reactions at 60 MeV [Brady, 1983]. Peaks were seen at excitation energies of 5.3 (1.8) MeV, 17.1 (13.6) MeV, 19.0 (15.5) MeV and 26.7 (23.2) MeV in ^{6}He. Broad peaks also were seen in ^{7}He at excitation energies of ~17 (6) MeV and ~31 (20) MeV.

3.1.3 (^{7}Li,^{7}Be) reactions

Giant dipole resonances have been observed in (^{7}Li,^{7}Be) reactions on ^{12}C and ^{28}Si at 26 MeV/A [Nakayama, 1992]. The spin-flip and non-spin-flip components of resonances were separated using the particle-γ coincidence method. (The particle - γ coincidence method will be discussed in detail in chapter 4.) In ^{12}B, a giant dipole resonance was seen at an excitation energy of ~23 (8) MeV, and evidence for an isovector giant monopole resonance and an isovector giant quadrupole resonance was seen at excitation energies of ~28 (13) MeV and ~33 (18) MeV, respectively. A spin dipole resonance was seen at excitation energy of ~ 23 (8) MeV. In ^{28}Al a giant dipole resonance was seen at the excitation energy of ~20 MeV, and evidence for isovector giant monopole and isovector giant quadrupole resonances were found at excitation energies of ~27 MeV and ~31 MeV, respectively. A spin dipole resonance was exhibited at the excitation energy of ~27 MeV.

Evidence for a soft dipole resonance was reported in ^{6}Li(^{7}Li,^{7}Be)^{6}He at 82 MeV [Sakuta, 1994]. Peaks were found at excitation energies of ~5.3 (1.8) MeV, ~9.5 (6.0) MeV, ~15.5 (12.0) MeV and ~22.5 (19.0) MeV. The peak at ~9.5 MeV with energy width ~4.8 MeV was associated with a soft dipole resonance.

The $^{90}Zr(^{7}Li,^{7}Be)^{90}Y$ reaction was studied at 78 MeV in the angular range $10^{\circ} - 28^{\circ}$ [Gareev, 1988]. Four peaks were observed at excitation energies of 14.8 (1.7) MeV, 17.7 (4.6) MeV, 21.5 (8.4) MeV and 27.9 (14.8) MeV. They have energy widths of 2.2 MeV, 3.0 MeV, 7.0 MeV and 13.9 Mev, respectively.

3.1.4 ($^{13}C,^{13}N$) reactions

The ($^{13}C,^{13}N$) reaction has been studied at 50 MeV/u on targets of ^{12}C, ^{40}Ca, $^{58,60}Ni$, ^{90}Zr, ^{120}Sn and ^{208}Pb [Berat, 1989, 1993]. Isovector giant dipole resonances have been observed in ^{12}B, ^{40}K, ^{58}Co and ^{60}Co at excitation energies of 22.8 (7.7) MeV, 19.7 (12.0) MeV, 19.0/21.2 (10.2/12.4) MeV and 20.2/22.7 (9.1/11.6) MeV respectively. They have energy widths of 1.9 MeV, 3.1 MeV, 1.9/1.5 MeV and 2.2/2.2 MeV, respectively. The dipole resonances in ^{58}Co and ^{60}Co are split into two components each. Isovector giant monopole resonances have been seen in ^{60}Co, ^{90}Y, ^{120}In and ^{208}Tl at excitation energies of 33.2 (22.1) MeV, 31.8 (18.7) MeV, 33.0 (14.7) MeV and 39.4 (16.5) MeV, respectively. They have energy widths of 8.1 MeV, 4.6 MeV, 4.1 MeV and 3.1 MeV, respectively.

The ($^{13}C,^{13}N$) reaction has also been studied at 60 MeV/u on targets of ^{12}C and ^{208}Pb [Lhenry, 1994]. Four peaks were seen in ^{12}B at excitation energies of 15.1 (0.0) MeV, 16.05 (0.95) MeV, 19.5 (4.4) and 22.8 (7.7) MeV. The peak at 22.8 (7.7) MeV was identified as the giant dipole resonance. Three peaks were seen in ^{208}Tl at excitation energies of 28.7 (5.8) MeV, 32.7 (9.8) MeV and 39.4 (16.5) MeV. The peak at 39.4 (16.5) MeV was identified as the giant monopole resonance.

3.1.5 ($^{12}C,^{12}N$) reactions

The $^{12}C(^{12}C,^{12}N)^{12}B$ reaction has been studied at 30 and 70 MeV/u [Bohlen, 1988]. At 30 MeV/u and $\theta_{lab} = 3.4^{0}$, peaks identified as 1^{+}, 2^{+}, 2^{-}, 1^{-}, 3^{-}, 2^{-}, 4^{-}, 3^{+}, 1^{-} (giant dipole resonance), and (1^{-}) were seen at the energies of 15.1 (0.0), 16.05 (0.95),

16.77 (1.67), 17.72 (2.62), 18.49 (3.39), 19.47 (4.37), 19.62 (4.52), 20.76 (5.66), 22.87 (7.77) and 25.55 (10.45) MeV, respectively. At 70 MeV/u and $\theta_{lab} = 1.3^0$, peaks identified as 1^+, 2^+, 2^-, 1^-,0^+, 3^-, 2^+, 2^-, 4^-,1^+ and 1^- (giant dipole resonance) were seen at energies of 15.1 (0.0) MeV, 16.05 (0.95) MeV, 16.77 (1.67) MeV, 17.72 (2.62) MeV, 17.82 (2.72) MeV, 18.49 (3.39) MeV, 18.86 (3.76) MeV, 19.47 (4.37) MeV, 19.62 (4.52) MeV, 20.1 (5.0) MeV and 22.87 (7.77) MeV, respectively.

3.2 Energy considerations

The giant resonances observed in the various reactions discussed above are summarized in the tables 3.1 (a) to 3.1(f). The excitation energies in MeV given in these tables are relative to the ground states of the target nuclei. The values in parentheses are the excitation energies (E_X) in MeV relative to the residual nuclei, and the values in curly brackets are the energy widths in MeV. The excitation energies in the target nuclei are calculated from the equation

$$E_x^{target} = E_x + E_x(IAS; T_Z = T_0). \tag{3.1}$$

Here, E_x^{target} are the excitation energies relative to the targets, E_X are the excitation energies in the residual nuclei, and $E_x(IAS; T_Z = T_0)$ are the excitation energies of the isobaric analog states (IAS) in the target nuclei. If known experimentally [Antony, 1988], these values for E_X(IAS) should be used. Otherwise, they can be calculated with an uncertainty of ±200 keV from the Coulomb energy equation and known ground state mass excesses from

$$E_x(IAS; T_Z = T_0) = \Delta M(T_Z = T_0 + 1) - \Delta M(T_Z = T_0) + \Delta M(H) - \Delta M(n) + \Delta E_{Coul.} \tag{3.2}$$

$$\text{with } \Delta E_{Coul.} = \frac{1.389 Z_c - 2.041}{A^{1/3}} MeV. \tag{3.3}$$

It should be noted that the calculated energies reported by Auerbach and Klein [Auerbach, 1983, 1984] do not represent E_x or E_x^{target}. However, they are simply related to E_x by the equations

$$E_x^{AK} = E_x + \Delta M(T_Z = T_0 + 1) - \Delta M(T_Z = T_0) \tag{3.4}$$

$$= E_x^{target} - (\Delta E_{Coul.} - \Delta M(n) + \Delta M(H)). \tag{3.5}$$

Similar equations hold for the values reported by the authors for proton-rich nuclei.

	(π^-,π^0) [c]	$(^7Li,^7Be)$ [h]	$(^{13}C,^{13}N)$ [b]	Theory [a]
^{12}C		~28 (13){3.5}		
^{28}Si		~27.0		
		(16.3){3.5}		
^{40}Ca	24.1			32.3 (24.7)
	(16.5){21.6}			
^{48}Ca				38.9 (20.9)
^{60}Ni	25.2 (14.1)		33.2	34.2 (23.1)
	{14.7}		(22.1){8.1}	
^{90}Zr	22.0		31.8	33.7 (20.6)
	(8.9){15.0}		(18.7){4.6}	
^{120}Sn	21.4 (3.1){9.2}		33.0	35.4 (17.1)
			(14.7){4.1}	
^{140}Ce	19.9 (2.1){8.5}			35.8 (18.0)
^{208}Pb	12.0 {11.6}		39.4	34.2 (11.3)
			(16.5){3.1}	

Table 3.1(a) Isovector giant monopole resonances with excitation energies in MeV relative to the respective target nuclei. Excitation energies relative to the residual nuclei are given in parentheses. Experimental energy widths are given in curly brackets.

References:

[a] [Auerbach, 1983, 1984]

[b] [Berat, 1989, 1993]

[c] [Bohlen, 1988]

[d] [Brady, 1983]

[e] [Erell, 1986]

[f] [Gareev, 1988]

[g] [Moinester, 1989] [h] [Nakayama, 1992]

[i] [Raywood, 1990]

	(π^-,π^0) [e]	(n,p) [d]	(^{7}Li,^{7}Be) [h]	(^{12}C,^{12}N) [c]	(^{13}C,^{13}N) [b]	Theory [a]
^{6}Li		17.1(13.6)				
		19.0 (15.5)				
^{7}Li		31 (20)				
^{12}C			22.7	22.8 (7.7)	22.8	
			(7.6){4.0}		(7.7){1.9}	
^{28}Si			~20.0			
			(9.3){4.0}			
^{40}Ca	13.8				19.7	19.3 (11.7)
	(6.2){5.7}				(12.1){3.1}	
^{48}Ca						23.3 (5.3)
^{58}Ni					19.0	
					(8.7){1.9}	
					21.2	
					(10.9)1.5}	
^{60}Ni	13.5 (2.4)				20.2	20.2 (9.1)
	{4.2}				(9.1){2.2}	
					22.7	
					(11.6){2.2}	
^{90}Zr	10.4 {2.7}					19.0 (5.9)
^{120}Sn	9.6 {0.0}					19.5 (1.2)
^{140}Ce						19.5 (1.2)
^{208}Pb						24.8 (1.9)

Table 3.1(b) Isovector giant dipole resonances. (See Table 3.1(a) caption).

	(^{7}Li,^{7}Be) [h]	Theory [a]
^{12}C	~33 (18){3.5}	
^{28}Si	~31.0	
	(20.3){4.0}	
^{40}Ca		31.4 (23.8)
^{48}Ca		35.8 (17.8)
^{60}Ni		32.1 (21.0)
^{90}Zr		30.4 (17.3)
^{120}Sn		31.0 (12.7)
^{140}Ce		31.6 (13.8)
^{208}Pb		30.0 (7.1)

Table 3.1(c) Isovector giant quadrupole resonances. (See Table 3.1(a) caption).

	(n,p) [i]	(n,p) [g]	Theory [a]
^{60}Ni			35.0 (23.9)
^{90}Zr	28.6		33.1 (20.0)
	(15.5){3.8}		
^{208}Pb		36.5	35.6 (12.7)
		(13.6){9.0}	

Table 3.1(d) Spin monopole resonances. (See Table 3.1(a) caption).

	(n,p) [i]	(n,p) [g]	(^{7}Li,^{7}Be) [h]	Theory [a]	Jπ
^{12}C			~23 (8){4.0}		
^{28}Si			~20.0		
			(9.3){4.0}		
^{60}Ni				35.2 (24.1)	0$^-$
				29.9 (18.8)	1$^-$
				18.9 (7.8)	2$^-$
^{90}Zr	15.8 (2.7){2.3}			39.0 (25.9)	0$^-$
	18.6 (5.5){2.6}			34.5 (21.4)	1$^-$
	23.1(10.0){4.6}			23.5 (10.4)	2$^-$
^{208}Pb		28.0 (5.1){2.8}		37.1 (14.2)	0$^-$
				38.1 (15.2)	1$^-$
				29.7 (6.8)	2$^-$

Table 3.1(e) Spin dipole resonances. (See Table 3.1(a) caption).

	(n,p) [g]	Theory [a]	Jπ
^{60}Ni		37.8 (26.7)	1$^+$
		31.7 (20.6)	2$^+$
		25.3 (14.2)	3$^+$
^{90}Zr		33.7 (20.6)	1$^+$
		30.6 (17.5)	2$^+$
		25.4 (12.3)	3$^+$
^{208}Pb	36.5(13.6){9.0}	38.1 (15.2)	1$^+$
	28.0 (5.1){2.8}	31.7 (8.8)	2$^+$
		31.2 (8.3)	3$^+$

Table 3.1(f) Spin quadrupole resonances. (See Table 3.1(a) caption).

In the present work, the (^{7}Li,^{7}Be) and (^{7}Li,^{7}Be γ) reactions at 350 MeV were studied for the targets of ^{6}Li, ^{12}C, ^{90}Zr, ^{120}Sn and ^{208}Pb. The giant resonances observed will be discussed below together with the results.

CHAPTER 4

EXPERIMENTAL PROCEDURES AND DATA REDUCTION

The present work investigates the (^{7}Li,^{7}Be) charge-exchange reactions. The $^7Li^{+3}$ beam is produced by the K1200 cyclotron at the National Superconducting Cyclotron Laboratory at Michigan State University. Part of the data were taken in December 1992 (experiment #92030) and part of the data were taken in November 1993 (experiment #93018-1) and January 1994 (experiment #93018-2). The outgoing particles in experiments #92030 and #93018-2 were analyzed with the S320 magnetic spectrograph. In the experiment #93018-1, the outgoing particles were analyzed with the A1200 fragment separator and beam analyzer.

4.1 The S320 spectrograph

4.1.1 Mechanical layout

The S320 spectrograph consists of two quadrupole, a dipole, an octupole and a sextupole magnets (QQDMS). The K parameter of this spectrograph is 320 where K is defined by the equation

$$\frac{E}{A} = K\left(\frac{q}{A}\right)^2. \tag{4.1}$$

Here, E is the energy, A is the mass, and q is the charge state of the particles. The major components of the spectrograph are shown in the figure 4.1 [Winfield, 1992].

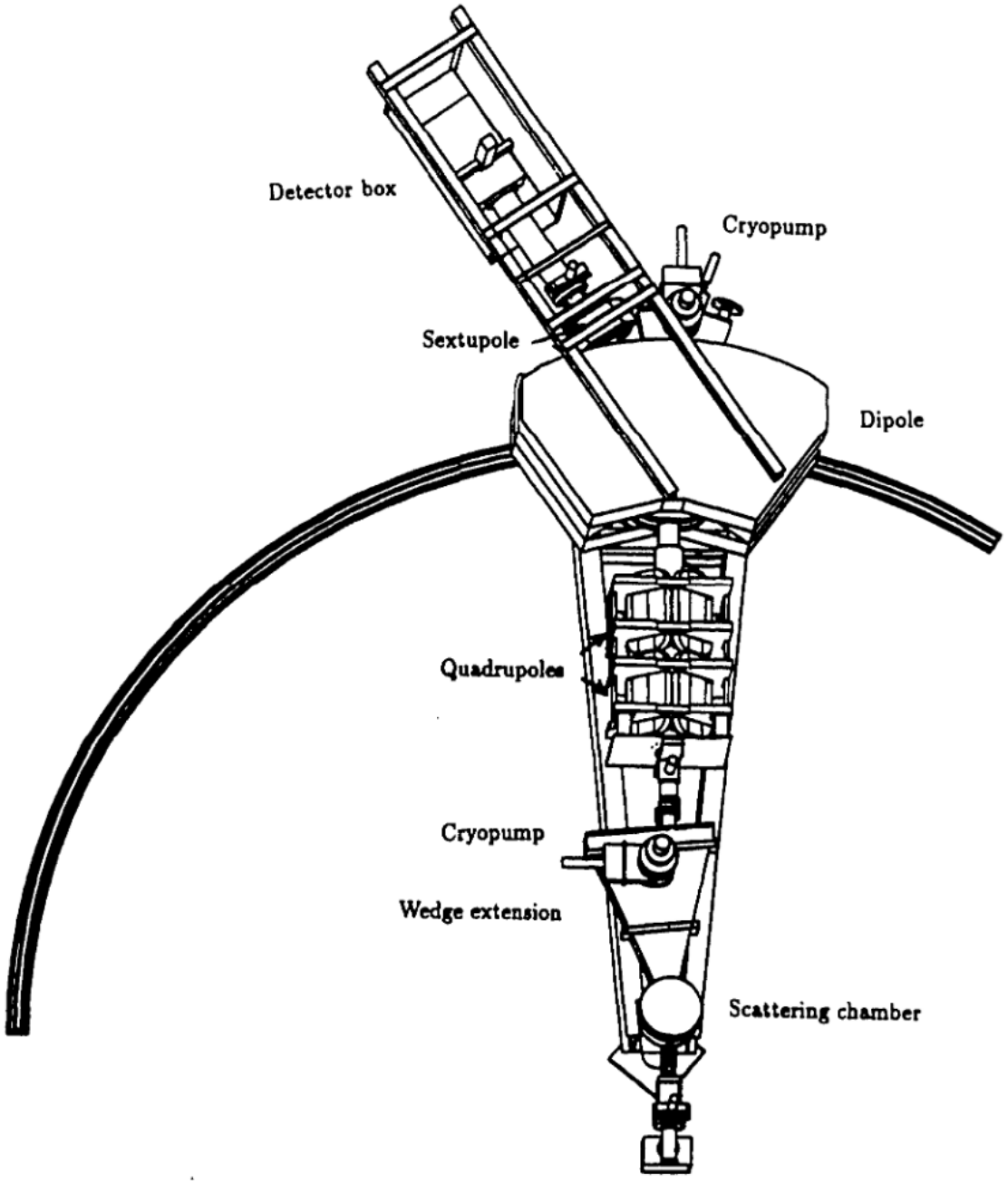

Figure 4.1 The S320 Spectrograph.

The spectrograph covers an angular range from -5 degrees to 55 degrees. The targets are mounted in a scattering chamber with inside diameter of 39 cm and an inner height of 15 cm. This provides a maximum solid angle for coincidence measurements of about 120 msr. The scattering chamber is connected to the incoming beam tube with a

sliding seal. The lower part of the target chamber rotates with the spectrograph, and the upper part and the lid is braced to a wall of the vault and does not move. The target ladder is mounted at the center of the chamber from below. The target frames of 2" x 1.125" are mounted on the ladder by sliding down the rail. A scintillator is mounted at the upper end of the ladder tilted by 45 degrees to view the beam. The target positions are controlled by moving the target ladder vertically. This can be done locally or remotely from the Data-U. The target ladder can be rotated locally by a motor underneath the chamber or remotely from the Data-U and can hold up to five targets and the scintillator.

The entrance aperture of the spectrograph is located at a distance of 196.5 cm from the target. The aperture ladder can hold up to four apertures. The position and the angle of the aperture ladder can also be controlled locally or remotely from the Data-U. The lid of the scattering chamber is designed to hold 12 BGO detectors at a distance of 6.4 cm from the target. The γ detection system will be discussed in detail in section 4.2. A wedge-shaped aluminium chamber of length about 130 cm and height 12.5 cm, as shown in fig. 4.1, is connected to the scattering chamber. This chamber contains a rectangular aluminium box 49 cm long. The target chamber and the rectangular box is connected via a 2" diameter pipe. The other end of the box is attached to a 9" diameter pipe. There are two ports on the exit flange of the 9" diameter pipe one at 0 degree and the other at 5 degree. The port at 0 degree is used for small angle measurements and the port at 5 degree is used for large angle measurements. Top and side views of the scattering chamber are shown in figure 4.2 [Winfield, 1992]. The Faraday cup is usually mounted at the 0 degree port.

The targets are usually transferred to the scattering chamber in an argon atmosphere. The targets used in the experiment #92030 were self-supporting ^{6}Li, ^{12}C, ^{90}Zr, ^{120}Sn, ^{208}Pb and C_8H_8 (polystyrene) with thicknesses 2.0, 2.4, 3.1, 2.8, 3.1 and 2.3 mg/cm^2, respectively. In the experiment #93018-1, self-supporting targets of ^{6}Li,^{12}C and C_8H_8 with thicknesses 2.6, 3.0 and 2.3 mg/cm^2, respectively were used. In the

experiment #93018-2, the targets used were self-supporting ^{6}Li, ^{12}C and C_8H_8 with thicknesses 2.5, 3.0 and 0.906 mg/cm^2, respectively.

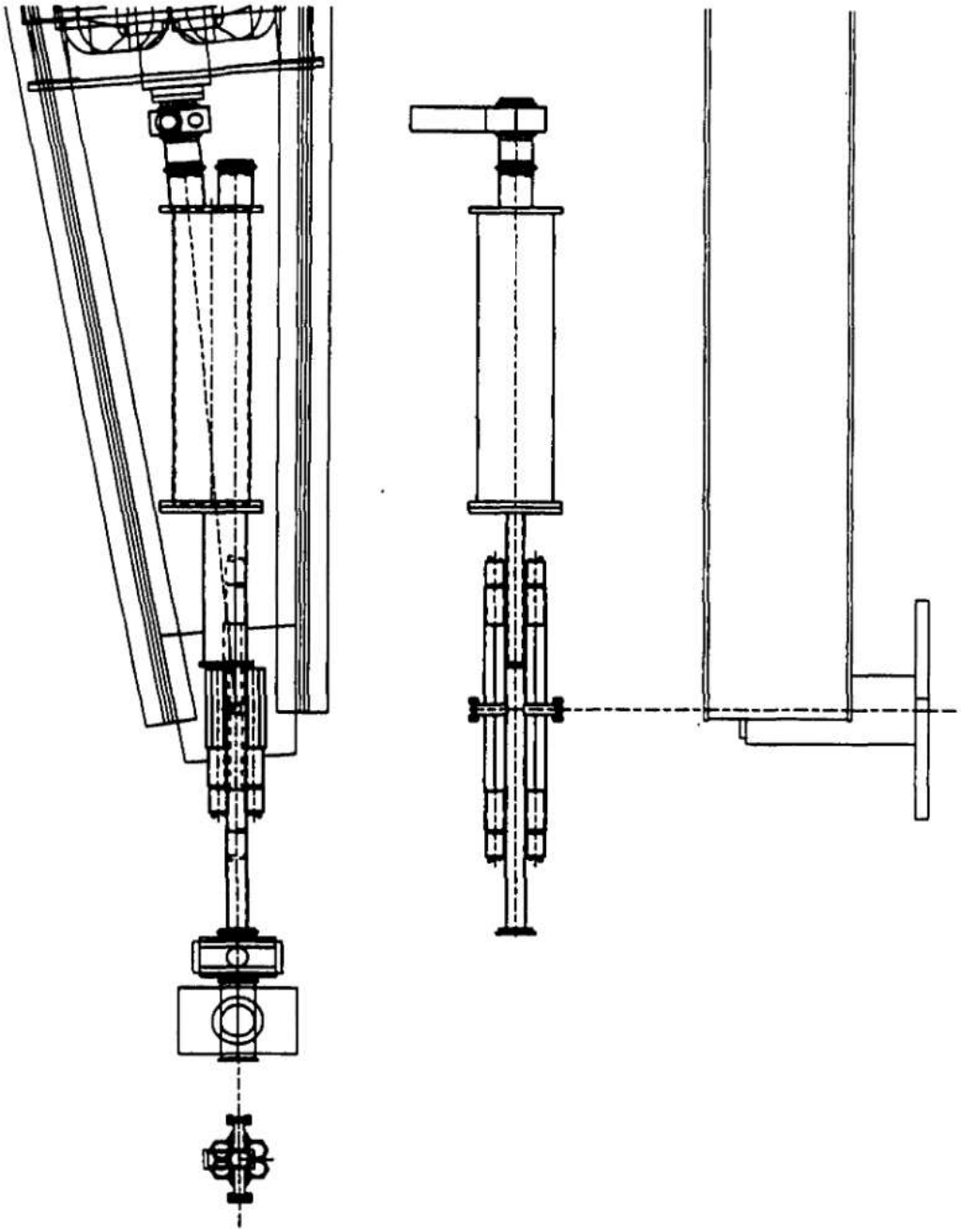

Figure 4.2 The top and the side views of the scattering chamber

4.1.2 Focal plane detection system

The focal plane detectors are located in the detector box shown in figure 4.1. The focal plane detection system consists of position sensitive single-wire proportional counters (SWPC), ion chambers and scintillators. There are two operating modes of the detector system: the light ion configuration and heavy ion configuration. In the light-ion configuration, the particles are transmitted through the ion chambers and stopped at the scintillator. In the heavy-ion configuration, the particles are stopped at the ion chambers. The present work uses the light-ion configuration.

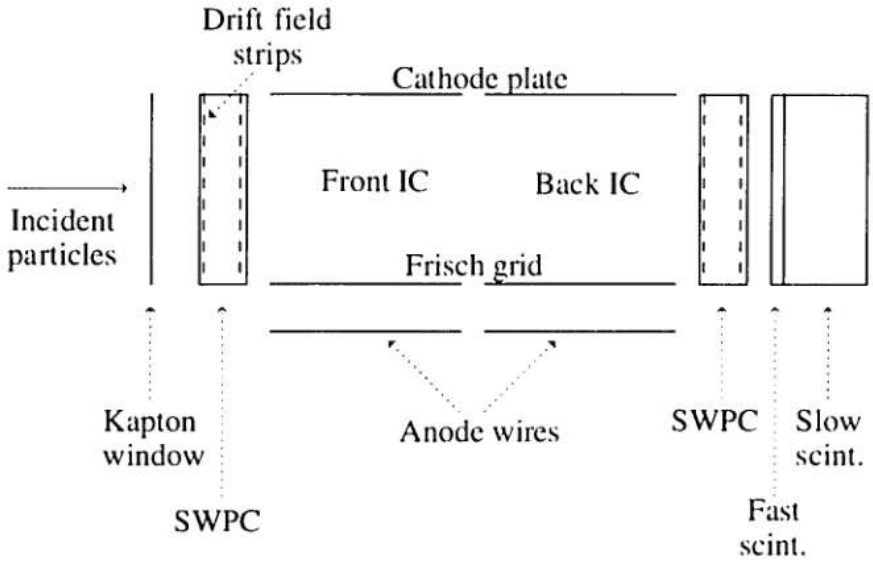

Figure 4.3 Schematic diagram of S320 focal plane detector system in light-ion configuration.

The light ion configuration has five units: a SWPC followed by two ion chambers followed by another SWPC and a scintillator. The ion chamber gives the energy loss and the scintillator gives the residual energy of the particles. The detectors are filled with isobutane. All these detectors are operated in the same gas volume. Figure 4.3 shows a schematic layout of the focal plane detector system in the light ion mode. The x position is calculated by using the charge division method as follows.

Suppose a particle of charge Q hits the SWPC at distance x from left and suppose l is the length of the wire.

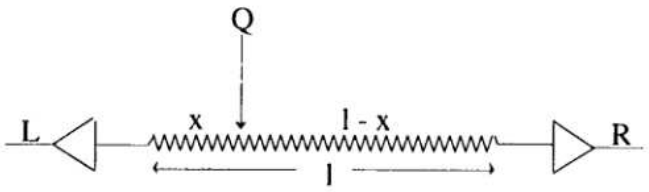

Figure 4.4 Schematic diagram of a SWPC.

If the left signal is given by

$$L = \frac{Qx}{l} \tag{4.2}$$

and the right signal is given by

$$R = \frac{Q(l-x)}{l}, \tag{4.3}$$

then

$$x = \frac{lL}{L+R}. \tag{4.4}$$

The angle of incidence is calculated from the positions on the front and back SWPC and the distance between them. The average energy loss in the front and back ion chambers is taken as the energy loss of the particles. The scintillator consists of a 0.51 mm thick fast plastic scintillator (NE104) and a 10 cm thick slow plastic scintillator (BC444). The total energy of a particle is approximately proportional to the sum of the pulse height signals from the fast and slow scintillators. The S320 events are defined by the presence of a fast signal from the first scintillator.

4.1.3 Optics and magnet settings of S320 spectrograph

The S320 medium-resolution magnetic spectrograph consists of five magnets: two quadrupole magnets, a dipole magnet, an octupole magnet and a sextupole magnet. The field directions of the magnets are shown schematically in figure 4.5.

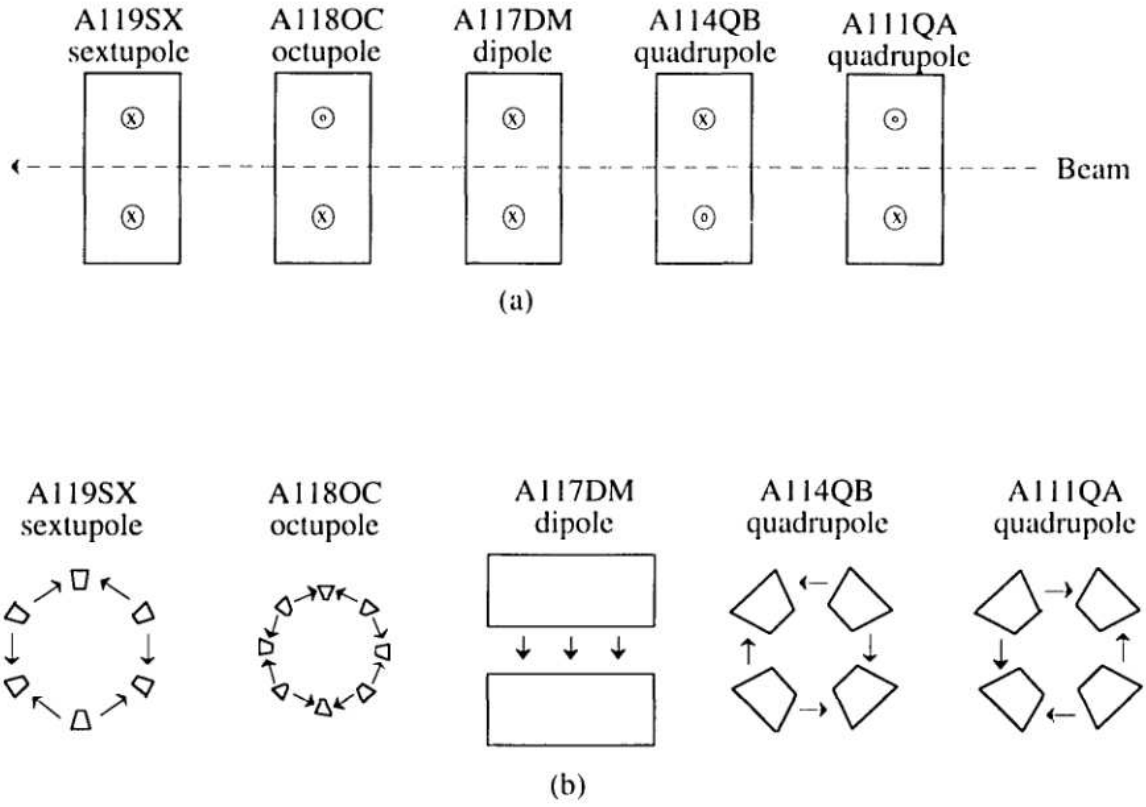

Figure 4.5 Field directions of S320 magnets: (a) side view; (b) as seen by the beam.

The settings of the magnets are obtained by running the program S320 in Nscl_Library:[Setup.S320]. This program makes use of the established characteristics of the system and the results of ray tracing calculations. A sample of magnet settings used in experiment 92030 is given in table 4.1. The table 4.2 summarizes the important optical and magnetic parameters of S320 QQDMS spectrograph.

magnet	Current (A)	Field (KG)
A111QA y quadrupole	163.77	
A114QB x quadrupole	129.42	
A117DM dipole	190.39	10.097
A118OC octupole	48.41	
A119SX sextupole	54.24	

Table 4.1 Sample of S320 magnet settings.

4.2 Particle - γ coincidence technique and γ detection system

The 0.43 MeV γ-rays from the deexcitation of the first excited state of ^{7}Be are detected with an array of 12 BGO detectors. The BGO detectors used in the present work consist of Bismuth Germanate (BGO) crystals of 3/4" dia. x 2" optically coupled to the Hamamatsu photomultiplier tubes of R1213 or R1166 (high gain variant of the R1213) with E974-13 Hamamatsu bases. Each photomultiplier tube is wrapped with two layers of μ-metal and two layers of soft iron to shield from the magnetic field. The cathode luminous sensitivity, the anode dark current, and the cathode blue sensitivity of the R1213 photomultiplier tubes are about ~100 μA/lm, ~2 nA, and ~10 μA/lm, respectively, and those of the R1166 photomultiplier tubes are ~100 μA/lm, ~0.5 nA, and ~10 μA/lm, respectively. Both types of photomultiplier tubes have bialkali photocathodes with maximum radiant sensitivity of about 90 mA/W at the wavelength 400 nm. The scintillation emission maximum of the BGO is situated at the wavelength of about 490 nm. This difference between the BGO scintillator emission maximum and the photomultiplier spectral sensitivity could be reduced by using a wavelength shifter or a photomultiplier tube

with a different photocathode material. This could increase the BGO output signal and should slightly improve the energy resolution. The surfaces of both ends of the scintillator are polished, and the curved surface is roughened and covered with Teflon tape for diffuse light reflection. The BGO is a high-Z material with a density of 7.13 g/cm^3. This makes it a very efficient detector for γ-rays. The decay time of the BGO output signal is about 300 ns. The photofraction at 430 keV is about 60%.

The lid of the scattering chamber is designed to hold 12 BGO detectors, with the central axis at a distance of 6.4 cm from the target. The detector array is mounted inside a semi-circular opening in the lid. The geometry is shown in the figure 4.6. Two blocks of Cu and four blocks of Pb were used as shields against the γ-rays and the neutrons from the beam stop. The 12 detectors have a total photopeak detection efficiency for the 430 keV γ-rays of about 12% for this geometry.

Dispersion, D	= 1.6 cm
Magnification, M_x	= -0.67
M_y	= -2.5
Beam spot on target	0.5 mm coherent width
	3 mm tall, dispersion matched
	2.4 mm dispersed beam width for 0.1% energy spread
Maximum solid angle $\Delta\theta$	= 12 mr
$\Delta\phi$	= 12 mr
Ω	= 0.67 msr
Range,$(E_{max} - E_{min})/E$	= 20%
Focal plane	Normal incidence, 18 cm long x 2.6 cm tall
Bend angle	= 34.4 degree
Maximum rigidity, $B\rho_{max}$	= 2.57 Tm at 1.47 T
ρ_{max}	= 1.75 m
Central ray radius, ρ_{mean}	= 1.7 m
Calculated line width, $\Delta E/E$	= 0.1%
Distance from target to aperture	= 196.5 cm
Distance from target to focal plane	= 675 cm
Distance from target to back scintillator	= 712 cm

Table 4.2 Parameters of the QQDMS S320 spectrograph [Winfield, 1992].

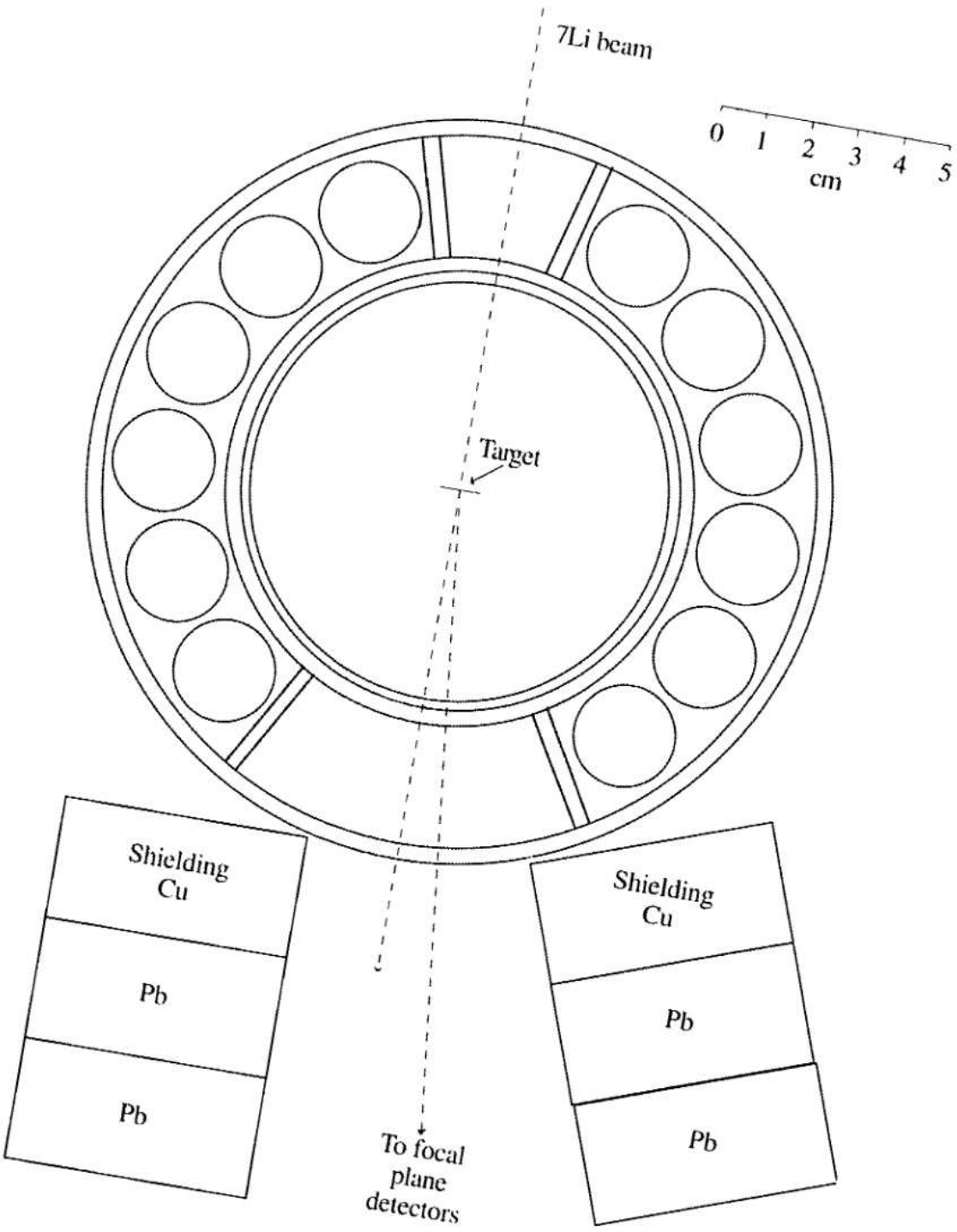

Figure 4.6 The BGO detector array.

4.3 Electronics setup

The electronics setup for signal processing and data acquisition is located in the "Data-U" area. The signals from the focal plane detectors and BGO detectors are routed to the patch panel in the Data-U through RG213 or RG59 cables. A LeCroy 1440 multichannel high voltage power supply was used to supply the high voltage for the BGO detectors and the focal plane detectors. The voltage settings were controlled remotely from the Data-U. The signal from each BGO detector was connected to an amplifier located in the vault. One of the outputs of the amplifiers was used for the energy information, and the other output was used for the timing information of the γ events. The time of flight of the ^{7}Be was measured relative to the beam burst (RF) of the cyclotron. The first RF signal which arrives in coincidence with the focal plane event trigger will generate a logic signal, the master gate, of about 300 ns width. This will trigger the time-to-digital converter (TDC) for the BGO detectors. The γ event signals will be delayed such that they arrive near the middle of the master gate to make the best use of the full range of the TDC. The delayed γ events, which occur in coincidence with the master gate, will generate a logic signal which will then be fanned out to a scaler, a bit register, the TDC, and the master coincidence which is a logic fan-in-fan-out (FI-FO). The signal from the master coincidence will strobe the charge-to-digital converters (QDC) for the BGO detectors. The signal from the coincidence unit for focal plane events and the RF make a coincidence with the computer-not-busy signal which is produced by the front-end processor to generate the event trigger and the bit-register strobe. The event trigger is sent to the CAMAC (Computer Automated Measurement And Control) programmable gate generator, LeCroy 2323, to trigger the computer. The bit-register strobe, delayed by about 100 ns, triggers the data acquisition system.

4.3.1 The electronics setup for the experiment #92030

A schematic electronics setup used in the experiment #92030 is shown in the figure 4.7. The figures 4.8 (a), (b), (c), (d) and (e) show the detailed electronics setups. The signals from each BGO detector is amplified by a spectroscopy amplifier, TC241S. This amplifier generates a fast and a slow output signal. The fast signal was used for timing information and the slow signal, delayed by 400 ns, was fed to an analog-to-digital converter (ADC) for the energy information. Two "BaF_2" delay boxes in series were used to generate the 400 ns delay. The fast signal had about 30 ns rise-time. The coincidence level of the logic unit PS754 (see figure 4.8 (c)) was set to 1 when BGO singles were to be measured, and it was set to 2 when BGO events in coincidence with focal plane events were to be measured.

4.3.2 The electronics setup for the experiment #93018-part 1

A schematic electronics setup is shown in the figure 4.9. The figures 4.10 (a), (b) and (c) show the detailed electronics setups. The electronics setup is similar to that of the previous experiment, #92030, with some minor modifications. In the previous experiment, the BGO energies were measured with an ADC, using the slow, integrated signal from the spectroscopy amplifier, TC241S. As a result, pile-up of γ events were seen in the BGO energy spectra. The pile-up rate is about 6%, when the BGO detectors are running at a rate of about 10000 events/sec. One needs a fast signal to reduce the pile-up γ events. Therefore, TC241S amplifiers were replaced by the MSU fast amplifiers, and consequently the ADCs were replaced by charge-to-digital converters (QDC), LeCroy 2249W. The strobe for the QDC was taken from the master coincidence, whereas in the previous experiment, the strobe for ADC was taken from the logic FI-FO after the coincidence of anti-NIM with the master coincidence. The BGO signal from the fast amplifier had a rise-time of about 8 ns, and the decay-time was about 200 ns. The

decaying signal displayed fluctuations. These fluctuations arise from the emission of single photoelectrons from the photocathode of the photomultiplier tube. The timing properties of BGO (see chapter 5) are discussed in detail in reference [Annakkage, 1994]. As a result the signals from the lower-level and upper-level constant fraction discriminators (CFD) had several after-pulses. Two delay and gate generators (D&GG), 21*6691, were used as vetoes to eliminate these after-pulses. The delay and the width of the upper-level D&GG were 0 ns and 2000 ns, respectively, and those of the lower-level D&GG were 130 ns and 2000 ns, respectively.

4.3.3 The electronics setup for the experiment #93018-part 2

A schematic electronics setup and the detailed electronics setups are shown in figures 4.11, 4.12 (a), (b) and (c). The electronics setup is almost the same as that used in the previous experiment with few changes. The BGO output signal for the QDC is taken from the fast amplifier, while the timing signal is further amplified by the TC241S amplifier. The TC241S is used to integrate and differentiate the signal. The integration and differentiation time constants were 20 ns.

4.4 The data acquisition system

The NSCL data acquisition system consists of two components: the MASH system (VME "front-end") [Fox, 1989] and the VAX/VMS data flow architecture [Fox, 1985]. The data are read from the CAMAC modules by the VME front-end (Motorola 6800) using the event readout program. The event readout program describes how and when each event is read. This program can be generated by the program generator. The program generator can also be used to create CAMAC crate definition, bit-register definition, scaler input definition, and scaler display definition.

To generate the CAMAC crate definition file, the user needs to describe which CAMAC modules are in which slots of the crate and which names are given to each input

of each module. For bit register definition, the user determines which input will be the readout for each bit in the bit-register. Both crate definition and bit-register definition are contained in a file with the extension x.cra. To generate a scaler definition file, the user needs to define the names for each input of the scaler modules. The scaler definitions are contained in a file with the extension x.sca.

The event readout program reads the data from CAMAC modules and stores them in blocks called event buffers. The data acquired from the front-end is distributed to the back-end programs by a program called router. The back-end programs which receive the on-line data are called consumers. The router acquires event buffers into a shared memory and sends buffer notification messages to each consumer. Since several consumers, such as 8 mm magnetic tapes, the data analysis program XSYS [XSYS, 1988], and scaler display program, are sharing a single copy of a buffer, the data is accessed read-only.

The on-line data are analyzed by the XSYS Event Analysis Language code (EVAL). This program reads the events from the event buffers and stores them in memory locations called user buffers and increment appropriate histograms.

4.5 Calibration programs

There are several calibration programs available in the directory Nscl_Library. The program Calib can be used to predict the channel numbers of the energy spectrum given the excitation energy of the residual nucleus or the kinetic energy of the ejectile or alternatively, to produce a list of excitation energies of the residual particle against channel number of the energy spectrum. This program can be found in the directory Nscl_Library:[Setup.Calib]. The user has to generate an input file which should contain the calibration information such as the focal plane position for a given magnetic field. The execution code is Cal88. A sample input file can be found in Nscl_Library:[Setup.Calib].

The program S320 can be used to run kinematics of any given reaction. This program can be found in the directory Nscl_Library:[Setup.S320]. It can also be used to

calculate the energy losses in the scintillator and in the ion chambers and hence to predict the particle identification.

4.6 Data reduction

The on-line data are recorded on 8 mm magnetic tapes. In the off-line data reduction, the events are analyzed with the software program XSYS events analysis language code (EVAL) [XSYS, 1988]. The particle identification is performed by setting two-dimensional software gates on several spectra: (1) the energy loss signal in the scintillator (E) versus that in the ion chamber (ΔE); (2) the ΔE versus the time of flight (TOF) of ^{7}Be particles; (3) the E versus TOF; (4) the focal plane position versus TOF.

The events recorded in the BGO detectors in coincidence with the ^{7}Be particles consist of primarily γ-rays, but also of a few neutrons and other particles. The prompt γ-ray events are separated from neutrons and other particles by setting a one-dimensional software gate on the time-of-flight spectra of the BGO signals. The random γ-ray events which are also recorded (see chapter 5) are obtained by setting a second gate, a repetition time of the cyclotron beam burst away from the prompt gate. The random events, the events in the second gate, are then subtracted from the events in the prompt γ-burst which yields true coincidence events. The prompt γ-burst contains not only the γ events, but also some fast neutrons since the BGO detectors are somewhat sensitive to neutrons [Häusser, 1983]. Since they are only 6.4 cm away from the target, fast neutrons and γ-rays arrive almost simultaneously. A one-dimensional software gate in the energy spectrum is used to extract the events in the photopeak of the 0.43 MeV γ-rays. The neutrons and the γ-rays arising from the deexcitation of the residual nucleus are corrected for by setting a gate of the same width just above the photopeak energy. The events in the second gate are subtracted from the events in the photopeak.

The final singles and coincidence spectra of ^{7}Be particles usually display several peaks and the non-resonant quasi-free background arising from the $p_{bound}(^{7}Li,^{7}Be)n_{free}$

reaction. The peak-fitting program, OPDATA, is used to subtract the non-resonant quasi-free background and fit the peaks with gaussian distributions. The doubly differential cross section of the quasi-free background can be given by equation (4.5) [Erell, 1986],

$$\frac{d^2\sigma}{d\Omega dE} = N\frac{1-e^{-(E-E_0)/T}}{1+\left[(E-E_{qf})/W_L\right]^2}. \qquad (4.5)$$

Here, E_{qf} is the quasi-free energy, W_L is the width of the Lorentzian function, E_0 is the energy cutoff, and T is the cutoff energy scale parameter also known as the temperature. The quasi-free energy of ^{7}Be is taken as, E_{qf} = kinetic energy of ^{7}Be particles minus neutron binding energy. The quantity W_L is taken to be 32 MeV and T is taken to be 90 MeV. All the background parameters except N were kept fixed when fitting the background and the peaks. The coincidence spectra were fitted with centroid energies and widths fixed at the values from the corresponding singles spectra.

The differential cross sections of the peaks were determined from the yields under the gaussian distributions, the solid angle extended by the aperture, the target thickness, and the integrated beam current corrected for dead-time.

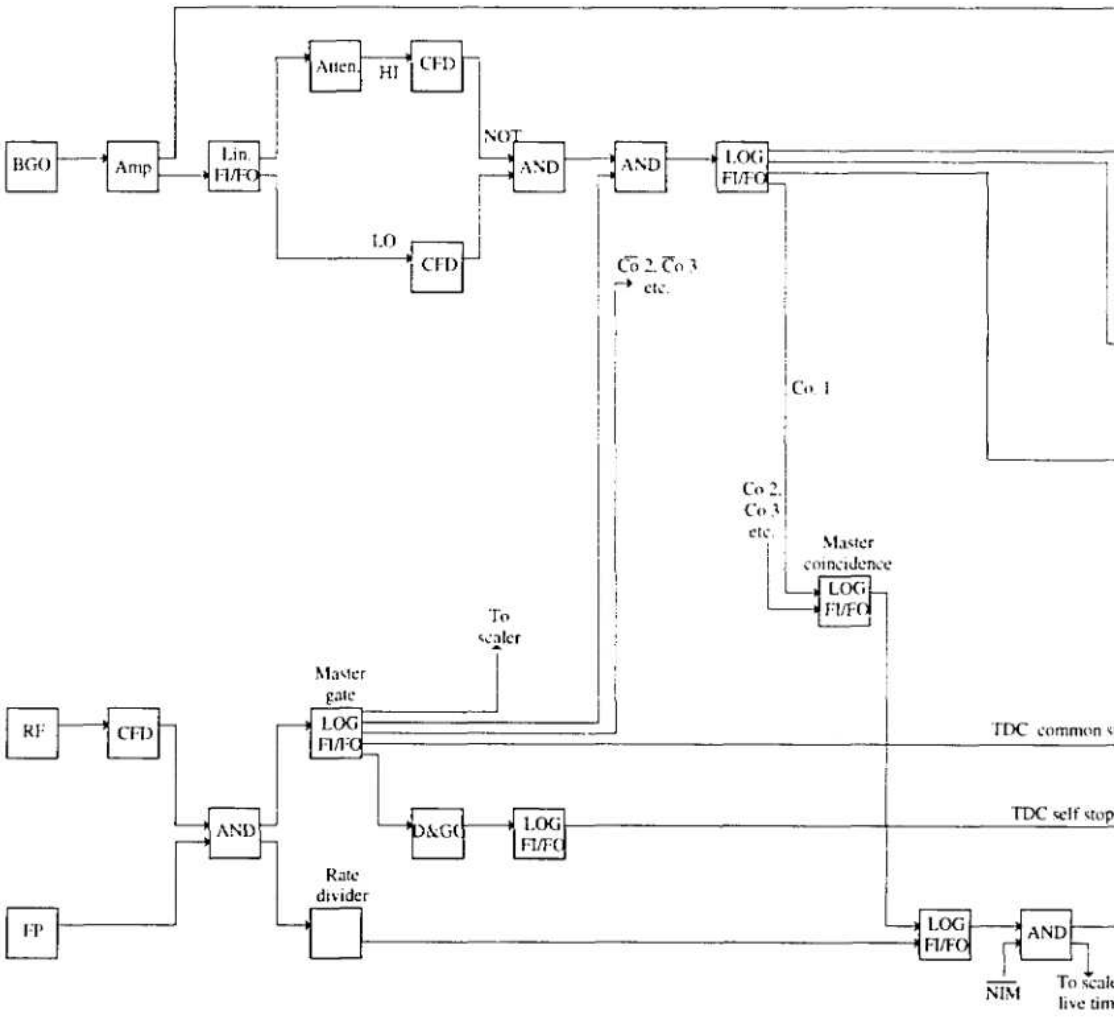

Fig. 4.7 Schematic electronics setup for expt. #92030

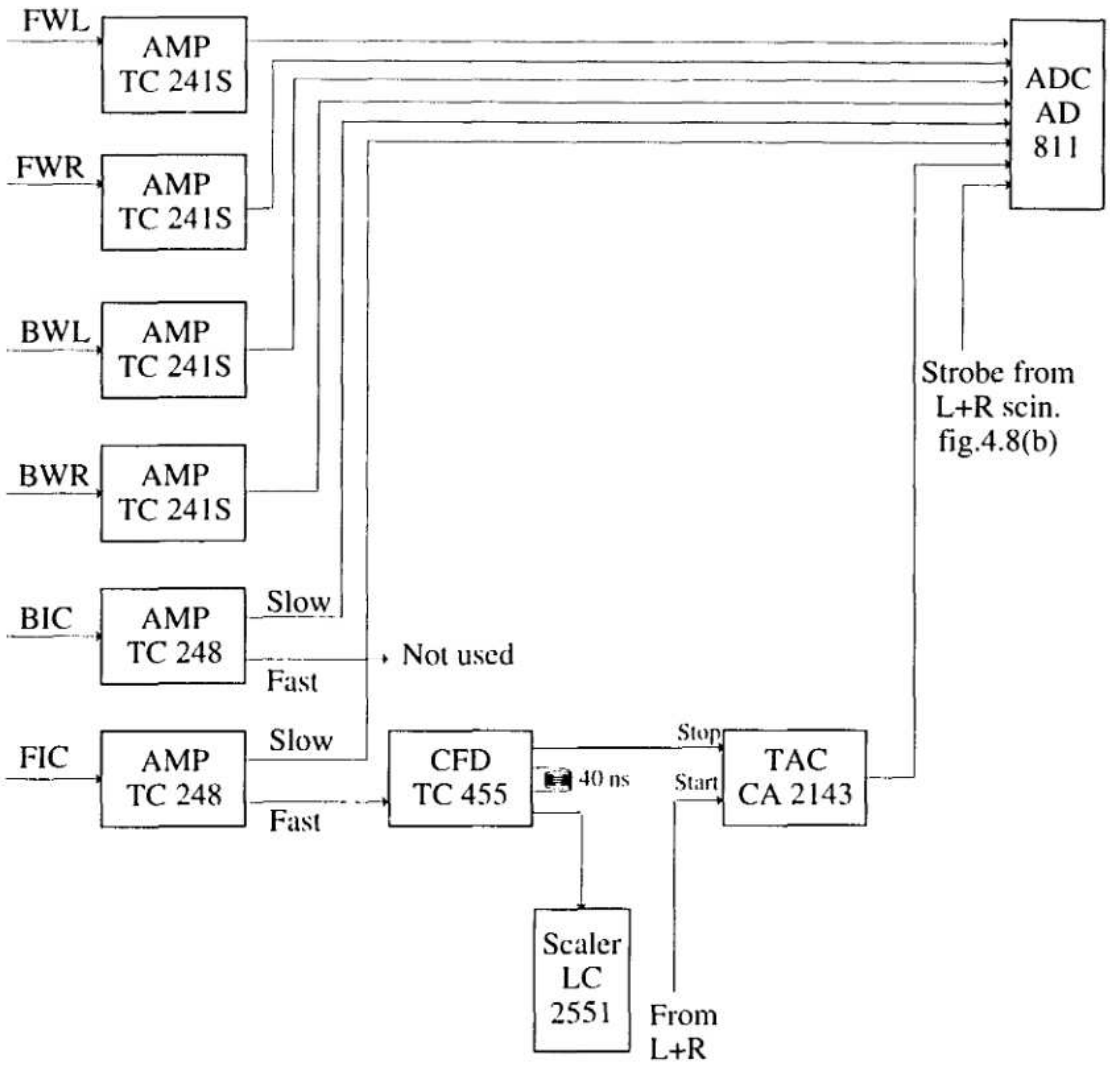

Figure 4.8 (a) Wire chamber electronics for the expt. #92030

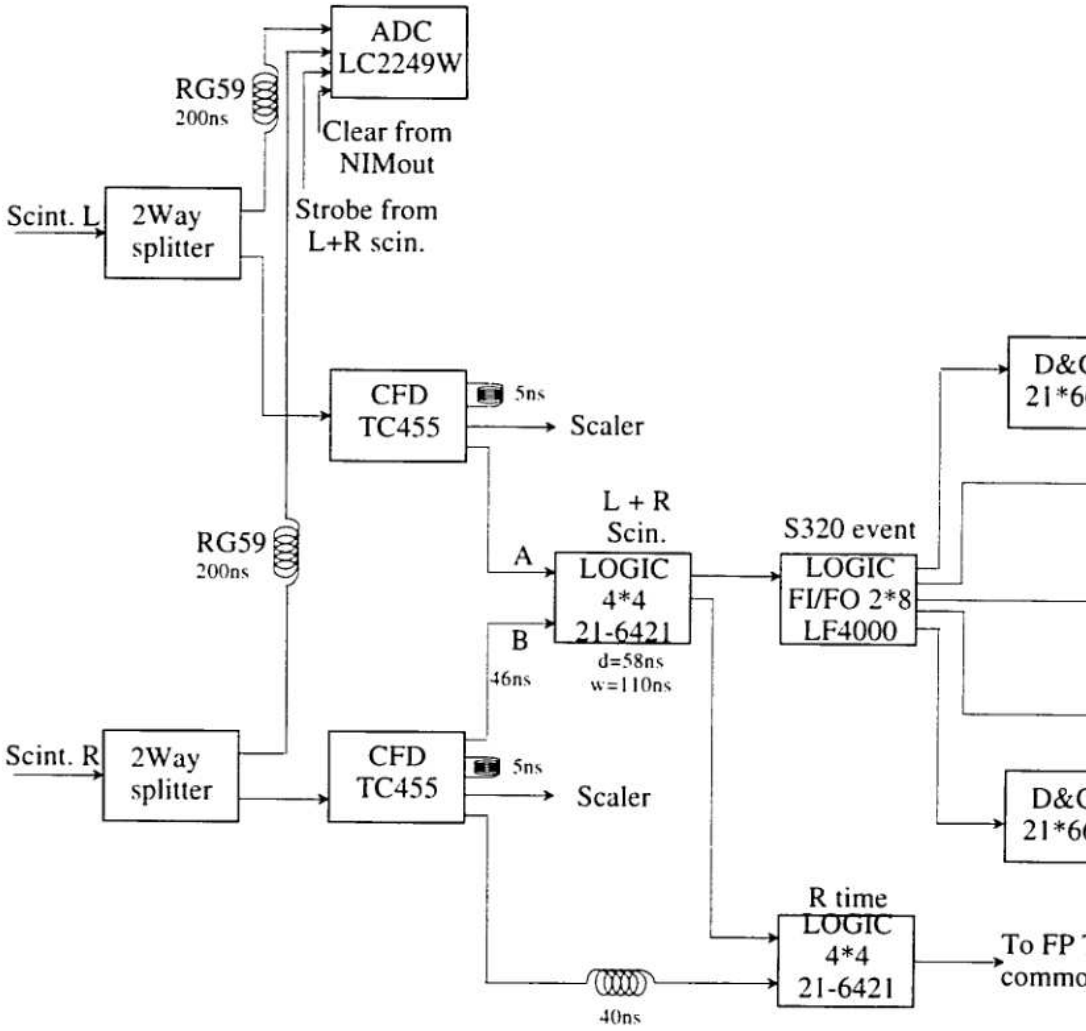

Fig. 4.8 (b) Scintillator electronics for the expt. #92030

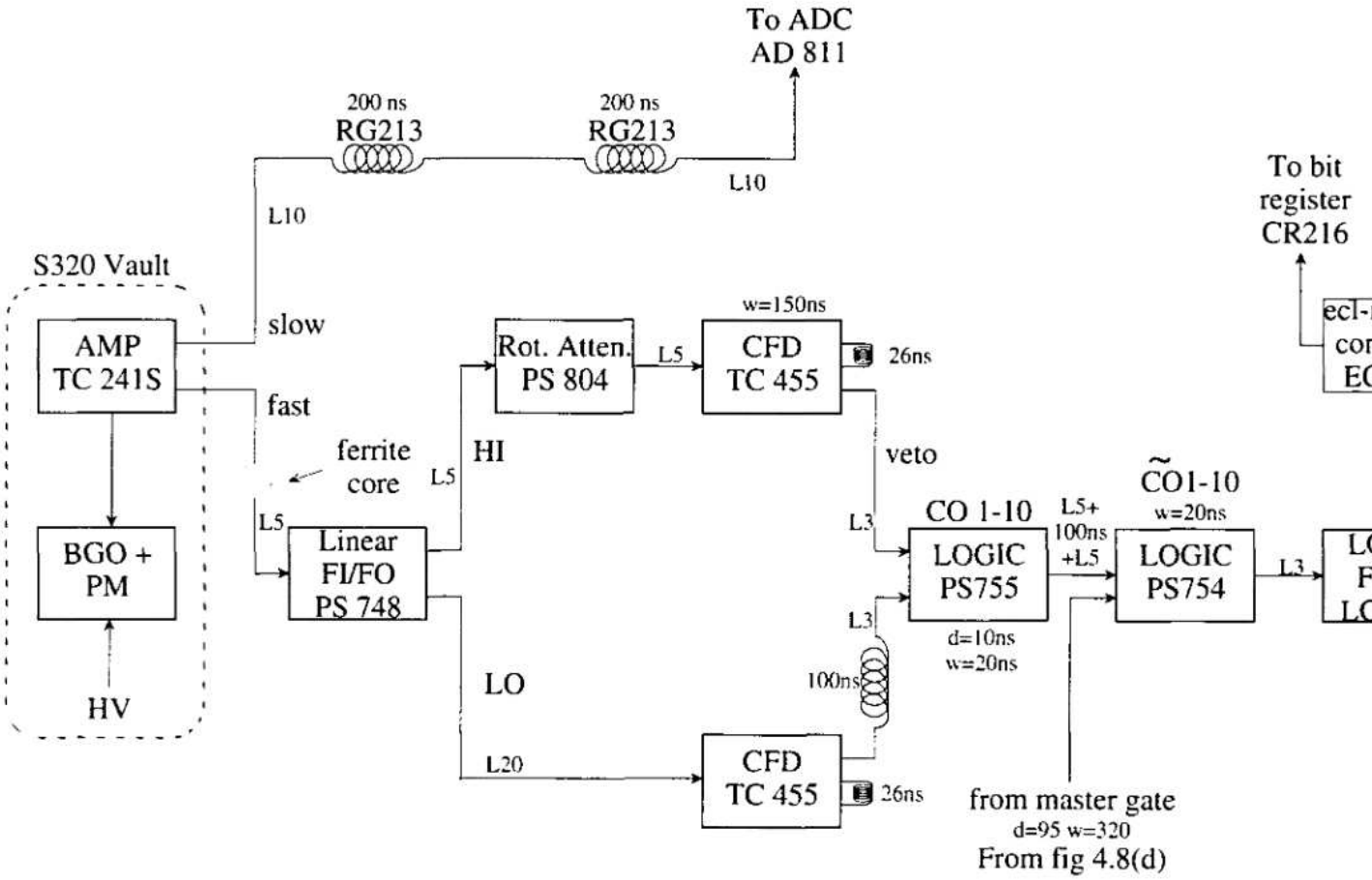

Fig. 4.8 (c) BGO electronics for the expt. #92030

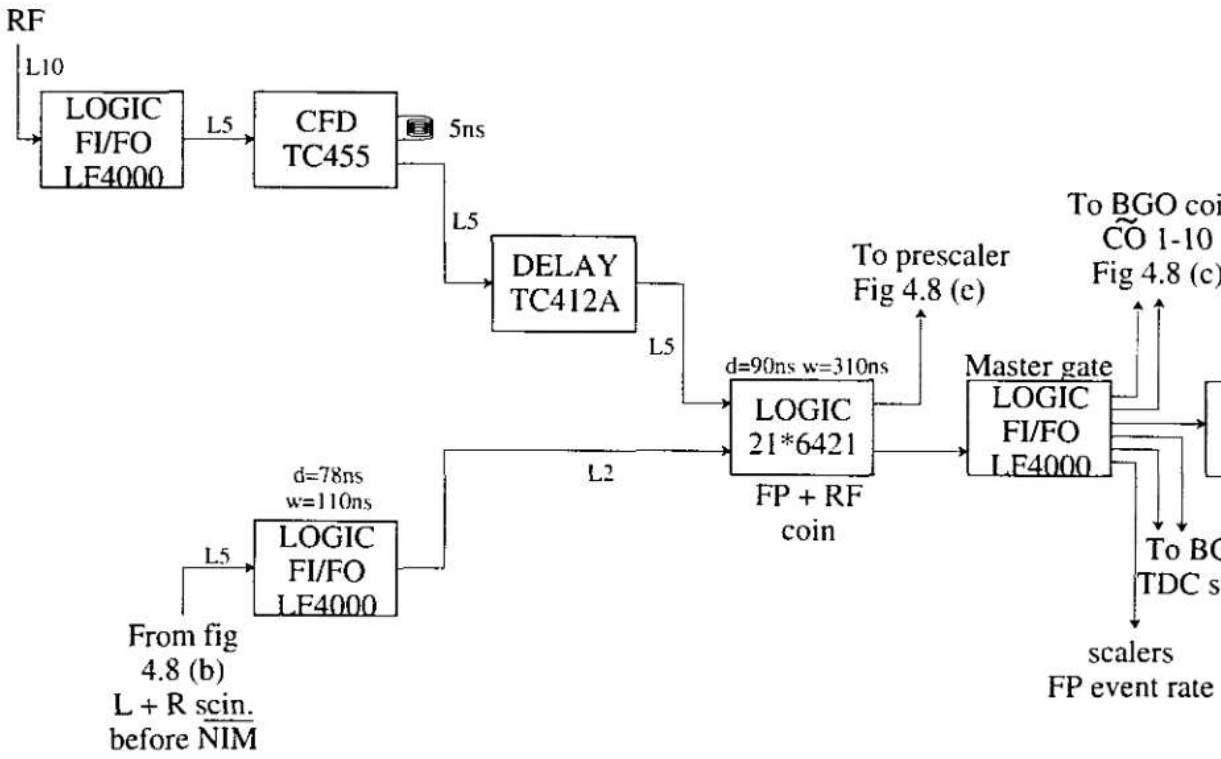

Fig. 4.8 (d) Master gate electronics for the expt. #92030

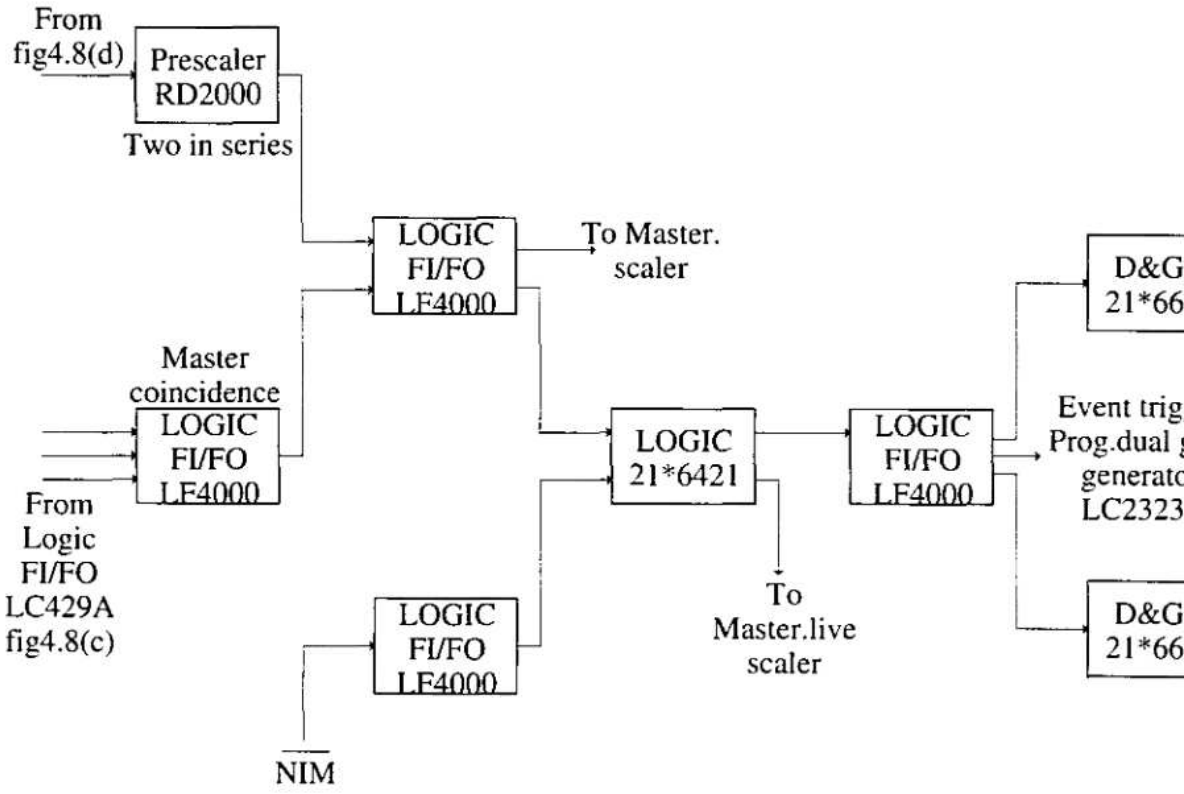

Fig. 4.8 (e) Master coincidence electroincs for the expt. #92030

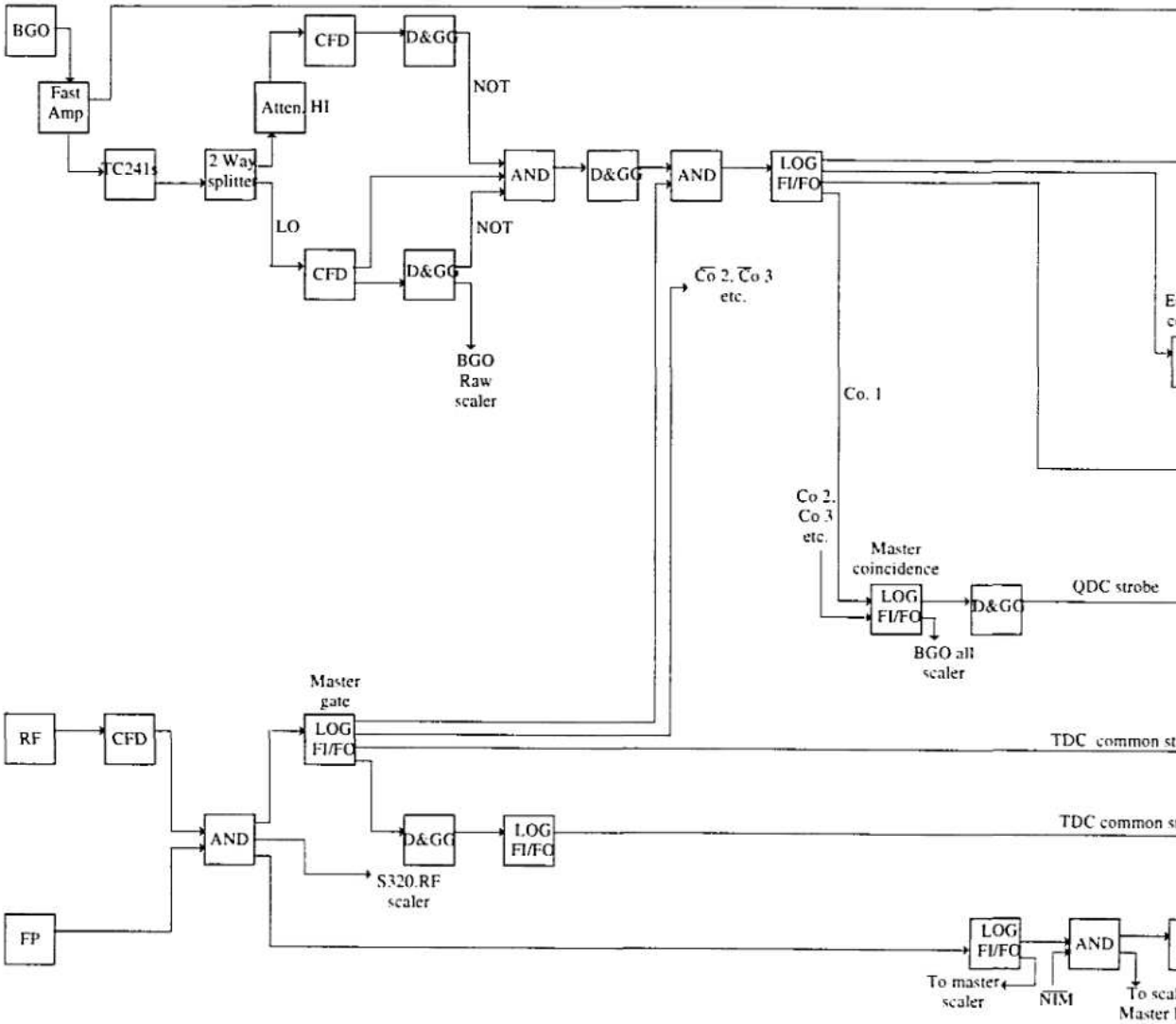

Figure 4.9 Schematic electronics setup for the expt. #93018-1

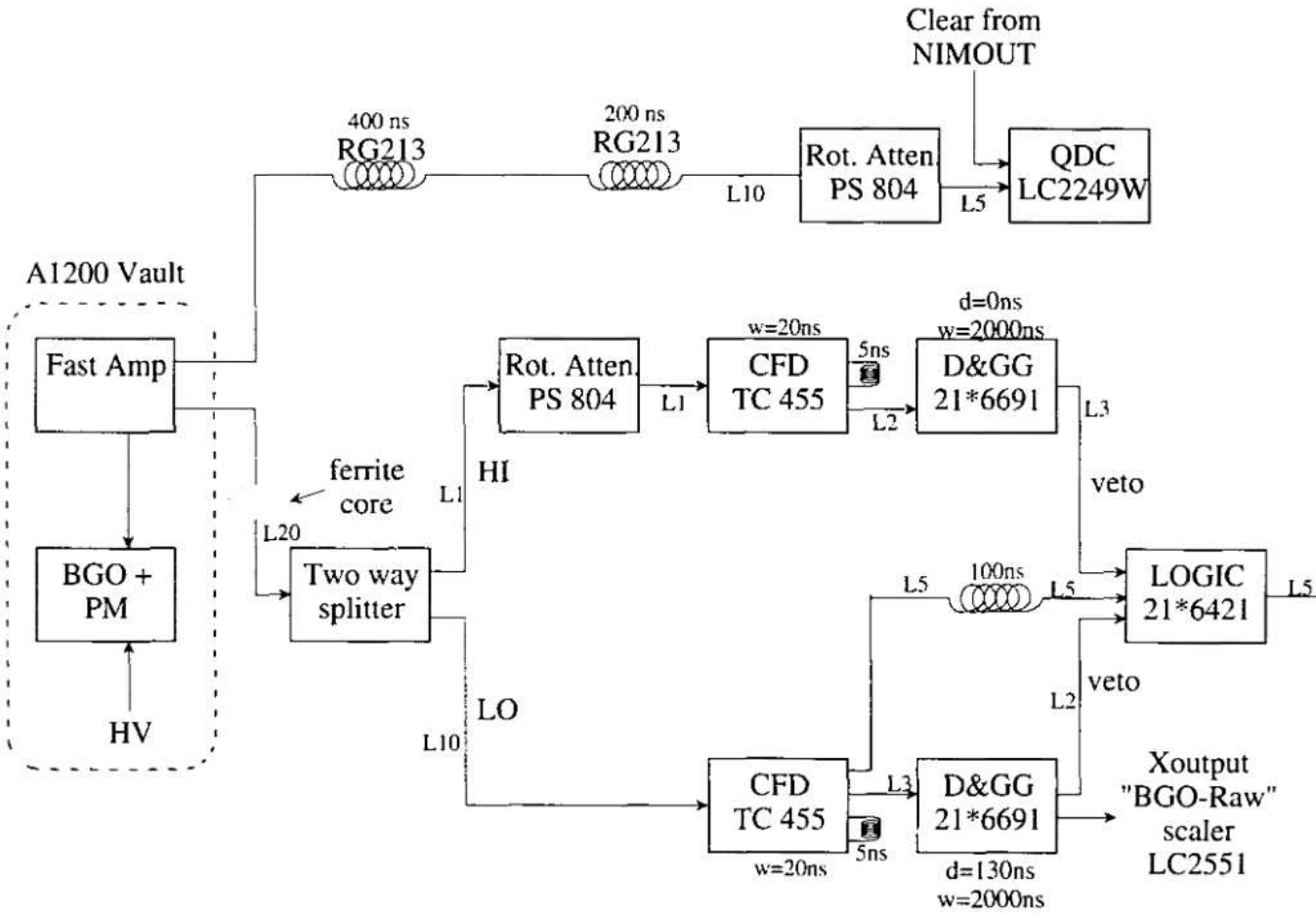

Fig. 4.10 (a) BGO electronics for the expt. #93018-1

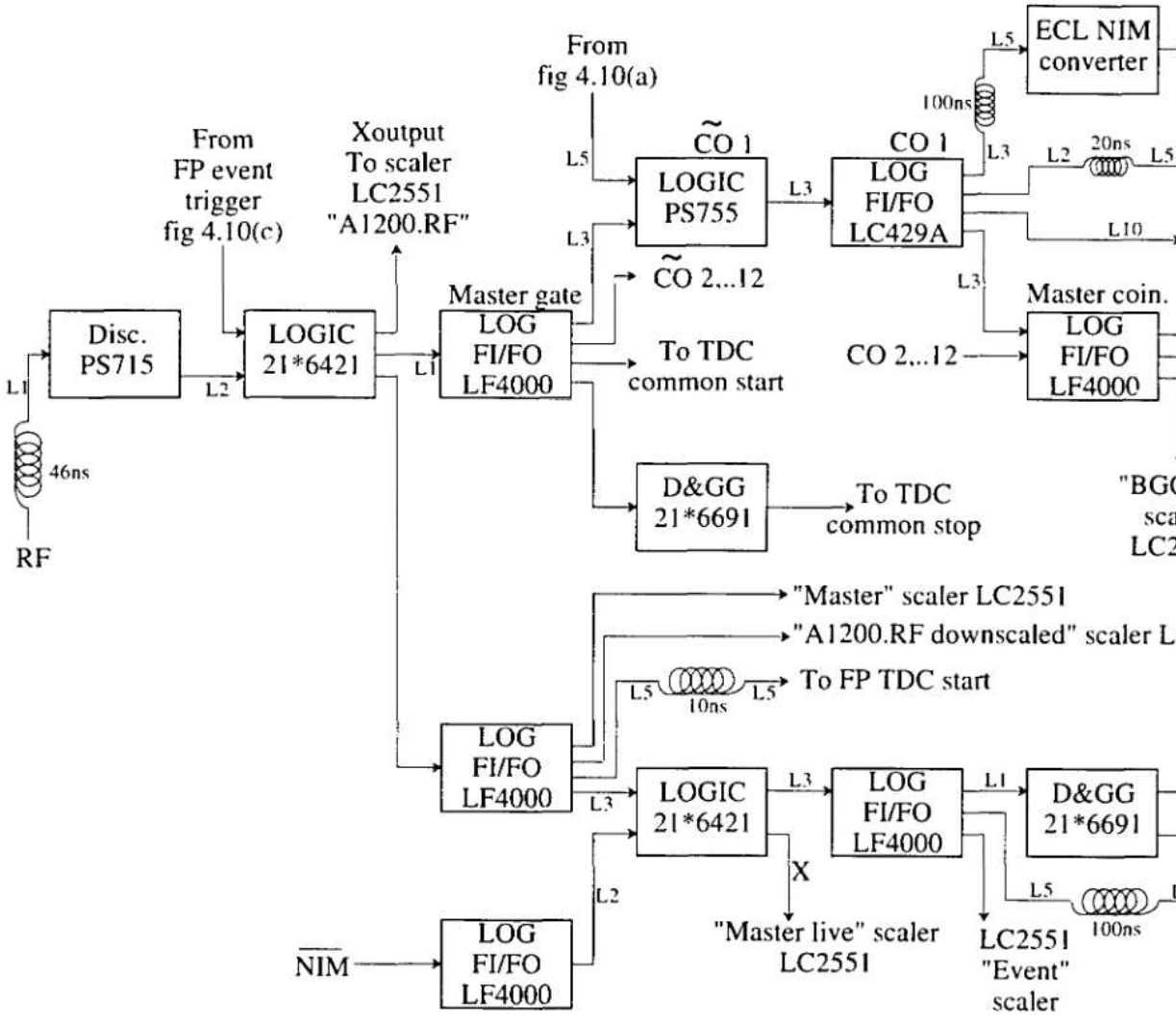

Fig. 4.10 (b) BGO and focal plane coincidence electronics for the expt. #93018-1

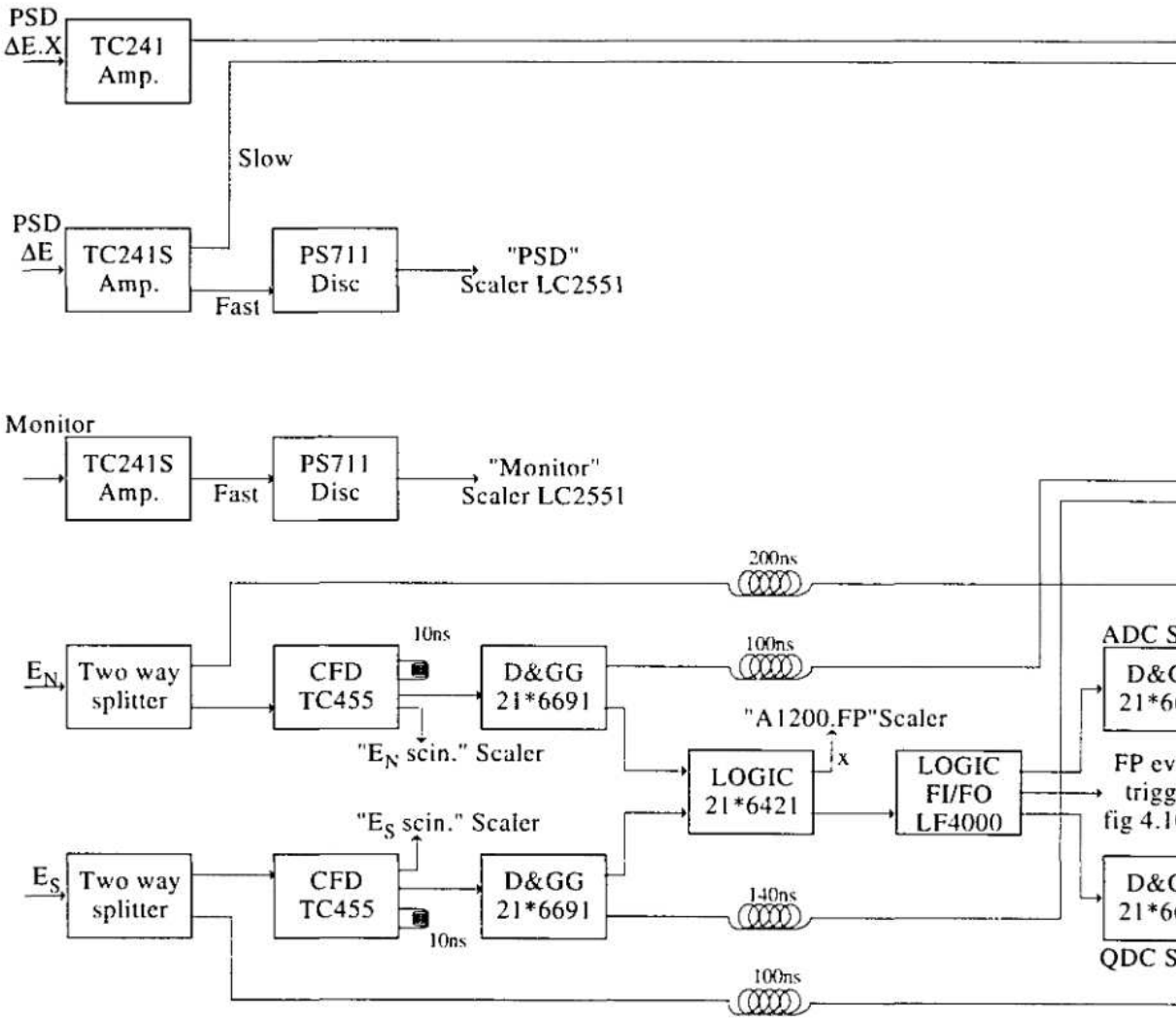

Fig. 4.10 (c) Focal plane electronics for the expt. #93018-1

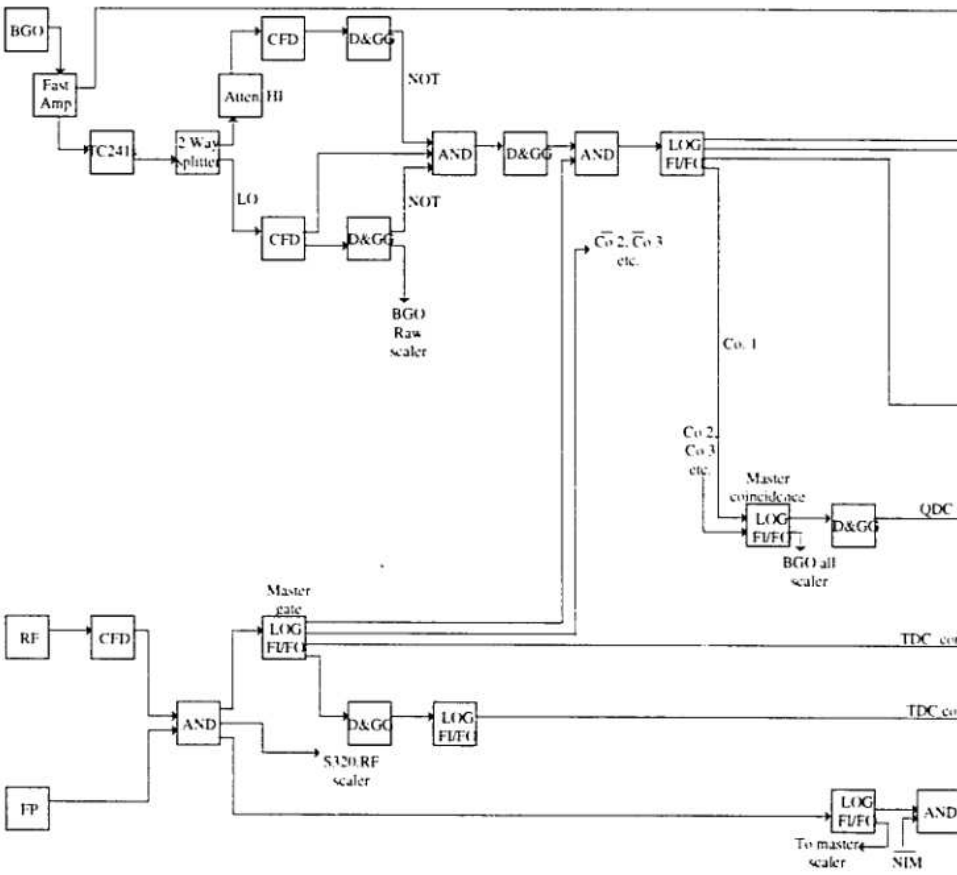

Figure 4.11. Schematic electronics setup for the expt. #9301

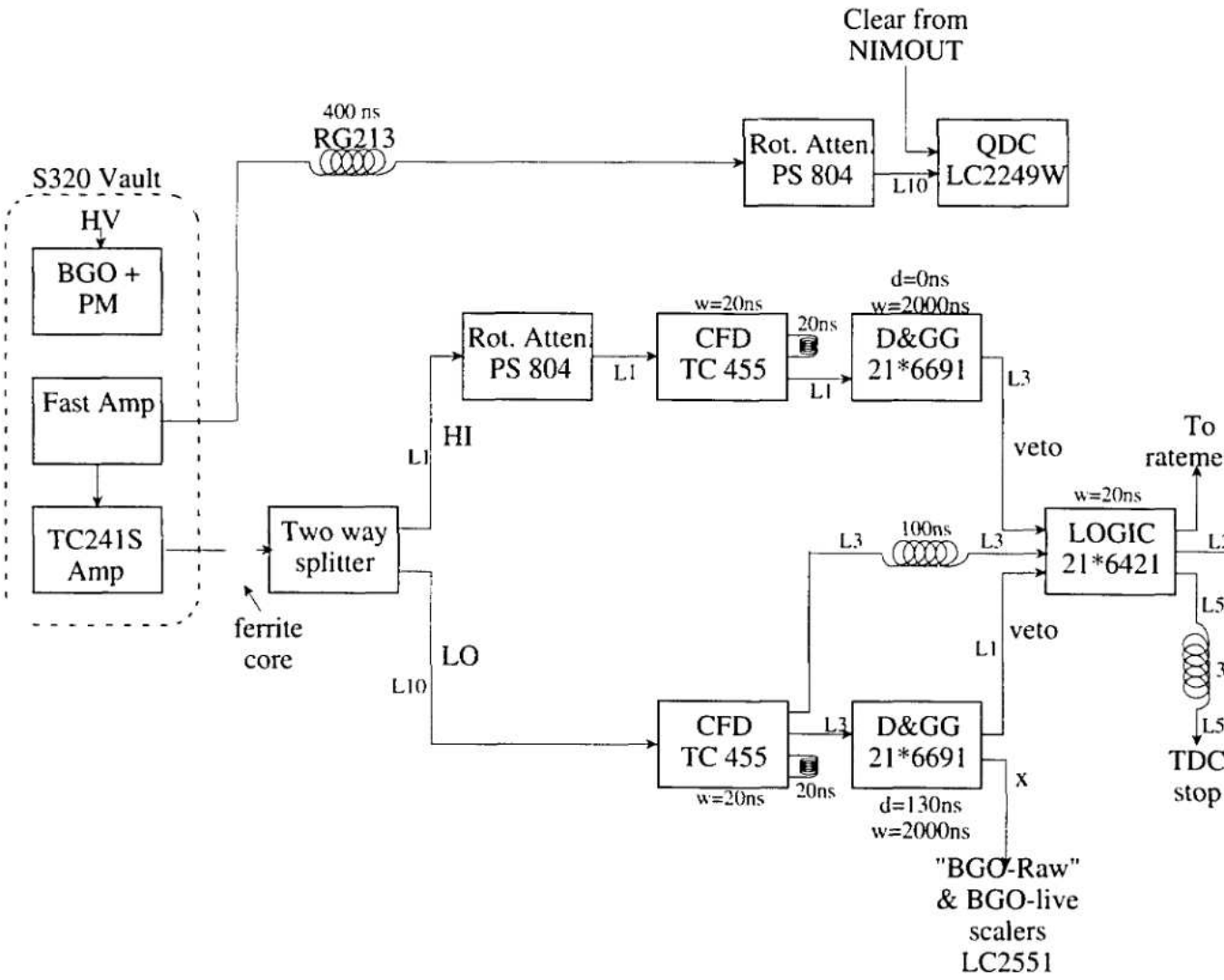

Fig. 4.12 (a) BGO electronics for the expt. #93018-2

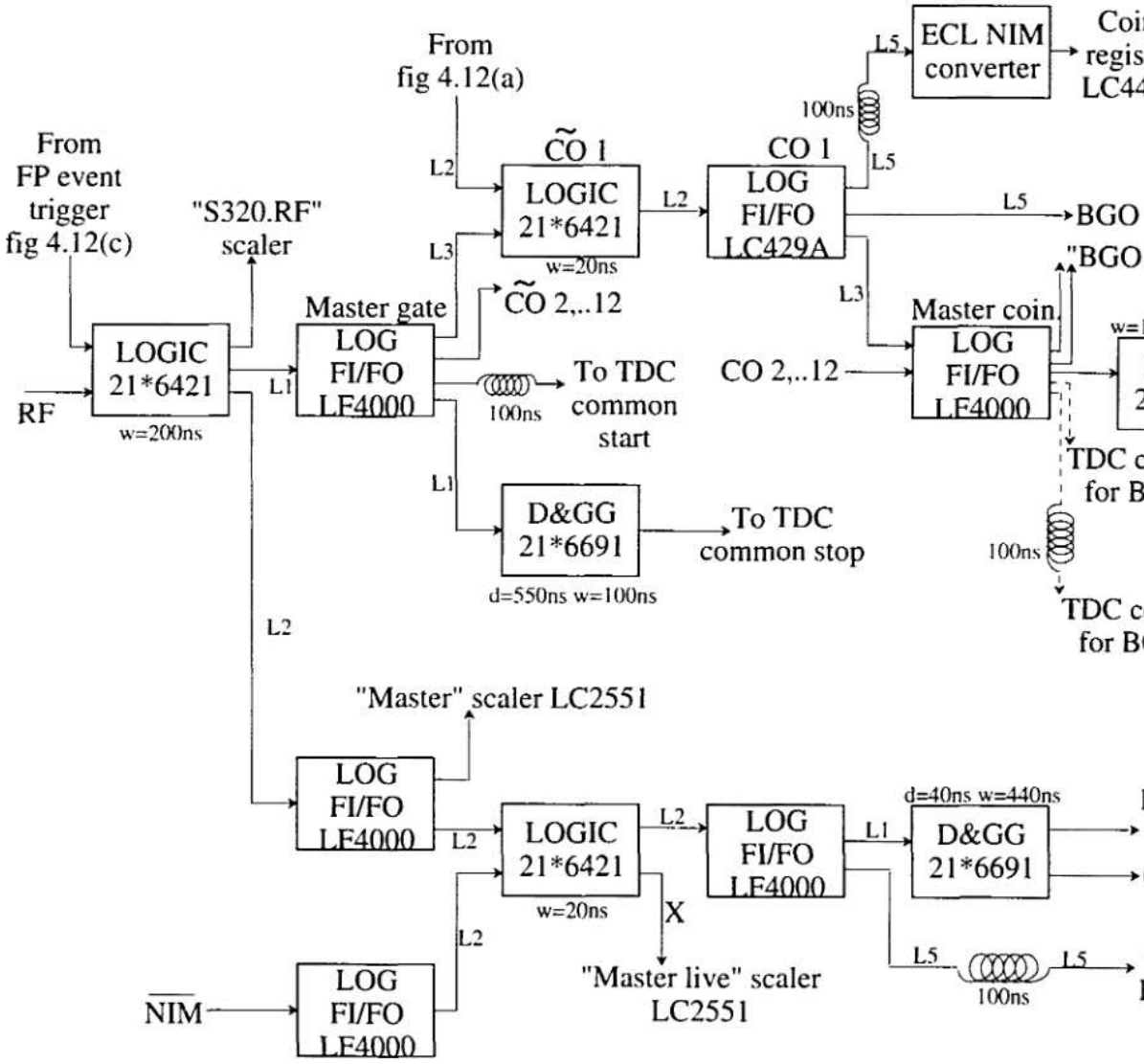

Fig. 4.12(b) BGO and focal plane coincidence electronics for the expt. #93018-2

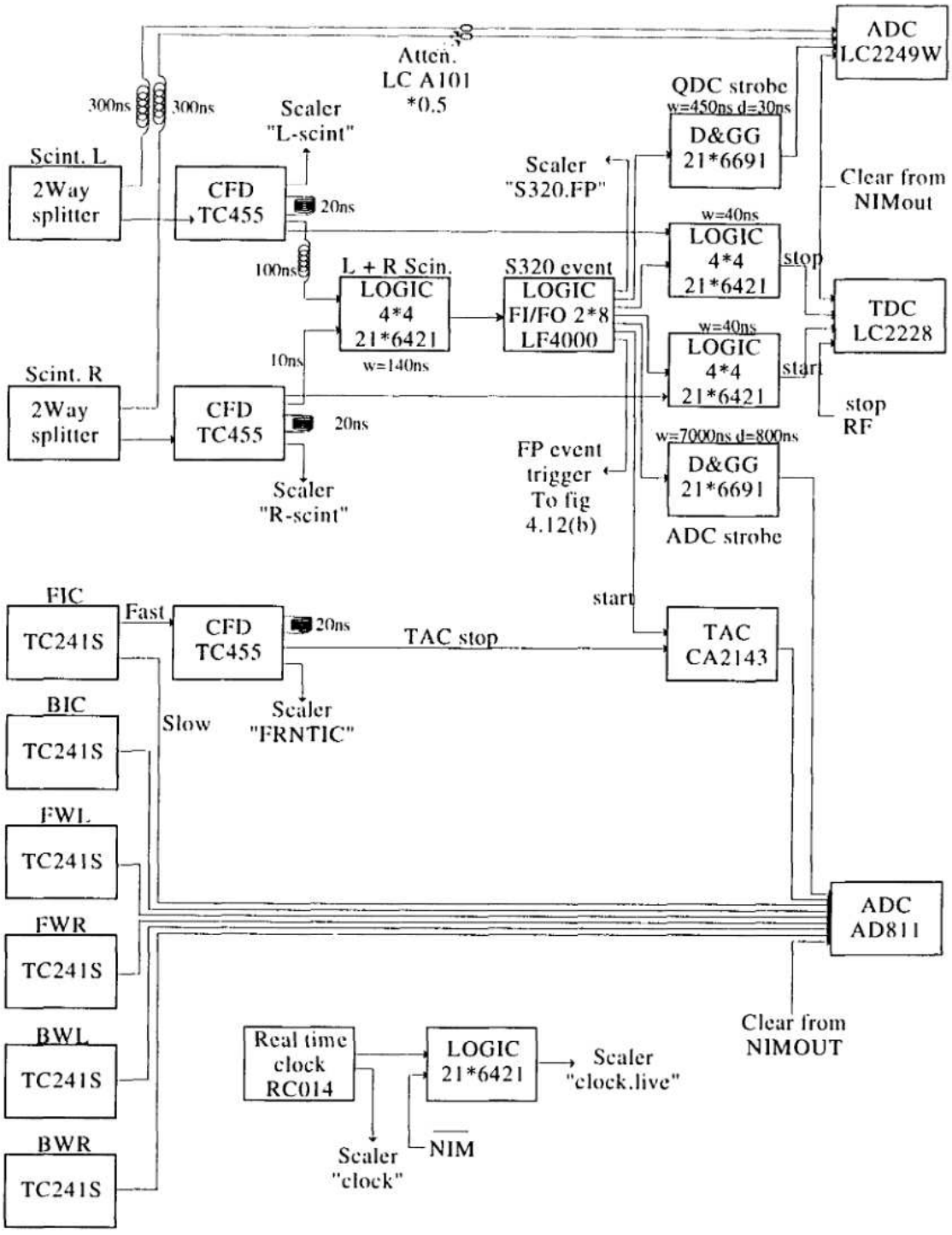

Fig. 4.12(c) Focal plane electronics for the expt. #93018-2

CHAPTER 5

TIMING AND ENERGY PERFORMANCE OF BGO DETECTORS

Bismuth Germanate, $Bi_4Ge_3O_{12}$ (BGO), scintillation detectors were used in the present experiment to detect Doppler-shifted 430 keV γ-rays. The material has a high Z value and a high density of 7.13 gcm^{-3}. Therefore, it has a high detection efficiency for γ-rays and a high photofraction. Due to these reasons, BGO detectors are extensively used in positron emission tomography (PET) scanners.

The BGO detectors used in the present work consist of BGO crystals of 3/4" dia x 2", optically coupled to the Hamamatsu photomultiplier tubes of R1213 or R1166 (high gain variant of the R1213) with E974-13 Hamamatsu bases. The performance of the photomultiplier tubes are described in detail in section 4.2. The BGO detector array was mounted on the lid of the scattering chamber, with the central axis at a distance of 6.4 cm from the target. The geometry is shown in the figure 4.6 (see chapter 4).

The output signals from BGO detectors had a rise time of about 8 ns and a decay time of about 200 ns. The signals show many fluctuations due to single photoelectron emission from the photocathode [Annakkage, 1994]. A typical output pulse from a BGO detector is shown in the figure 5.1. A Monte-Carlo simulation of the pulse shapes [Roberts, 1994] has been performed assuming 150 photoelectrons associated with an output signal [Annakkage, 1994]. A simulated pulse is shown in the figure 5.2. Surprisingly good agreement between the BGO output pulses and the simulated pulses is obtained.

The timing resolution of BGO detectors achieved in the present experiment was 6.5 ns FWHM. A typical time of flight spectrum is shown in the figure 5.3. The time is

measured relative to the beam burst of the cyclotron. The repetition rate of the beam bursts was 14.9 MHz. The spectrum shows a strong prompt pulse and several weak pulses from random coincidences, separated by 67 ns, and also γ-rays from the beam stop.

A typical γ-ray spectrum of a BGO detector for 662 keV γ-rays from a ^{137}Cs source is shown in the figure 5.4. The energy resolution and the total detection efficiency for 662 keV γ-rays are about 17% and 6.6%, respectively. The spectrum displays a high photopeak to compton ratio. An energy spectrum for Doppler-shifted 430 keV γ-rays for the ^{6}Li target obtained during the experiment is shown in the figure 5.5. The energy resolution and the total detection efficiency for Doppler-shifted 430 keV γ-rays are about 29% and 11%, respectively. Energy spectra of Doppler-shifted 430 keV γ-rays for the ^{12}C target also show strong photopeaks, but those for the ^{90}Zr target display very weak photopeaks. For the heavier targets, the BGO detectors are detecting not only 430 keV γ-rays, but also the γ-rays from deexcitations of the residual nuclei. The 430 keV Doppler-shifted γ-rays energy spectra for the ^{120}Sn and ^{208}Pb targets indeed do not show photopeaks. Figure 5.6 shows an energy spectrum of γ-rays for the ^{208}Pb target. This result shows that the technique for isolating spin-flip components in the (^{7}Li,^{7}Be) reaction by means of detecting the 430 keV γ-rays is limited to light target nuclei.

Figure 5.7 shows the dependence of the energy of the detected γ-rays on the laboratory angle. The solid curve describes the Doppler equation for electromagnetic radiation, given by

$$E = E_0 \frac{\sqrt{1-\left(v/c\right)^2}}{1-v/c\cos\theta}. \qquad (5.1)$$

Here, E_0 is the energy emitted by the radiation source, E is the Doppler-shifted energy, and v is the relative velocity of the moving source. The fit of the experimental data with the Doppler equation confirms that the BGO detectors are detecting 430 keV γ-rays.

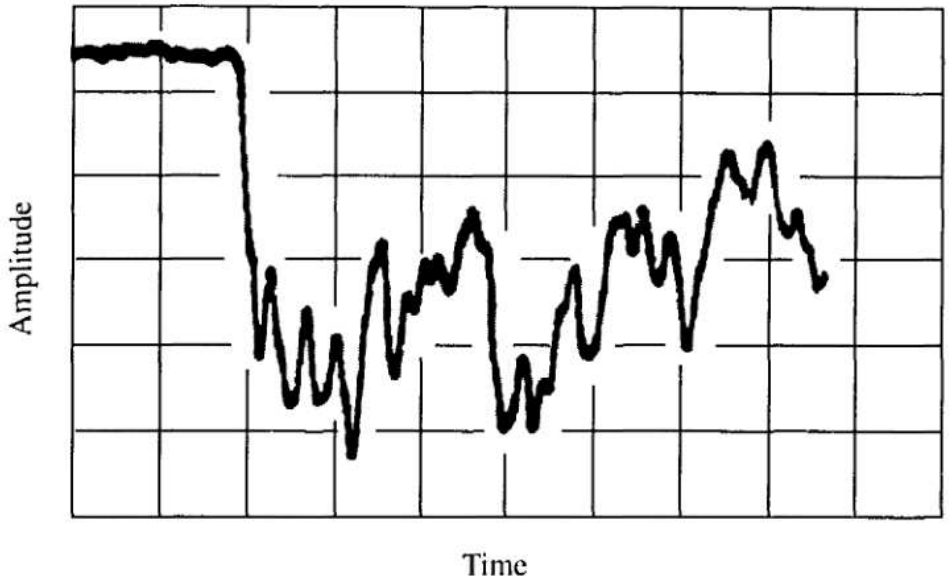

Figure 5.1 A typical output pulse from a BGO detector. Time scale is 10 ns per division. Pulse height scale is 5 mV per division [Annakkage, 1994].

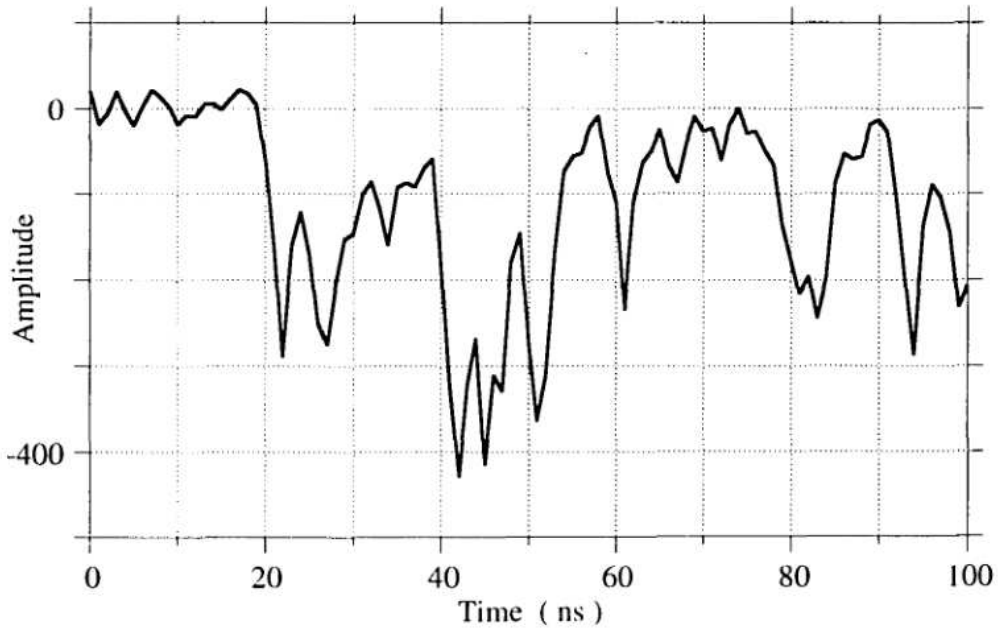

Figure 5.2 A simulated pulse from a BGO detector assuming 150 photoelectrons per pulse [Roberts, 1994; Annakkage, 1994].

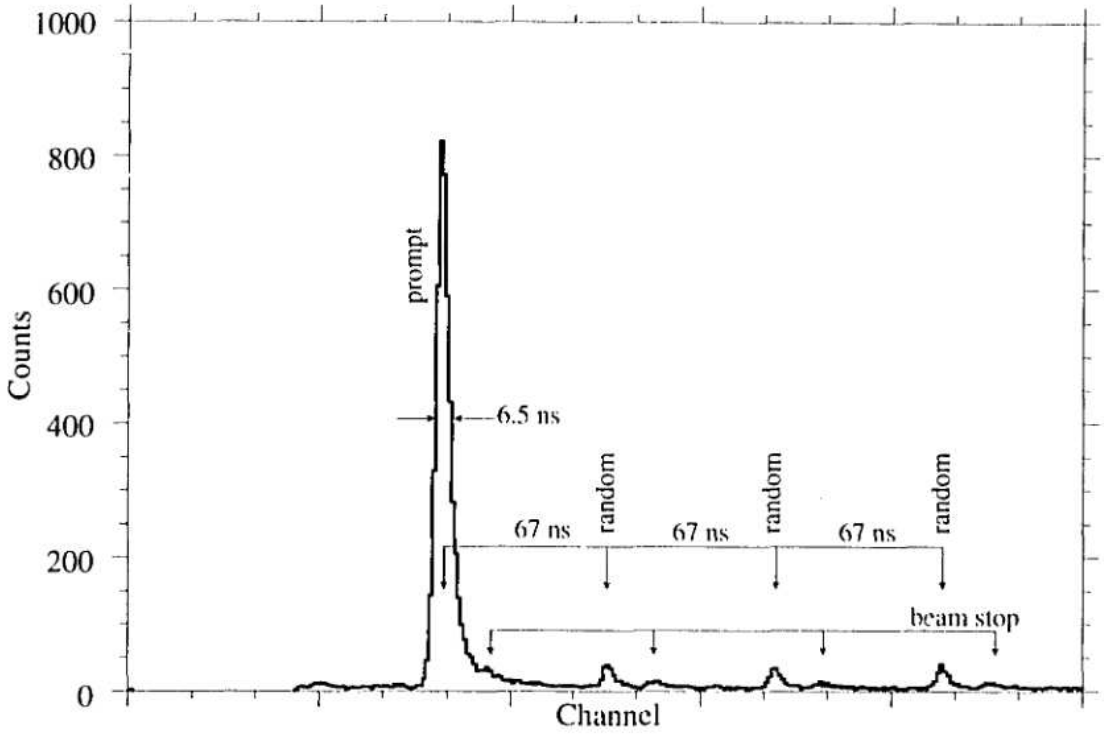

Figure 5.3 A typical time spectrum of 430 keV γ-rays [Annakkage, 1994].

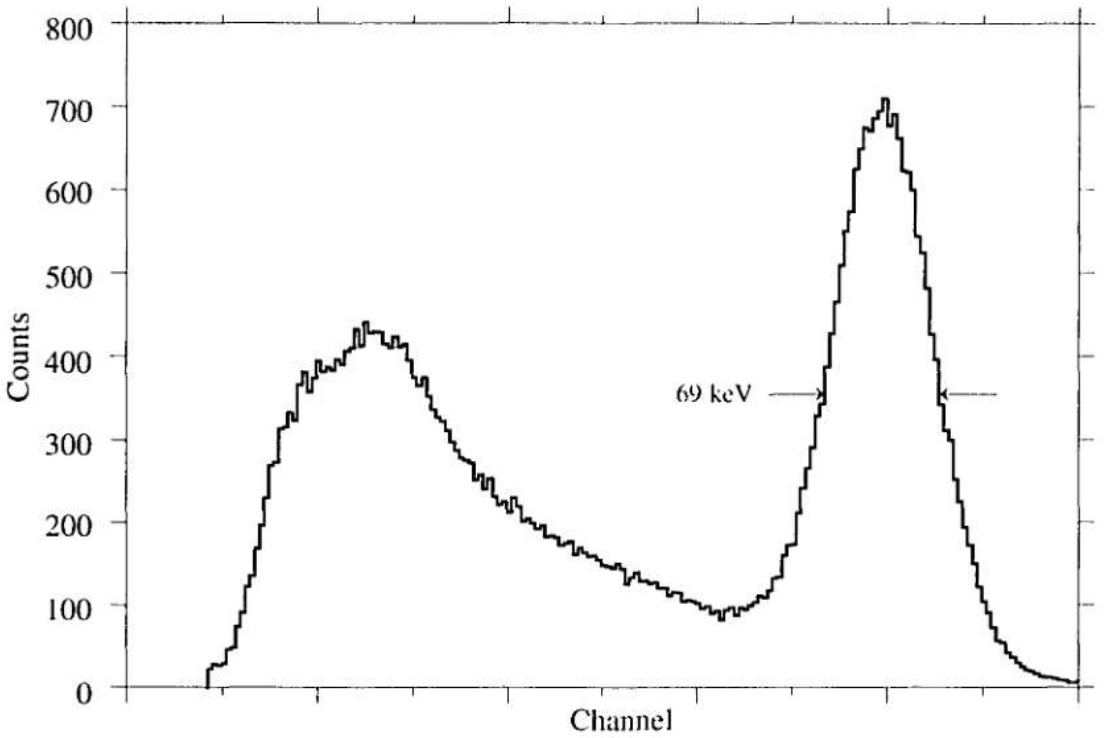

Figure 5.4 A typical energy spectrum of 662 keV γ-rays from a ^{137}Cs source. Events below 50 keV are suppressed.

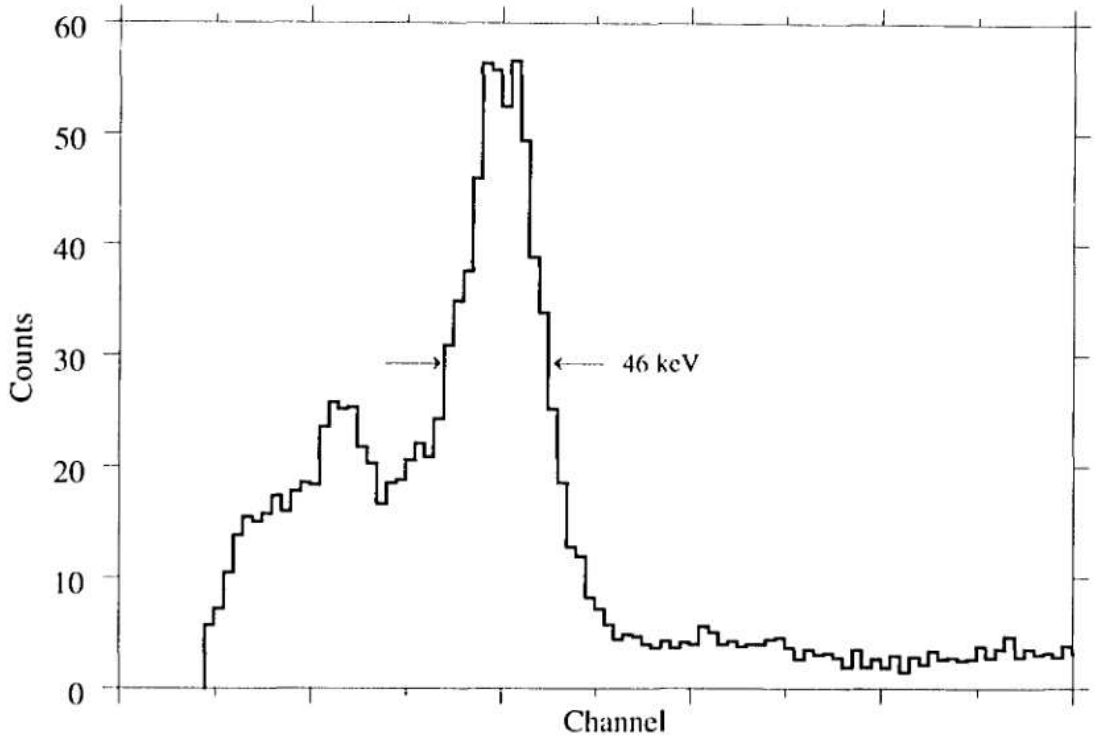

Figure 5.5 A typical energy spectrum of 430 keV Doppler-shifted γ-rays for the ^{6}Li target. Events below 50 keV are suppressed.

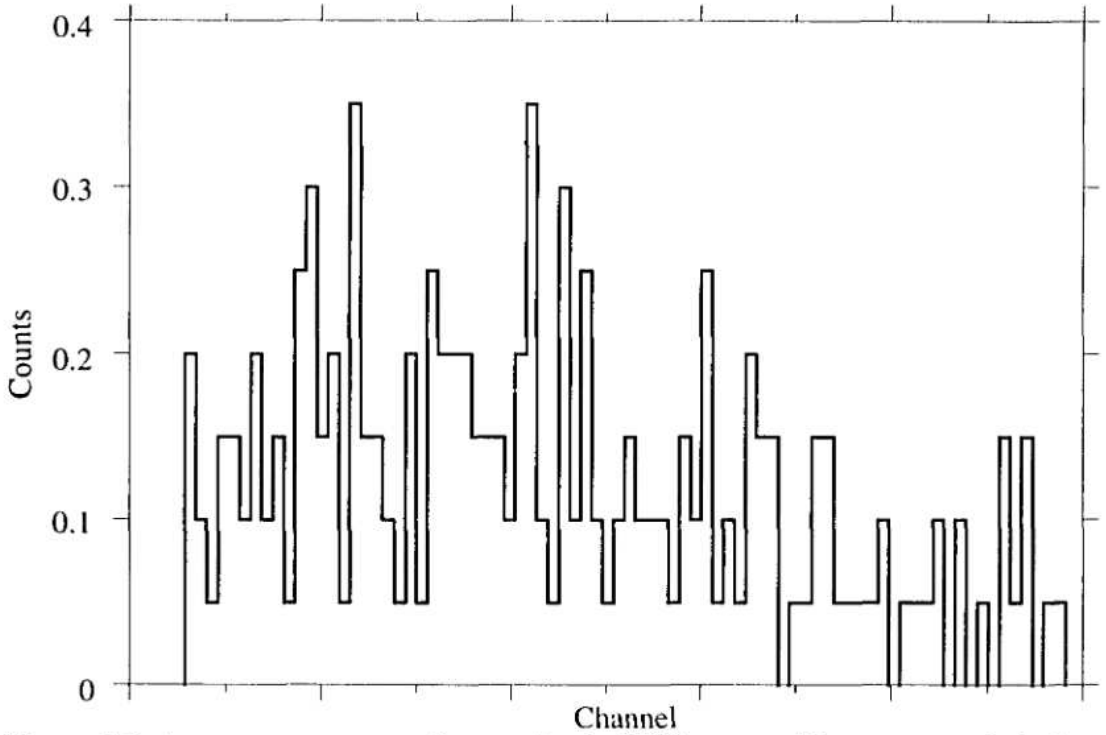

Figure 5.6 An energy spectrum of γ-rays for the ^{208}Pb target. The energy scale is the same as for figures 5.4 and 5.5.

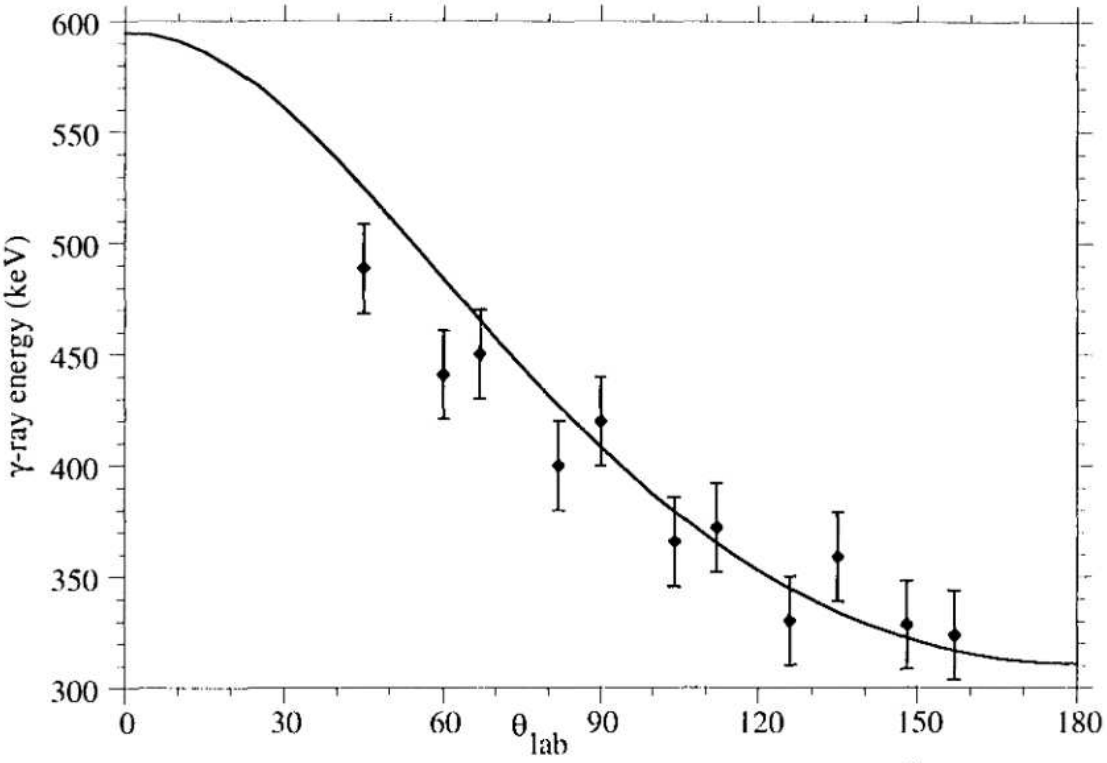

Figure 5.7 Energy of Doppler-shifted 430 keV γ-rays obtained for the ^{6}Li target as a function of lab angle.

CHAPTER 6

EXPERIMENTAL RESULTS

6.1 Experimental results

The (^{7}Li,^{7}Be) and (^{7}Li,^{7}Be γ) reactions were investigated in three experiments: #92030, #93018-1 and #93018-2. In the experiments #92030 and #93018-2, the data were taken at lab angles of 2.0 - 8.5 degree. In the experiment #93018-1, the data were taken at zero degree. The finite-angle measurements were performed with two different aperture settings: (1) ^{7}Be in singles and ^{7}Be in coincidence with 430 keV γ-rays were measured with an aperture of 2" x 2" which corresponds to a solid angle of 0.67 msr; the coincidence and the singles events were measured at lab angles of 2 - 6 degree in 1 or 2 degree steps; (2) ^{7}Be singles events without coincidence were measured at lab angles of 2.0 - 8.5 degree in 0.5 degree steps with an aperture of 1.125" x 0.75" which corresponds to a solid angle of 0.20 msr. All ^{7}Be spectra showed a peak due to hydrogen contamination on the targets. The contribution from hydrogen contamination are removed in the following figures using independently measured data for hydrogen with a polystyrene, C_8H_8, target. The thicknesses of hydrogen contaminants (from water) were typically about 8.3 $\mu g/cm^2$, 31.3 $\mu g/cm^2$, 0.2 $\mu g/cm^2$, 0.1 $\mu g/cm^2$, and 0.4 $\mu g/cm^2$ for ^{6}Li, ^{12}C, ^{90}Zr, ^{120}Sn, and ^{208}Pb targets, respectively. The underlying non-resonant background was assumed to be from the quasi-free charge-exchange reaction as described in the chapter 4.

6.1.1 The ^{6}Li(^{7}Li,^{7}Be)^{6}He reaction

The ^{7}Be singles spectra for the ^{6}Li target are shown in the figures 6.1(a) and 6.1(b). Spectra for ^{7}Be singles and ^{7}Be in coincidence with 430 keV γ-rays are shown in the figures 6.2(a) and 6.2(b). Five peaks are seen at excitation energies of 0.0 MeV, 1.93±0.03 MeV, 5.6±0.3 MeV, 14.2±0.3 MeV, and 22.7±0.3 MeV. They have energy widths of 1.55±0.07 MeV, 1.55±0.07 MeV, 12±1 MeV, 7.0±0.4 MeV, and 14±1 MeV, respectively. The widths of the gaussians for the first two peaks were kept the same when fitting the peaks since they are discrete states, and the widths are due to the finite resolution of the magnetic spectrograph. Cross sections for ^{7}Be singles and coincidence at lab angle of 2 degree, average excitation energies, and energy widths of states in ^{6}He are listed in table 6.1. The values $\frac{d\sigma^{coin.}}{d\Omega_{cm}}$ (corrected) are the coincidence cross sections corrected for the γ-ray detection efficiency, which was 11%.

The angular distributions of the cross sections for the singles events observed for the states in ^{6}He are shown in the figure 6.3. The points labeled with H may have increased uncertainties because of interference from hydrogen contamination. These are the angles where the contributions from hydrogen contamination had to be subtracted. The statistical uncertainties of the cross sections are very small. Uncertainties of about 10% were assumed for all data points estimated for singles cross sections from the uncertainties of the fitting procedure. For narrow states, the uncertainties of the coincidence cross sections are typically about the same as those for singles cross sections. The data points for lab angles of 2, 2.5 and 3 degrees of the weak 1.9 MeV state are not reliable due to the uncertainty of the subtraction of underlying hydrogen peak. A small adjustment is made to the 2 and 2.5 degree cross sections according to an assumed smooth dependence on the angle for the ratio of $\sigma(g.s)/\sigma(1.9MeV)$. The cross sections obtained for the $\theta_{lab} \approx 0^{\circ}$ have large absolute uncertainties due to difficulties to measure the integrated charge with the

A1200 magnetic device. However, the relative uncertainties are believed to be small. Therefore, the zero degree cross sections were renormalized by a factor of 1.844. This factor results from the comparison of the measured 0^o cross section for $^{12}C(^7Li,^7Be)^{12}B$ leading to the ^{12}B ground state with the calculated angular distribution which was found to be well described by the DWBA calculations (see section 8.2).

E_x (MeV)	Γ (MeV) (FWHM)	$\frac{d\sigma^{sing.}}{d\Omega_{cm}}$ (mb/sr)	$\frac{d\sigma^{coin.}}{d\Omega_{cm}}$ (mb/sr)	$\frac{d\sigma^{coin.}}{d\Omega_{cm}}$ Corrected. (mb/sr)	$\frac{d\sigma/d\Omega_{corr.}^{coin.}}{d\sigma/d\Omega^{sing.}}$
gs		0.877	0.044	0.400	0.46
1.93±0.03 (5.43)		0.185	0.009	0.081	0.44
5.6±0.3 (9.1)	12±1	3.478	0.144	1.309	0.38
14.2±0.3 (17.7)	6.5±0.4	1.789	0.074	0.673	0.38
22.7±0.3 (26.2)	14±1	1.810	0.096	0.873	0.48

Table 6.1 States in ^6He (present work). The values given in parentheses are the excitation energies relative to the target nucleus (see text).

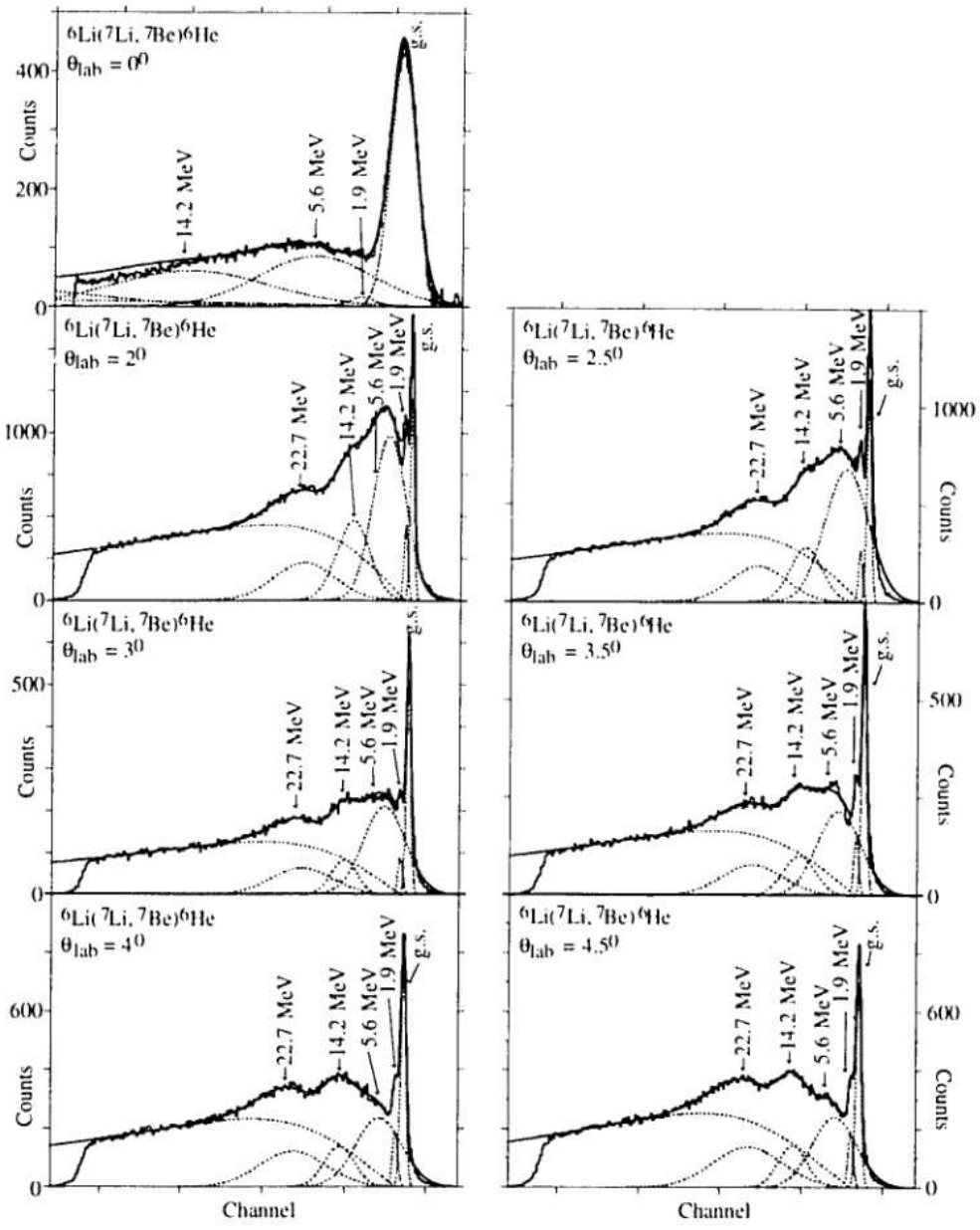

Figure 6.1(a) ^{7}Be singles spectra for ^{6}Li target at lab angles of 0.0 to 4.5 degree.

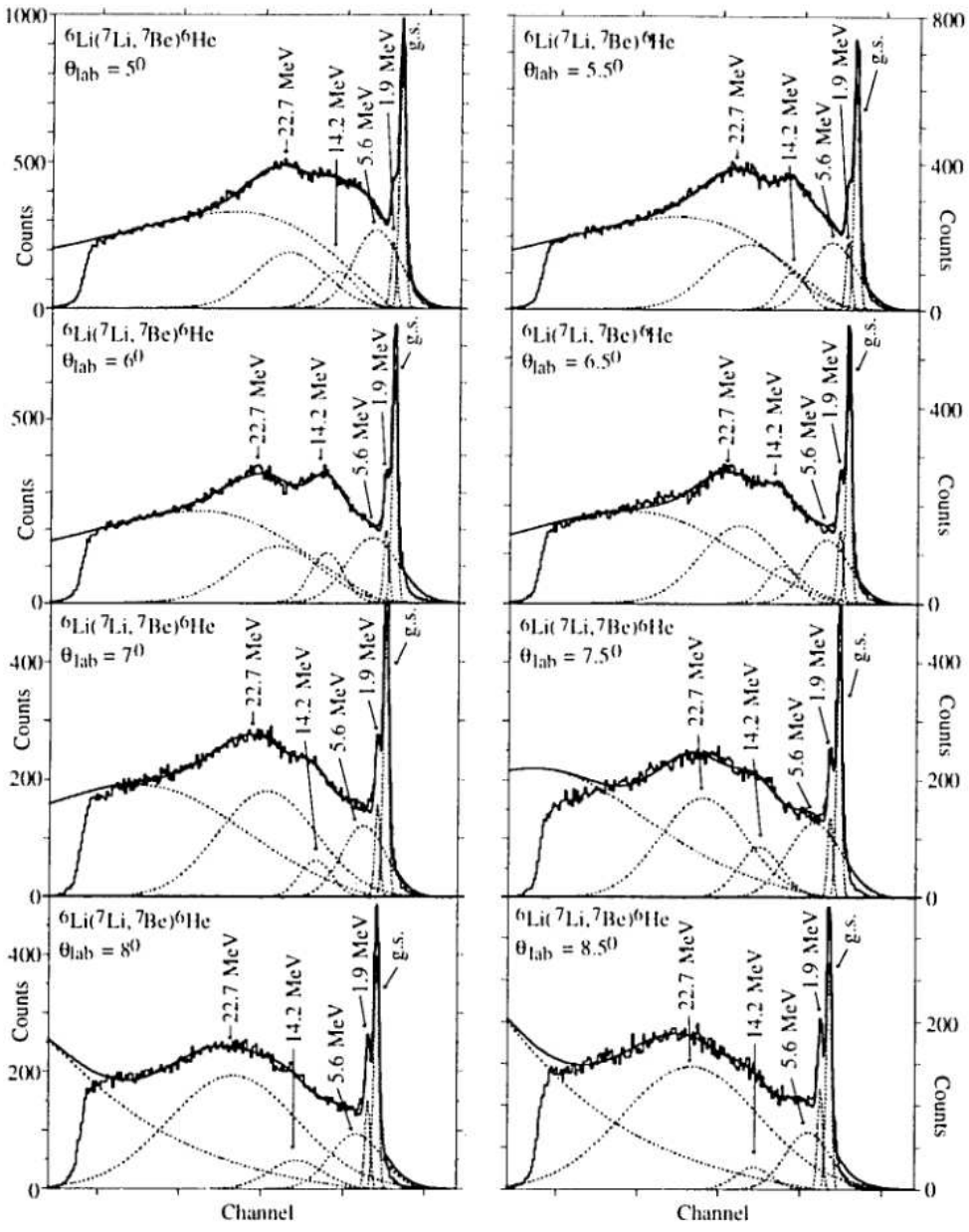

Figure 6.1(b) ^{7}Be singles spectra for ^{6}Li target at lab angles of 5.0 to 8.5 degree.

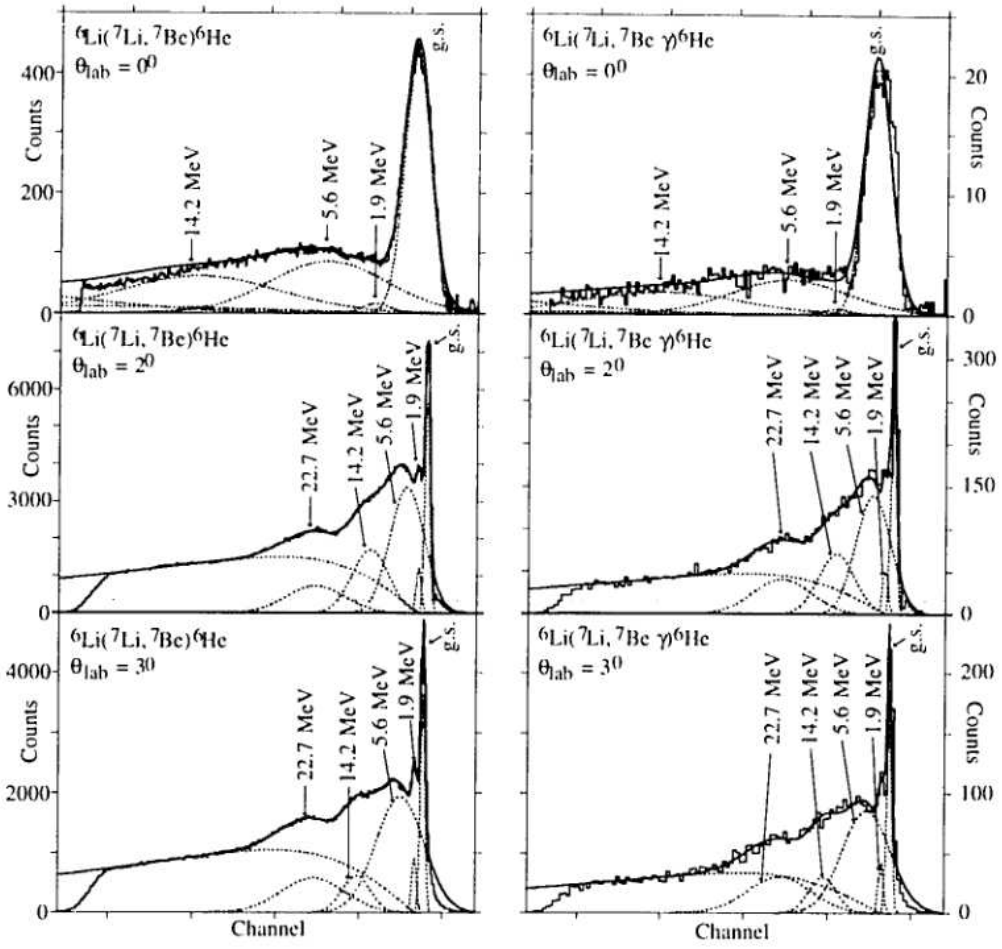

Figure 6.2(a) ^{7}Be singles and coincidence spectra for ^{6}Li target at lab angles of 0.0 to 3.0 degree.

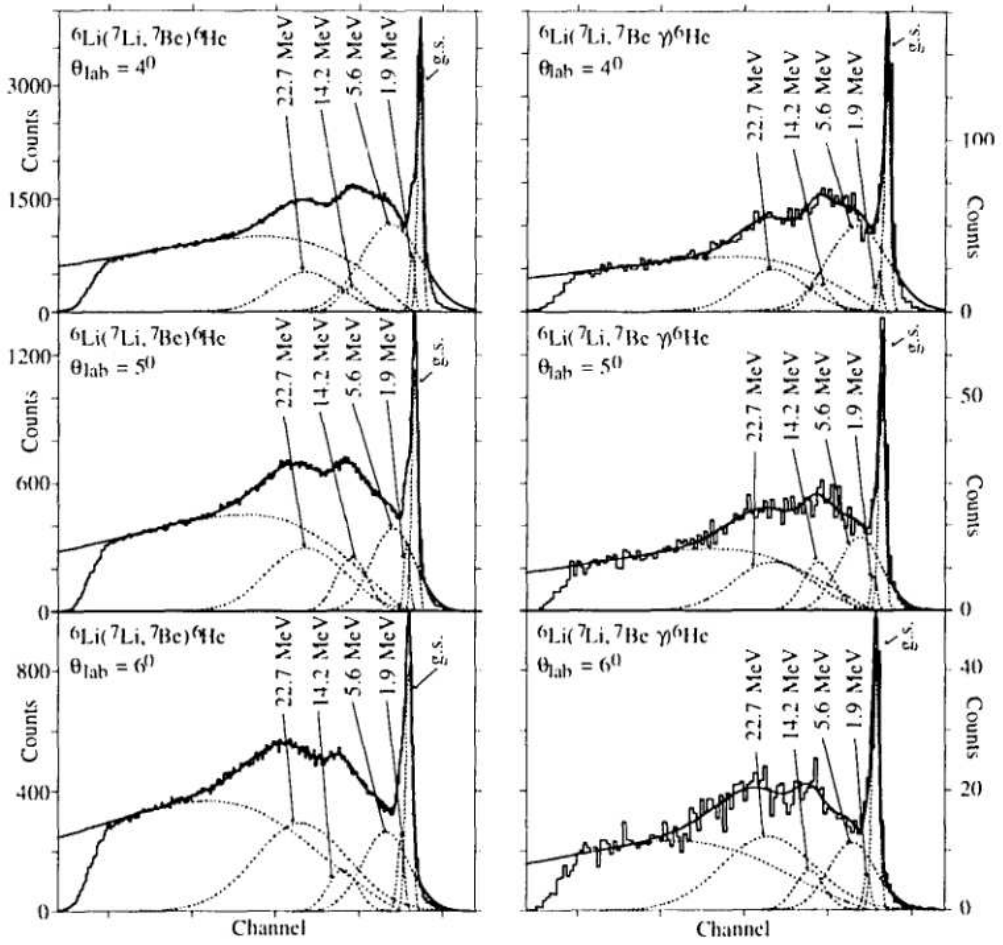

Figure 6.2(b) ^{7}Be singles and coincidence spectra for ^{6}Li target at lab angles of 4.0 to 6.0 degree.

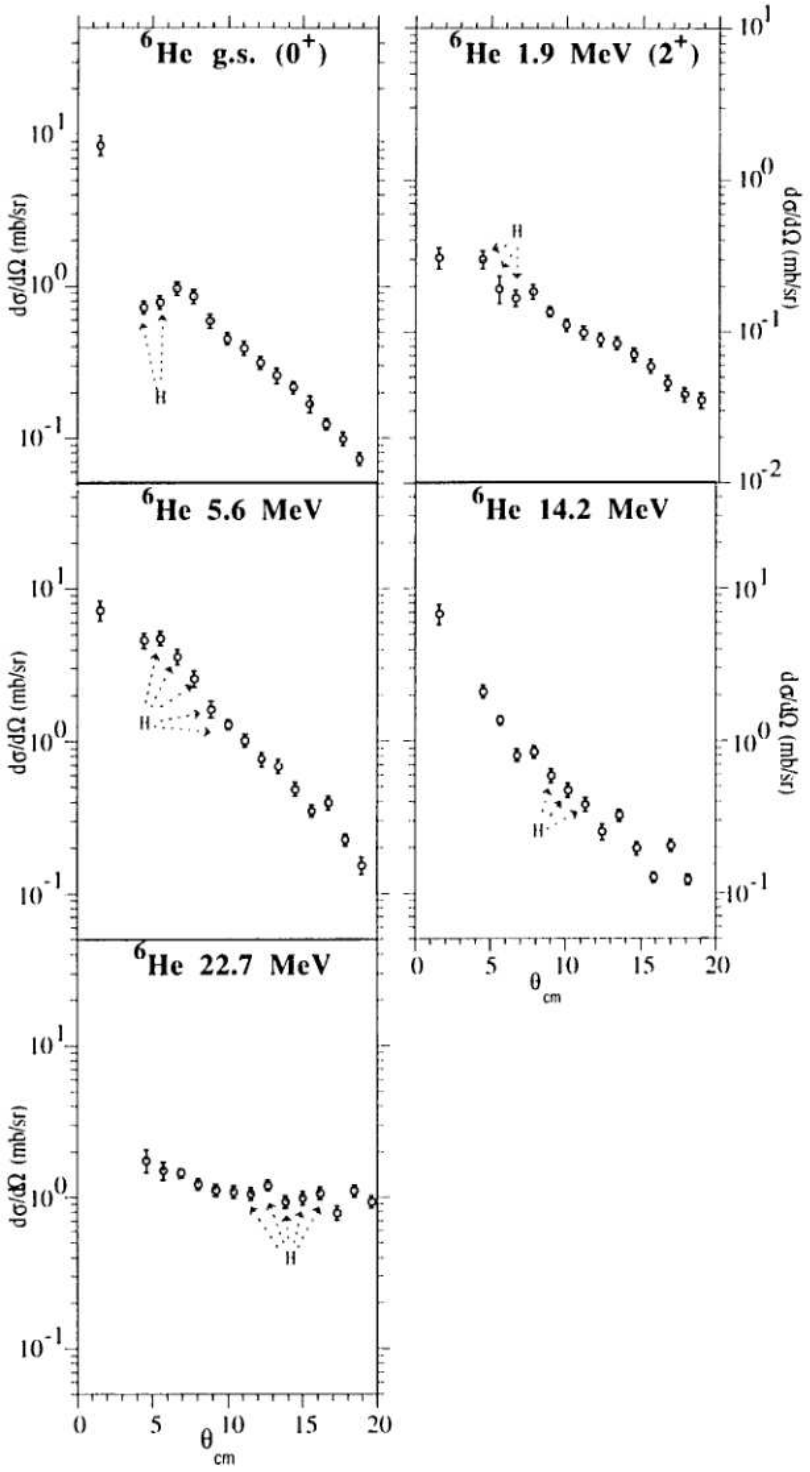

Figure 6.3 Angular distributions of the cross sections of states in ^{6}He.

6.1.2 The $^{12}C(^{7}Li,^{7}Be)^{12}B$ reaction

The figures 6.4(a) and 6.4(b) show the ^{7}Be singles spectra for the ^{12}C target. The spectra for ^{7}Be singles and coincidence with 430 keV γ-rays are shown in the figure 6.5. Six peaks are observed at excitation energies of 0.23±0.04 MeV, 2.2±0.1 MeV, 4.84±0.04 MeV, 6.93±0.05 MeV, 10.45±0.08 MeV, and 12.8±0.2 MeV. They have energy widths of 1.56±0.04 MeV, 2.6±0.1 MeV, 1.69±0.02 MeV, 2.89±0.09 MeV, 2.9±0.3 MeV, and 10.9±0.3 MeV, respectively. The peak at the 2.2 MeV is the superposition of several discrete states which could not be resolved due to the finite resolution of the spectrograph. Only for lab angles of 2 and 2.5 degrees a seventh peak was observed at excitation energy of 28.49±0.07 MeV with energy width of 1.0±0.1 MeV. ^{7}Be singles and coincidence cross sections for lab angle of 2 degree, average excitation energies and energy widths of states in ^{12}B are listed in table 6.2. The values $\frac{d\sigma^{coin.}}{d\Omega_{cm}}$ (corrected) are the coincidence cross sections corrected for the overall γ-ray detection efficiency, which was 11%.

The angular distributions of the cross sections for the states observed in ^{12}B are shown in the figure 6.6. As mentioned before, the zero degree cross sections were renormalized by a factor of 1.844 based on the 0^{o} cross section for the transition to the ^{12}B ground state and the comparison to the calculated angular distribution which was otherwise found to be well described by the DWBA analysis (see section 8.2). The uncorrected zero-degree cross section was used only for the ^{12}B ground state. It was assigned an estimated uncertainty of 85%. Uncertainties of 10% were assumed for all other singles cross sections estimated from the fitting procedure (see section 6.1.1).

E_x (MeV)	Γ (MeV) (FWHM)	$\frac{d\sigma^{sing.}}{d\Omega_{cm}}$ (mb/sr)	$\frac{d\sigma^{coin.}}{d\Omega_{cm}}$ (mb/sr)	$\frac{d\sigma^{coin.}}{d\Omega_{cm}}$ Corrected. (mb/sr)	$\frac{d\sigma/d\Omega_{corr.}^{coin.}}{d\sigma/d\Omega^{sing.}}$
gs		1.424	0.065	0.591	0.42
2.2±0.1 (17.3)	2.1±0.1	0.655	0.029	0.264	0.40
4.84±0.04 (19.94)	0.65±0.02	1.835	0.081	0.736	0.40
6.93±0.05 (22.03)	2.43±0.09	1.858	0.075	0.682	0.37
10.45±0.08 (25.55)	2.4±0.3	1.478	0.026	0.236	0.16
12.8±0.02 (27.9)	10.8±0.3	3.651	0.213	1.936	0.53

Table 6.2 States in ^{12}B (present work). (See table 6.1 caption).

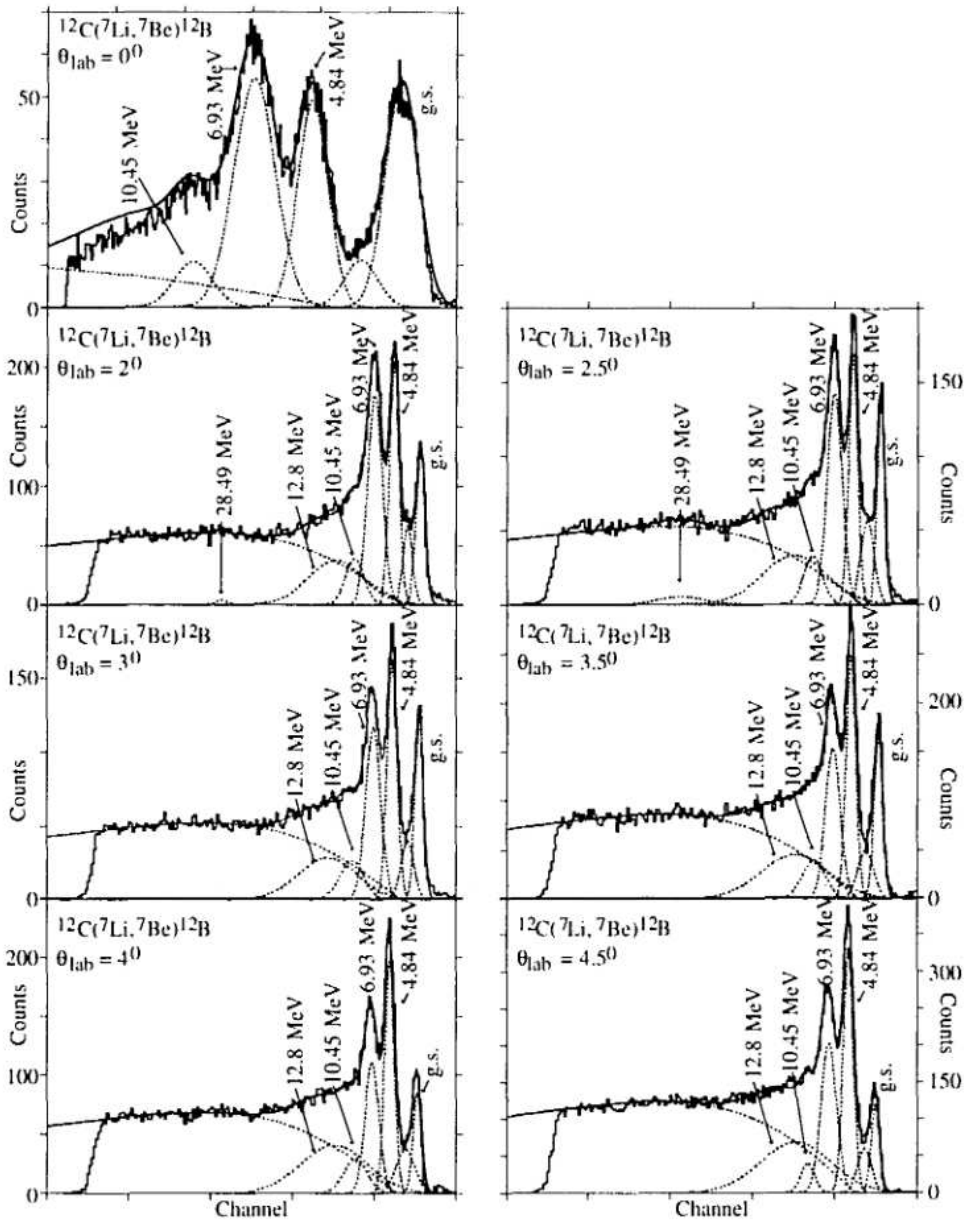

Figure 6.4(a) ^{7}Be singles spectra for ^{12}C target at lab angles of 0.0 to 4.5 degree.

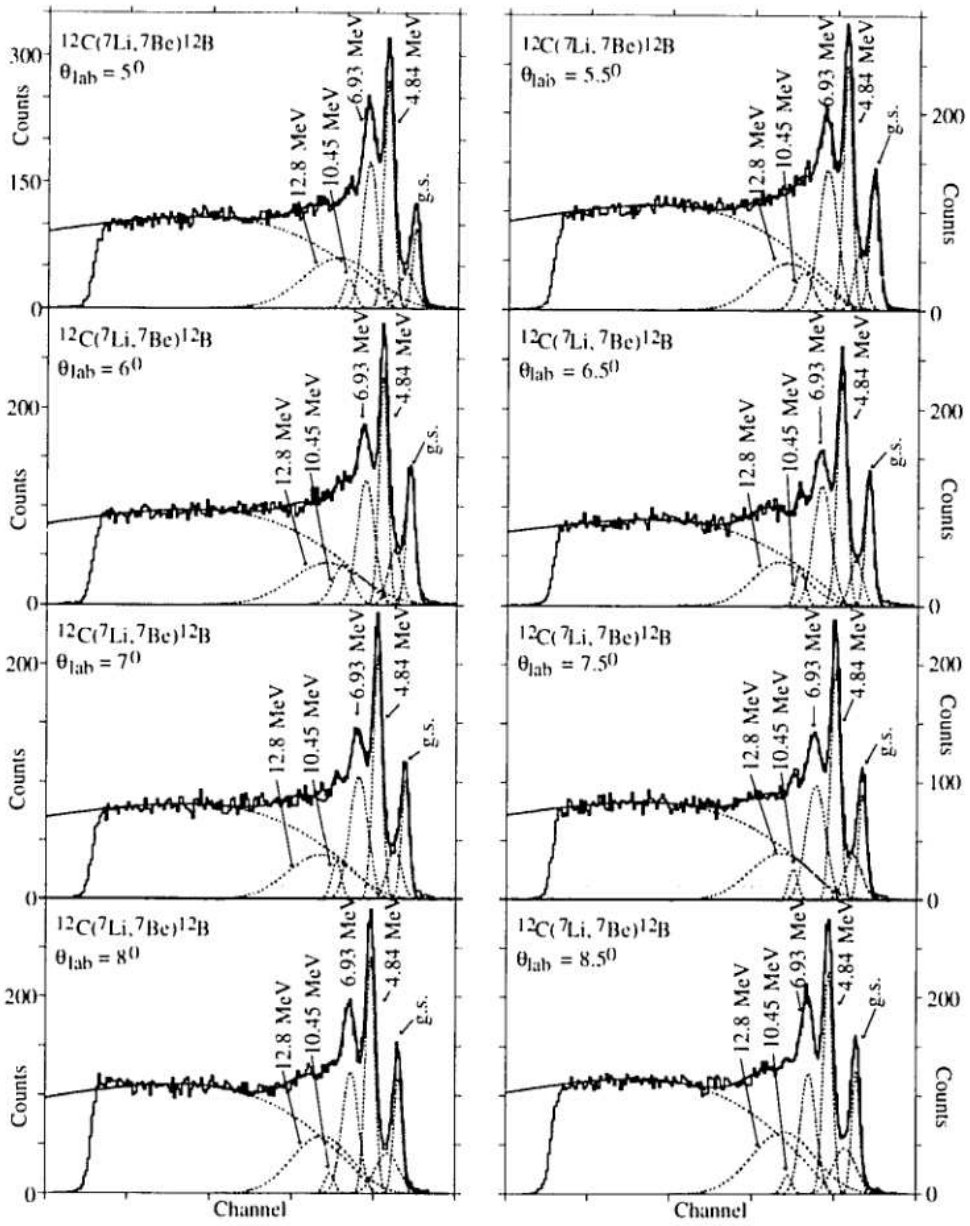

Figure 6.4(b) ^{7}Be singles spectra for ^{12}C target at lab angles of 5.0 to 8.5 degree.

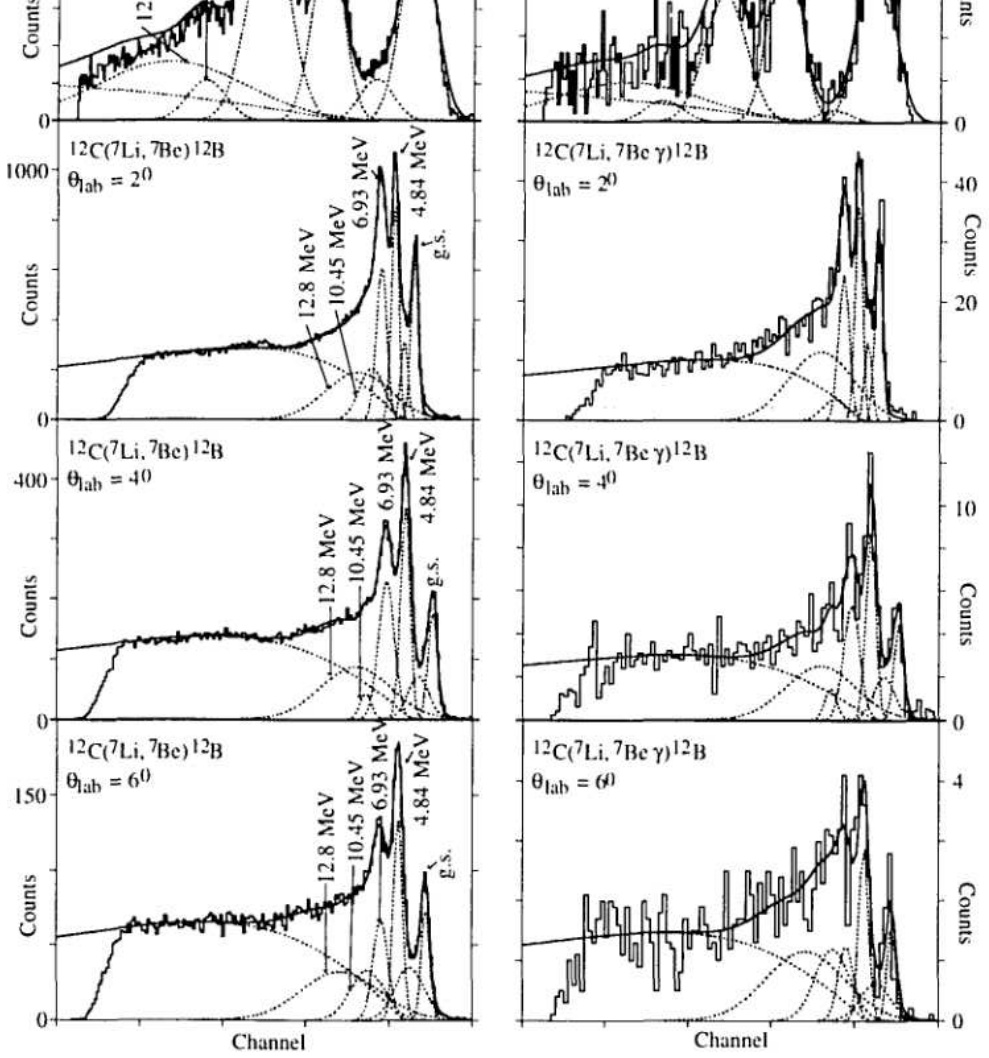

Figure 6.5 ^{7}Be singles and coincidence spectra for ^{12}C target at lab angles of 0.0 to 6.0 degree.

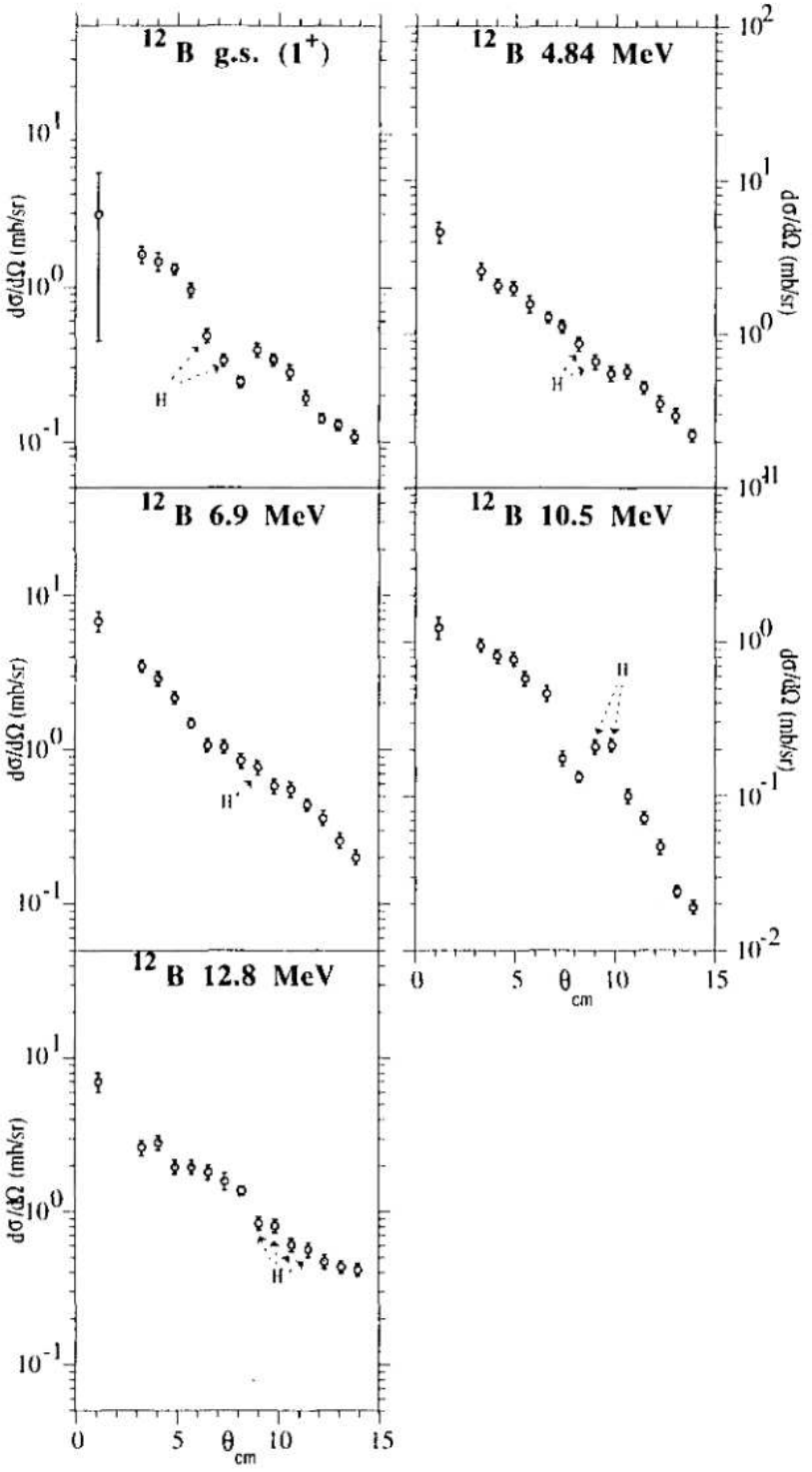

Figure 6.6 Angular distributions of the cross sections of states in ^{12}B.

6.1.3 The $^{90}Zr(^{7}Li,^{7}Be)^{90}Y$ reaction

The figure 6.7 shows the ^{7}Be singles and coincidence spectra for ^{90}Zr target at lab angle of 2 degree. Data were taken only for lab angle of 2 degree because the event rate for the heavier targets was quite low. Therefore, the statistics for the coincidence spectra is very poor. Four peaks are observed at excitation energies of 3.5±0.4 MeV, 6.1±0.3 MeV, 10.0±0.5 MeV, and 16.1±0.8 MeV with energy widths of 3.5±0.5 MeV, 9.4±0.9 MeV, 11±1 MeV, and 18±2 MeV, respectively. ^{7}Be singles and coincidence cross sections for lab angle of 2 degree, excitation energies and energy widths of states in ^{90}Y are listed in table 6.3. The values $\frac{d\sigma^{coin.}}{d\Omega_{cm}}$ (corrected) are the coincidence cross sections corrected for the γ-ray detection efficiency, which was 9%. These cross sections are uncertain to at least a factor of two because of the limited statistics. For heavier targets, the uncertainties of coincidence cross sections are as large as about 70%. Centroid energies and widths for the coincidence spectra were fixed at the values from the singles spectra.

E_x (MeV)	Γ (MeV) (FWHM)	$\frac{d\sigma^{sing.}}{d\Omega_{cm}}$ (mb/sr)	$\frac{d\sigma^{coin.}}{d\Omega_{cm}}$ (mb/sr)	$\frac{d\sigma^{coin.}}{d\Omega_{cm}}$ Corrected. (mb/sr)	$\frac{d\sigma/d\Omega_{corr.}^{coin.}}{d\sigma/d\Omega^{sing.}}$
3.5±0.4 (16.6)	3.1±0.5	1.096	0.0986	1.096	1.00
6.1±0.3 (19.2)	9.3±0.9	3.878	0.1425	1.5833	0.41
10.0±0.5 (23.1)	11±1	7.781	0.2266	2.5178	0.32
16.1±0.8 (29.2)	17±2	18.241	0.3153	3.503	0.19

Table 6.3 States in ^{90}Y (present work). (See table 6.1 caption).

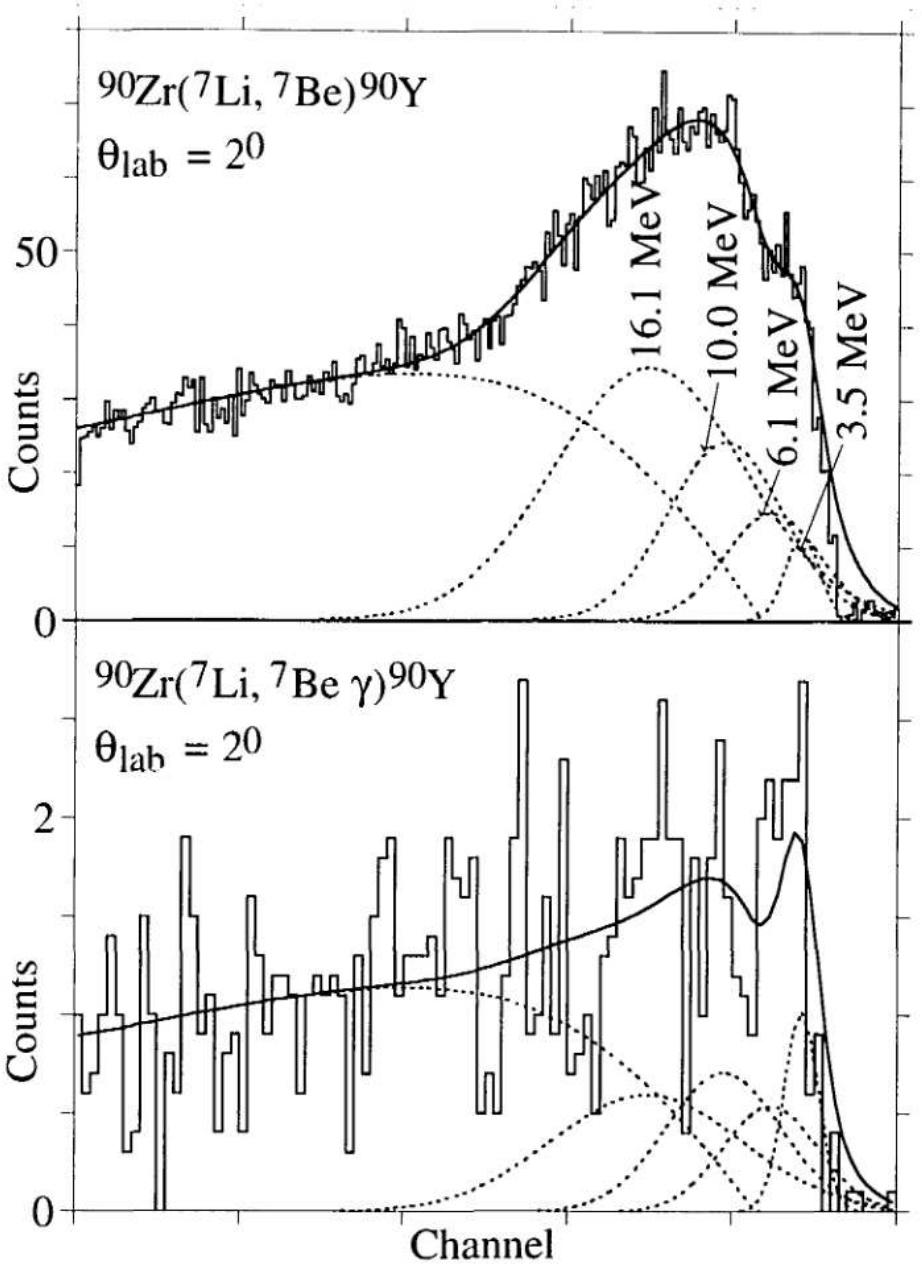

Figure 6.7 ^{7}Be singles and coincidence spectra for ^{90}Zr target at lab angle of 2 degree.

6.1.4 The ^{120}Sn(^{7}Li,^{7}Be)^{120}In

The ^{120}Sn (^{7}Li,^{7}Be)^{120}In reaction was performed at lab angles of 2 - 6 degrees in 1 degree steps. The ^{7}Be singles spectra are shown in the figure 6.8. Figure 6.9 shows the ^{7}Be singles and coincidence spectra. Four peaks are seen at excitation energies of 1.12±0.09 MeV, 6.0±0.2 MeV, 11.5±0.5 MeV, and 17.2±0.3 MeV. They have energy widths of 2.0±0.2 MeV, 5.4±0.7 MeV, 9.3±0.8 MeV, and 17±1 MeV, respectively. ^{7}Be singles and coincidence cross sections for lab angle of 2 degree, average excitation energies and energy widths of states in ^{120}In are listed in table 6.4. The values $\frac{d\sigma^{coin.}}{d\Omega_{cm}}$ (corrected) are the coincidence cross sections corrected for the γ-ray detection efficiency, which was 9%.

The angular distributions of the cross sections of the states observed in ^{120}In are shown in the figure 6.10. Relative uncertainties of 10% were estimated for all singles cross sections from the uncertainties of the fitting procedure. The cross sections observed in coincidence have again large uncertainties because of the limited statistics.

E_x (MeV)	Γ (MeV) (FWHM)	$\frac{d\sigma^{sing.}}{d\Omega_{cm}}$ (mb/sr)	$\frac{d\sigma^{coin.}}{d\Omega_{cm}}$ (mb/sr)	$\frac{d\sigma^{coin.}}{d\Omega_{cm}}$ Corrected. (mb/sr)	$\frac{d\sigma/d\Omega_{corr.}^{coin.}}{d\sigma/d\Omega^{sing.}}$
1.12±0.09 (19.42)	1.3±0.2	1.147	0.0411	0.4567	0.40
6.0±0.2 (24.3)	5.2±0.7	4.460	0.1846	2.0511	0.46
11.5±0.5 (29.8)	9.1±0.8	7.918	0.1750	1.9444	0.25
17.2±0.3 (35.5)	17±1	12.717	0.6068	6.742	0.53

Table 6.4 States in ^{120}In (present work). (See table 6.1 caption).

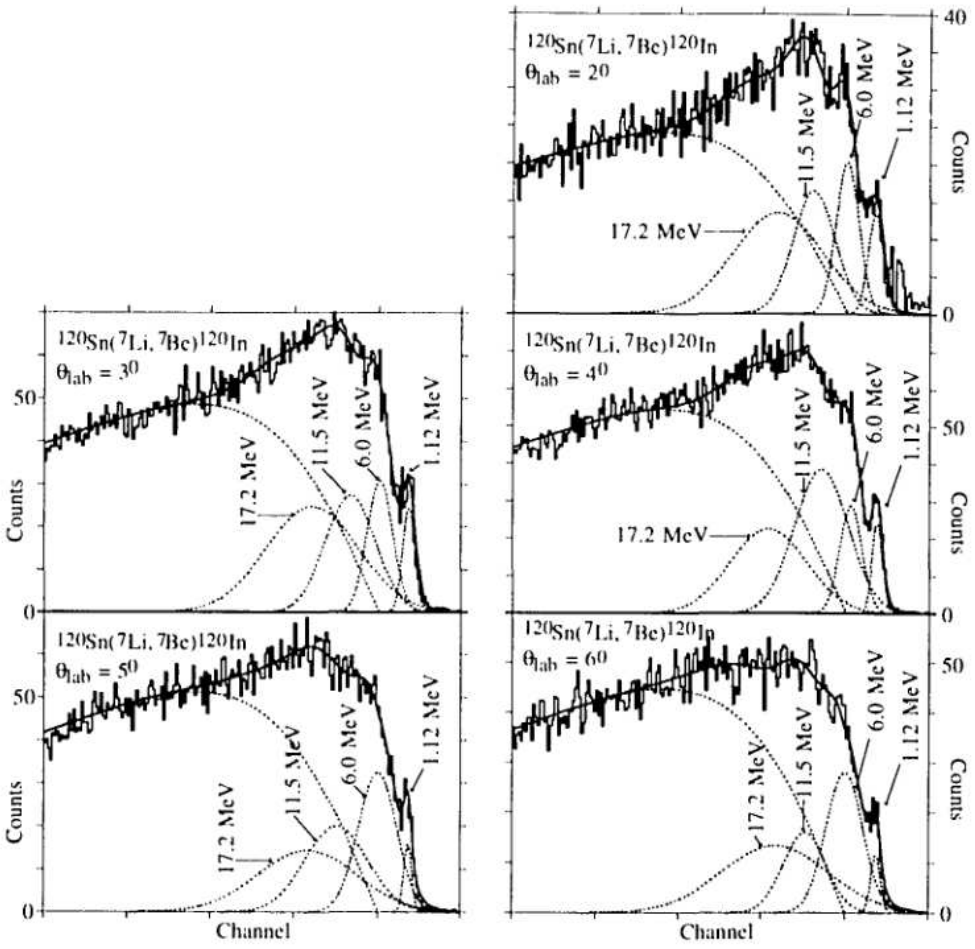

Figure 6.8 ^{7}Be singles spectra for ^{120}Sn target at lab angles of 2.0 to 6.0 degree.

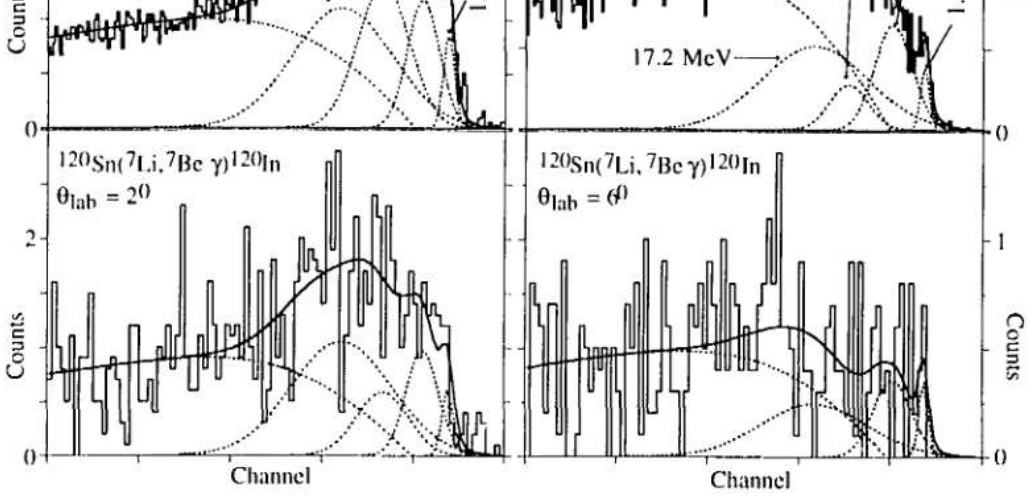

Figure 6.9 ^{7}Be singles and coincidence spectra for ^{120}Sn target at lab angles of 2.0 and 6.0 degree.

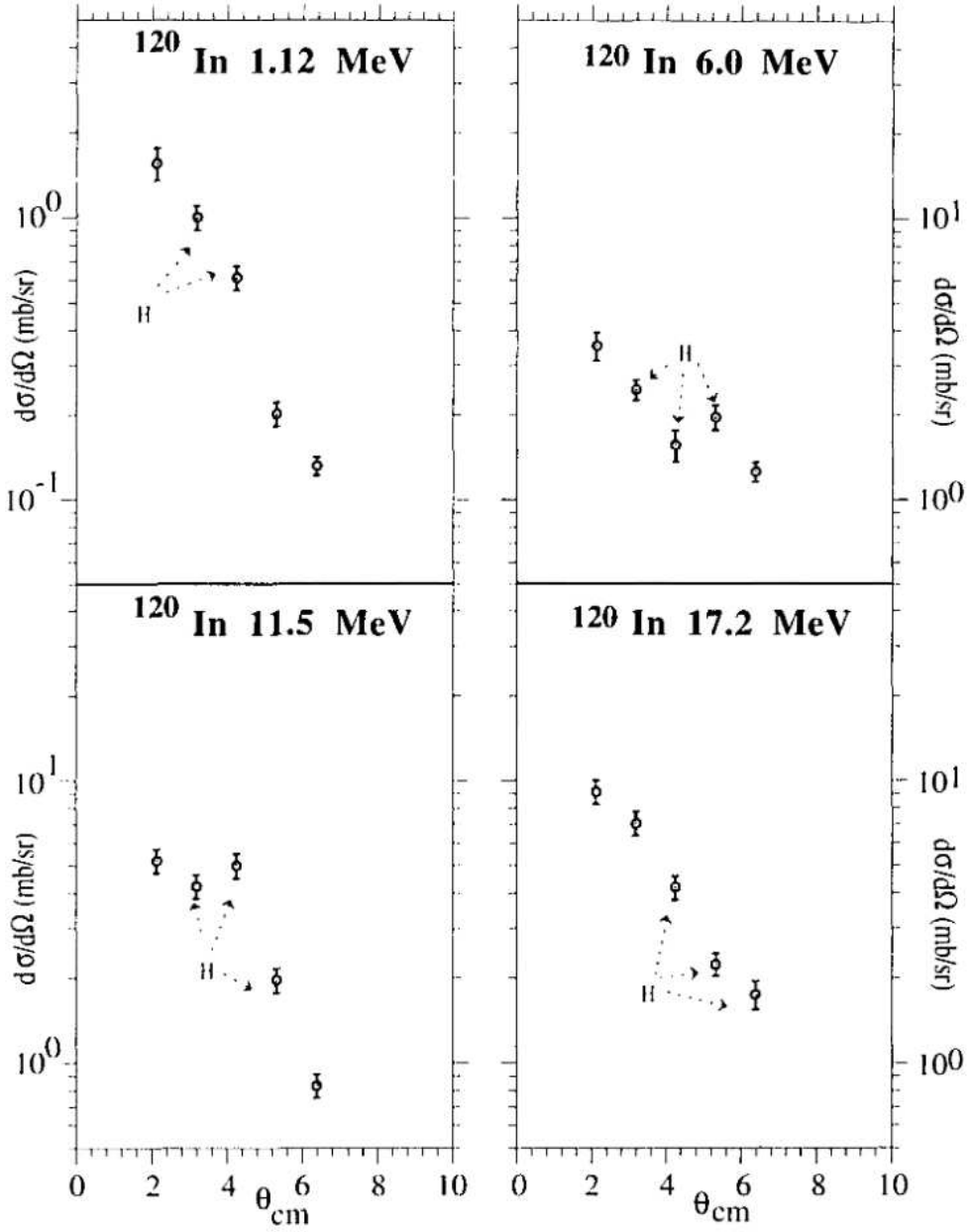

Figure 6.10 Angular distributions of the cross sections of states in ^{120}In.

6.1.5 The $^{208}Pb(^{7}Li,^{7}Be)^{208}Tl$ reaction

The ^{7}Be singles and coincidence spectra obtained at the lab angle of 2° for the ^{208}Pb target are shown in the figure 6.11. Six peaks are observed at excitation energies of 0.0 MeV, 2.7±0.3 MeV, 5.1±0.3 MeV, 8.0±0.4 MeV, 13.0±0.7 MeV, and 20±1 MeV. They have energy widths of 2.9±0.4 MeV, 4.4±0.7 MeV, 3.8±0.4 MeV, 4.2±0.4 MeV, 8.3±0.8 MeV, and 8.3±0.8 MeV, respectively. ^{7}Be singles and coincidence cross sections for lab angle of 2 degree, excitation energies and energy widths of states in ^{208}Tl are listed in table 6.5. The values $\frac{d\sigma^{coin.}}{d\Omega_{cm}}$ (corrected) are the coincidence cross sections corrected for the γ-ray detection efficiency, which was 9%. The limited statistics again affects the uncertainties of the coincidence cross sections.

E_x (MeV)	Γ (MeV) (FWHM)	$\frac{d\sigma^{sing.}}{d\Omega_{cm}}$ (mb/sr)	$\frac{d\sigma^{coin.}}{d\Omega_{cm}}$ (mb/sr)	$\frac{d\sigma^{coin.}}{d\Omega_{cm}}$ Corrected. (mb/sr)	$\frac{d\sigma/d\Omega_{corr.}^{coin.}}{d\sigma/d\Omega^{sing.}}$
gs		2.9045	0.0265	0.2944	0.10
2.7±0.3 (25.6)	4.1±0.7	4.8297	0.1961	2.1789	0.45
5.1±0.3 (28.0)	3.5±0.4	2.8236	0.0430	0.4778	0.17
8.4±0.4 (31.3)	3.9±0.4	3.6342	0.1133	1.2589	0.35
13.0±0.7 (35.9)	8.1±0.8	11.6104	0.0868	0.9644	0.08
20±1 (42.9)	8.2±0.8	4.4590	0.1114	1.2378	0.28

Table 6.5 States in ^{208}Tl (present work). (See table 6.1 caption).

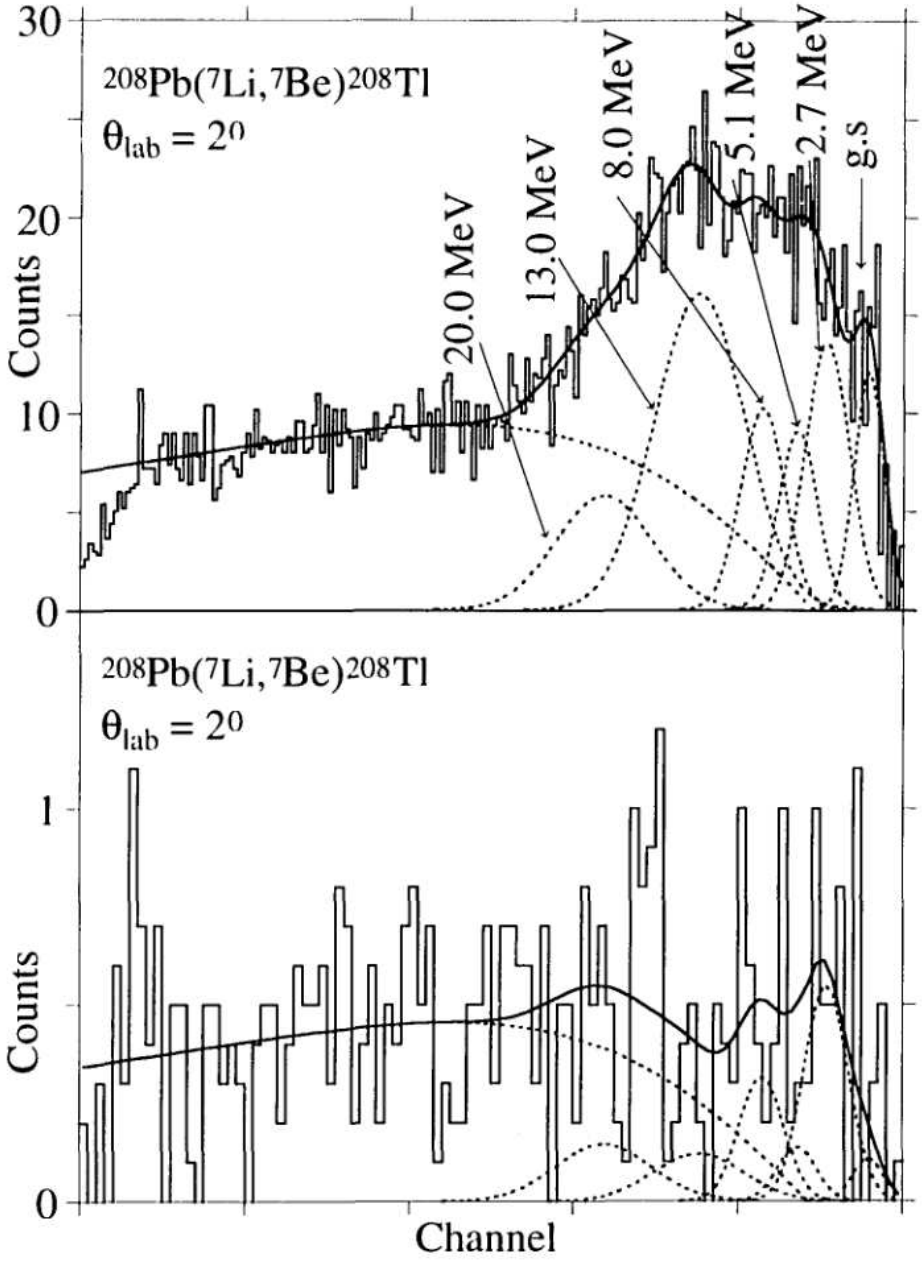

Figure 6.11 ^{7}Be singles and coincidence spectra for ^{208}Pb target at lab angle of 2 degree.

6.2 General comments

The states observed in ^{6}He, ^{12}B, ^{90}Y, ^{120}In, and ^{208}Tl nuclei will be compared with other published data in the chapter 8. The spin-flip and non-spin-flip components of the transitions can in principle be decomposed using the method described in section 7.3. In the present work, this decomposition was not performed due to two reasons: (1) the coincidence spectra for the heavier targets contain not only the ^{7}Be events in coincidence with 430 keV γ-rays, but also some ^{7}Be events in coincidence with fast neutrons and γ-rays from the deexcitation of the residual nucleus; (2) the statistics of most coincidence spectra are not good enough to perform a statistically meaningful decomposition. However, almost the same information can be extracted from the cross section ratios listed in the last column of tables 6.1 to 6.5.

CHAPTER 7

THEORETICAL CONSIDERATIONS

7.1 Operator formalism for giant resonances

Giant resonances are microscopically described as the coherent superposition of single particle-hole excitations of a nucleus. Single-particle and single-hole excitations can be described with operators acting on the ground states of nuclei.

The general form of the isoscalar, non-spin-flip excitation operator for $\Delta l > 1$ transitions can be given by [Blomgren, 1991]

$$Q_m^l = \sum_i r_i^l Y_m^l(\theta_i, \phi_i). \tag{7.1}$$

The summation runs over all nucleons, and l is the multipolarity of the transition. If the spin operator, σ, is also taken into account, the isoscalar, spin-flip operator for $l > 1$ can be written as

$$Q_m^l = \sum_i r_i^l Y_m^l(\theta_i, \phi_i)\sigma_i. \tag{7.2}$$

The general form of the isoscalar monopole operator can be written as

$$Q = \sum_i r_i^2 Y_0^0. \tag{7.3}$$

The operator with the zeroth radial order gives the initial state back. Hence the lowest order of the radial component for isoscalar monopole transitions is 2. The isoscalar, spin-flip monopole operator can be obtained by inserting the spin operator, σ.

For isoscalar dipole transitions the operator has a general form of

$$Q_m^l = \sum_i r_i^3 Y_m^l(\theta_i, \phi_i). \tag{7.4}$$

Since the first radial order gives the translation of the center of mass (that is a spurious center of mass motion), the lowest order of the radial component for isoscalar dipole transitions is 3.

The isovector, non-spin-flip transition operator for $\Delta l > 0$ transitions is of the form

$$Q_m^l = \sum_i r_i^l Y_m^l(\theta_i, \phi_i)\tau_i^{\pm}. \tag{7.5}$$

The operators $\tau^{\pm}$ correspond to isospin-raising and isospin-lowering, respectively. The isovector, non-spin-flip monopole operator is of the form

$$Q = \sum_i r_i^2 Y_0^0 \tau_i^{\pm}. \tag{7.6}$$

If the spin operator, σ, is also taken into account, the isovector, spin-flip operator can be written as

$$Q_m^l = \sum_i r_i^l Y_m^l(\theta_i, \phi_i)\sigma_i \tau_i^{\pm}. \tag{7.7}$$

Since the charge-exchange reactions are isovector transitions, the corresponding operators are either the isovector, spin-flip operator given by the equation (7.7) or the isovector, non-spin-flip operators given by the equations (7.5) and (7.6).

Nuclear β-decay is an isovector transition since the charge of the nucleus is changed by one unit. The allowed Fermi ($\Delta L = 0$, $\Delta S = 0$) β-decay transition operator has the form

$$Q = \sum_i \tau_i^{\pm}, \tag{7.8}$$

and the allowed Gamow-Teller ($\Delta L = 0$, $\Delta S = 1$) β-decay transition operator has the form

$$Q = \sum_i \sigma_i \tau_i^{\pm}. \tag{7.9}$$

The first forbidden Fermi and Gamow-Teller β-decay transition operators can be obtained by substituting $l = 1$ in the equations (7.5) and (7.7), respectively.

Figure 7.1 shows a schematic representation of charge-exchange operators acting on the ground state of a nucleus. The operators Q_-^l and Q_+^l are isospin-lowering and isospin-raising operators, respectively.

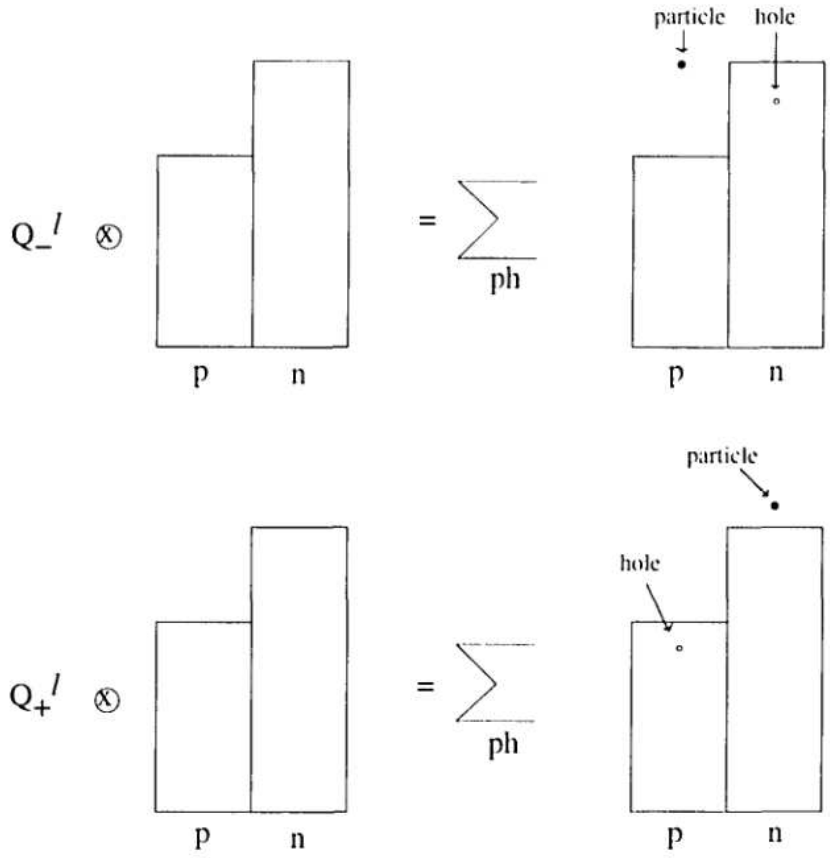

Figure 7.1 The isospin-lowering and isospin-raising operators acting on the ground state of a nucleus.

The transition strength of a giant resonance is the sum of the single-particle and single-hole transition strengths. The sum rules provide a measure of the transition strengths. The energy-weighted sum rule is defined by allowing the operators to act on the ground state and summing over all the states reached by them. The energy-weighted sum rule can be given by [Satchler, 1983]

$$\tilde{S}^{l} = (2l+1)\sum_{f}(E_f - E_0)\left\langle f\left\|Q^{l}\right\|i\right\rangle^{2}. \qquad (7.10)$$

The summation runs over all the states with multipolarity l. These sums are approximately independent of the nuclear structure. Hence the energy-weighted sum rule is almost model independent.

7.2 Reaction mechanism

7.2.1 Optical model

The study of the interaction of two nuclei is a complicated, multi-faceted problem. The optical model is introduced to simplify this problem. In this model, the interaction among nucleons in nuclei has been replaced by an average potential which is known as the optical potential. Consequently the interaction of two nuclei is replaced by a structureless particle moving in a potential well. The name "optical" refers to the similarity of the treatment to that of the scattering of light waves by a reflecting and absorbing sphere.

In the elastic scattering of particles, only the elastic channel is populated. In the non-elastic scattering, the non-elastic channels will also be populated, but there will be a loss of flux in the elastic channel. The removal of flux into non-elastic reaction channels is known as absorption. Hence the optical potential must be absorptive in the presence of non-elastic scattering. In other words, potential is complex; the real part corresponds to the scattering and the imaginary part corresponds to the absorption.

The optical potential is usually defined as [Perey, 1976]

$$U(r) = -Vf(x) + \left(\frac{\hbar}{m_\pi c}\right)^{2} V_{so}(\sigma.l)\frac{1}{r}\frac{d}{dr}f(x_{so}) - i\left(Wf(x_w) - 4W_D\frac{d}{dx_D}f(x_D)\right) + V_c(r). \qquad (7.11)$$

The functions $f(x_i)$ are usually given by

$f(x_i) = (1+e^{x_i})^{-1}$, where $x_i = (r - r_i A^{1/3})/a_i$.

The functions $f(x)$, $f(x_W)$, $f(x_{SO})$ and $f(x_D)$ are Wood-Saxon potential form factors for real, volume absorptive, spin-orbit and surface absorptive terms, respectively with the

corresponding radius and diffusivity parameters. The parameters V, V_{so}, W, and W_D represent the strength of the real, spin-orbit, volume absorptive, and surface absorptive potentials, respectively.

The quantity $V_c(r)$ is the Coulomb potential of a spherical uniform charge distribution of radius R_c, where $R_c = r_c A^{1/3}$, r_c is the Coulomb radius parameter, and A is the mass number of the target nucleus. The factor $A^{1/3}$ is sometimes replaced by $(A_1^{1/3} + A_2^{1/3})$ for heavy ions where A_1 and A_2 are the mass numbers of incident and target nuclei, respectively. The Coulomb potential V_c is given by

$$V_c = \frac{ZZ'e^2}{r} \quad ; r \geq R_c \tag{7.12}$$

$$V_c = \frac{ZZ'e^2}{2R_c}\left(3 - \frac{r^2}{R_c^2}\right) \quad ; r \leq R_c . \tag{7.13}$$

Furthermore,

$$\left(\hbar/m_\pi c\right)^2 \approx 2.000\, fermi^2$$

where m_π is the pion mass. The $\sigma.l$ operator is defined in terms of the spin angular momentum. The parameters V, r, a, W, r_w, a_w, W_D, r_D, a_D, V_{so}, r_{so}, a_{so}, and r_c are known as optical model parameters. They are usually obtained by fitting experimental elastic scattering cross sections.

7.2.2 Distorted-wave Born approximation

A particle of mass m and energy E scattering under a potential V(r) satisfies the Schrödinger equation

$$\left(\frac{-\hbar^2}{2m}\nabla^2 + V(r)\right)\chi_k(r) = E\chi_k(r). \tag{7.14}$$

This expression can be rearranged as

$$(\nabla^2 + k^2)\chi_k(r) = U(r)\chi_k(r) = F(r). \tag{7.15}$$

Here, $k^2 = \frac{2mE}{\hbar^2}$ and $U = \frac{2mV}{\hbar^2}$. If V = 0, then the equation (7.14) will take the form

$$(\nabla^2 + k^2)\chi_k(r) = 0. \tag{7.16}$$

This has the plane wave solution

$$\chi_k(r) = e^{ik.r}. \tag{7.17}$$

The potential V introduces scattered waves in addition to the incoming plane waves. The term F(r) can be considered as the source which generates the scattered waves. A solution to the equation (7.15) consists of the scattered waves generated by F(r) and any solution to the homogeneous equation (7.16). Therefore, $\chi(r)$ can be written as

$$\chi_k(r) = e^{ik.r} - \frac{1}{4\pi}\int dr' \frac{e^{ik|r-r'|}}{|r-r'|} U(r')\chi(k,r'). \tag{7.18}$$

For large r ,

$$\frac{1}{|r-r'|} \approx \frac{1}{r} \quad \text{and} \quad k|r-r'| \approx kr - k'.r'.$$

Here, k' is the wave number of the scattered particle. Hence,

$$\chi_k(r) = e^{ik.r} - \frac{1}{4\pi}\frac{e^{ikr}}{r}\int dr' e^{-ik'.r'} U(r')\chi(k,r'). \tag{7.19}$$

The scattering amplitude, $f(\theta,\phi)$, is implicitly given by,

$$\chi_k(r) = e^{ik.r} + f(\theta,\phi)\frac{e^{ikr}}{r}. \tag{7.20}$$

Therefore,

$$f(\theta,\phi) = -\frac{1}{4\pi}\int dr'\, e^{-ik'.r'} U(r')\chi(k,r'). \tag{7.21}$$

The differential cross section is defined as

$$\frac{d\sigma}{d\Omega} = \left| f(\theta, \phi) \right|^2 . \tag{7.22}$$

If the potential V is weak, then the scattered wave has a small amplitude and can be considered as a perturbation. The wave-function $\chi(r')$ can be approximated as the first term of the equation (7.19). This is known as the plane wave Born approximation. The scattering amplitude then can be written as

$$f^{BA}(\theta, \phi) = -\frac{1}{4\pi} \int dr' \, e^{-ik'.r'} U(r') e^{ik.r'} . \tag{7.23}$$

If the differential cross-section for the reaction A(a,b)B is written as

$$\frac{d\sigma}{d\Omega} = \frac{\mu_\alpha \mu_\beta}{(2\pi\hbar^2)^2} \frac{k_\beta}{k_\alpha} |T|^2, \tag{7.24}$$

then the transition amplitude T will become

$$T^{BA} = \int d\tau \psi_B^* \psi_b^* e^{-ik_\beta . r_\beta} V \psi_A \psi_a e^{ik_\alpha . r_\alpha} . \tag{7.25}$$

Here α = A+a is the entrance channel, β = B+b is the exit channel, ψ_i are the wave-functions describing the internal state of nucleus i, V is the potential of interaction between the projectile and the target, and τ are the variables to be integrated over.

In general, the wave-functions in the nuclear interior, r < R (radius of the nucleus), are not plane waves, but the waves are distorted by inelastic scattering and absorption. Therefore, the $e^{ik_i . r_i}$ terms in the equation (7.25) should be replaced by the distorted-waves, $\chi(k_i, r_i)$. This is known as the distorted-wave Born approximation (DWBA). The transition amplitude is given by

$$T^{DWBA} = \int\int dr_\alpha dr_\beta \chi^{(-)}(k_\beta, r_\beta)^* \langle b, B|V|a, A\rangle \chi^{(+)}(k_\alpha, r_\alpha) \tag{7.26}$$

Here, V is the interaction between the projectile and the target. The matrix element $\langle b, B|V|a, A\rangle$ is known as the form factor, F(r), for the reaction. The form factor is calculated by folding the nucleon-nucleon interaction with the target and projectile transition densities. The distorted-waves can be expanded in partial wave series,

$$\chi_i^{(+)}(k_a, r) = \frac{4\pi}{k_a r} \sum_{L_a M_a} i^{L_a} \chi_{L_a}(k_a, r) Y_{L_a M_a}(\hat{r}) Y^*_{L_a M_a}(\hat{k}_a), \tag{7.27}$$

$$\chi_f^{(-)^*}(k_b, r) = \frac{4\pi}{k_b r} \sum_{L_b M_b} i^{-L_b} \chi_{L_b}(k_b, r) Y^*_{L_b M_b}(\hat{r}) Y_{L_b M_b}(\hat{k}_b). \tag{7.28}$$

In inelastic nucleon scattering, the form factor is calculated with the single-folding method while in inelastic heavy-ion scattering, it is calculated with the double-folding method. The interaction V is assumed to be the sum of an effective two-body nucleon-nucleon interaction $v_{p,t}$ over all the nucleons in the projectile and the target. Therefore, the interaction V can be given by

$$V = \sum_{p,t} v_{p,t}. \tag{7.29}$$

The nucleon-nucleon interaction consists of three main parts: central, tensor and spin-orbit. For charge-exchange reactions, in general, the spin-orbit part of the interaction produces negligible contribution to the cross section. The important parts of the interaction in charge-exchange reactions are the central and the tensor terms. The nucleon-nucleon interaction can by written as [Cook, 1984]

$$v_{p,t}(s) = \sum_{\substack{K=0,2 \\ ST}} v^K_{ST}(s) C^K_S Y_K(\hat{s}). [\sigma^s(p) \otimes \sigma^s(t)]^K \tau^T(p). \tau(t)^T \tag{7.30}$$

Here, K = 0 and 2 correspond to central and tensor, respectively. S and T are the spin and isospin labels of the force. The quantities C_S^K are constants. The vector **s** is the separation vector between the interacting nucleon pair. The operators σ and τ are the Pauli spin and isospin operators. The form factor $\langle b.B|V|a.A\rangle$ can be evaluated, from the work of Petrovich [Petrovich, 1977], as

$$\langle bB|v|aA\rangle = \sum_{\substack{J_R M_R \\ J_p M_p \\ J_t M_t}} i^{-J_R}(-1)^{J_b - M_b}\hat{J}_b \langle J_A J_t M_A M_t | J_B M_B\rangle \langle J_a J_b M_a, -M_b | J_p M_p\rangle \langle J_R J_p M_R M_p | J_t M_t\rangle$$

$$\times F_{M_R}^{J_R J_p J_t}(R) Y^*_{J_R M_R}(\hat{R}). \tag{7.31}$$

Here,

$$F_{M_R}^{J_R J_p J_t}(R) = \sum_{\substack{L_R L_p L_t \\ S T M_t K}} (4\pi)^{-1/2}(-1)^{J_a - J_b + J_p + L_t + S + M_T - K}\hat{L}_p\hat{L}_t\hat{S}\hat{L}_R\hat{J}_R \langle L_p L_t 00 | L_R 0\rangle \langle J_R L_R 00 | K 0\rangle$$

$$\times \begin{Bmatrix} L_p & S & J_p \\ L_t & S & J_t \\ L_R & K & J_R \end{Bmatrix} \frac{C_K}{2\pi^2}\int_0^\infty v_{ST}^K(k) F_{ba}^{L_p S J_p, T M_t}(k) F_{BA}^{L_t S J_t, T M_t}(k) j_{J_R}(kR) k^2 dk. \tag{7.32}$$

The quantities J_R, J_p and J_t denote the total angular momentum transfer to the relative motion, to the projectile motion and to the target motion, respectively. The quantities L_R, L_p and L_t denote the orbital angular momentum transfer to the relative motion, to the projectile motion and to the target motion, respectively. The quantities $v_{ST}^K(k)$ and $F_{fi}^{LSJ,TMT}(k)$ are the Fourier transforms of the interaction and the densities in the momentum space, which can be given by the equations (7.33) and (7.34).

$$v_{ST}^K(k) = 4\pi\int_0^\infty v_{ST}^K(s) j_K(ks) s^2 ds \tag{7.33}$$

$$F_{fi}^{LSJ,TM_T}(k) = 4\pi\int_0^\infty F_{fi}^{LSJ,TM_T}(r) j_L(kr) r^2 dr \tag{7.34}$$

The radial densities have the form

$$F_{fi}^{LSJ.TM_T}(r)=\sum_{j_f j_i} S_{TM_T}^{J}(j_f j_i)\left\langle l_f j_f \left\| T^{LSJ} \right\| l_i j_i \right\rangle u_{n_f l_f j_f}(r) u_{n_i l_i j_i}(r). \tag{7.35}$$

Here, $S_{TM_T}^{J}(j_f j_i)$ are the spectroscopic amplitudes in the isospin representation. The tensor $T_{M_J}^{LSJ}$ is formed from coupling $Y_{LM_L}(\hat{r})$ with σ^S. The spectroscopic amplitudes are defined by

$$S_{TM_T}^{J}(j_f j_i)=\frac{2^{1/2}\hat{j}_f}{\hat{j}}\left\langle f \left\| A_{TM_T}^{J} \right\| i \right\rangle. \tag{7.36}$$

Here,

$$A_{TM_T}^{J}(j_f j_i)=\sum_{\substack{m_f m_i \\ t_{Z_f} t_{Z_i}}} (-1)^{j_i - m_i + 1/2 - t_{Z_i}} \left\langle j_f j_i m_f, -m_i \middle| JM_J \right\rangle \left\langle \frac{1}{2}\frac{1}{2} t_{Z_f}, -t_{Z_i} \middle| TM_T \right\rangle a_{j_f m_f t_{Z_f}}^{+} a_{j_i m_i t_{Z_i}}. \tag{7.37}$$

From equations (7.26), (7.27), (7.28), (7.31) and (7.32) the transition amplitude can be written as

$$\begin{aligned} T=\frac{4\pi}{k_a k_b}(-1)^{J_b - M_b}\hat{J}_b \sum_{\substack{J_R J_p J_t \\ M_R}} \hat{J}_R \left\langle J_A J_t M_A, M_B - M_A \middle| J_B M_B \right\rangle \\ \times \left\langle J_R J_p M_R, M_a - M_b \middle| J_t M_B - M_A \right\rangle \left\langle J_a J_b M_a, -M_b \middle| J_p, M_a - M_b \right\rangle S_{J_R J_p J_t}^{M_R}(\theta). \end{aligned} \tag{7.38}$$

Here,

$$\begin{aligned} S_{J_R J_p J_t}^{M_R}(\theta)=\sum_{L_a L_b} i^{L_a - L_b - L_R}(2L_b+1)(4\pi)^{-1/2}\left\langle L_b J_R 00 \middle| L_a 0 \right\rangle \left\langle L_b J_R M_R, -M_R \middle| L_a 0 \right\rangle \\ \times \left[\frac{(L_b - M_R)!}{(L_b + M_R)!}\right]^{1/2} P_{L_b}^{M_R}(\theta) \int_0^\infty dr \chi_{L_b}(k_b, r) F_{M_R}^{J_R J_p J_t}(r) \chi_{L_a}(k_a, r). \end{aligned} \tag{7.39}$$

The differential cross section, finally, is given by [Satchler, 1983]

$$\frac{d\sigma}{d\Omega}=\frac{\mu_a \mu_b}{(2\pi\hbar^2)^2}\frac{k_b}{k_a}\frac{1}{(2J_a+1)(2J_A+1)}\sum_{\substack{M_A M_B \\ M_a M_b}} |T|^2. \tag{7.40}$$

Therefore,

$$\frac{d\sigma}{d\Omega} = \frac{1}{E_a E_b} \frac{k_b}{k_a} \frac{(2J_b+1)(2J_B+1)}{(2J_a+1)(2J_A+1)} \sum_{\substack{J_R J_p J_t \\ M_R}} \left| S^{M_A}_{J_R J_p J_t}(\theta) \right|^2 . \tag{7.41}$$

In the present work, the differential cross sections were calculated using the fully microscopic DWBA code FOLD [Cook, 1988] as described above. This code produces the direct and exchange double-folded potentials. This model includes the single nucleon knock-on exchange (SNKE) contributions to the potentials as well as the direct terms. The effective nucleon-nucleon interaction is assumed to be the free nucleon-nucleon scattering amplitude, often known as the t matrix. The effective nucleon-nucleon interaction can be given by

$$v_{p,t}(s) = t_{nn}(E,q)\delta(r_s). \tag{7.42}$$

Here, E is the bombarding energy, q is the momentum transfer, and t_{nn} is the free nucleon-nucleon t matrix element. The nucleon-nucleon interaction $v_{p,t}$ is given by equation (7.30). Figure 7.2 shows the energy dependence of the magnitude of the central part of nucleon-nucleon t matrix [Love, 1981]. The quantities t_0^c, t_σ^c, t_τ^c, and $t_{\tau\sigma}^c$ denote the central parts of the nucleon-nucleon t matrix elements for the isoscalar non-spin-flip, the isoscalar spin-flip, the isovector non-spin-flip, and the isovector spin-flip transitions, respectively. The quantity E_p is the energy of the projectile.

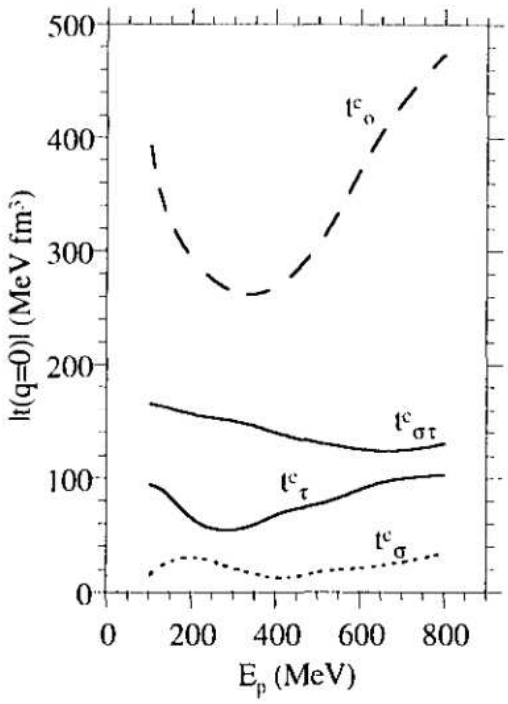

Figure 7.2 Energy dependence of the magnitude of the central part of the nucleon-nucleon t matrix. (From [Love, 1981]).

The ratio $\frac{t^c_{\sigma\tau}}{t^c_\tau}$ indicates that spin-flip excitations dominate over non-spin-flip excitations in the charge-exchange reactions for small angles near q = 0 at bombarding energies E_p>100 MeV. At lower energies the strength of isovector non-spin-flip excitations becomes comparable to that of isovector spin-flip excitations. The bombarding energy of the present work is 350 MeV or 50 MeV/u, where the ratio $\left|\frac{t^c_{\sigma\tau}}{t^c_\tau}\right|^2$ is about 1.

7.3 Nuclear structure consideration

The (^{7}Li,^{7}Be) charge-exchange reaction is a useful spectroscopic tool to investigate the isovector giant resonances for several reasons: (a) ^{7}Li and ^{7}Be are mirror nuclei, and all energy states are isobaric analog states; (b) the first excited state of ^{7}Be at 0.429 MeV is the only particle stable excited state, and the high-lying states decay by the emission of ^{3}He, α and protons; the 0.429 MeV state of ^{7}Be has the mean lifetime, τ_m, of 192 $\pm$ 25 fsec

[Ajzenberg-Selove, 1988] and decays by emission of γ-rays; (c) the (^{7}Li,^{7}Be) reactions selectively excite isovector resonances with ΔT_z=+1.

^{7}Li and ^{7}Be ground states have spin and parity of 3/2$^-$. The ^{7}Be excited state at 0.429 MeV has spin and parity 1/2$^-$. Therefore, transitions to the ^{7}Be ground state has both spin-flip and non-spin-flip components, while the transitions to the ^{7}Be excited state is a pure spin-flip transition. The cross sections of the transitions to the ^{7}Be ground state and the ^{7}Be excited state can be given by the equations (7.43) and (7.44).

$$\sigma(^7Be_{gs}) = B_{gs}(F)\sigma(\Delta S = 0) + B_{gs}(GT)\sigma(\Delta S = 1) \tag{7.43}$$

$$\sigma(^7Be_{ex}) = B_{ex}(GT)\sigma(\Delta S = 1) \tag{7.44}$$

Here, B(F) and B(GT) are Fermi and Gamow-Teller β-decay matrix elements, respectively. They can be obtained from the experimental log ft values for the respective β-decays. Since ^{7}Be(ε)^{7}Li is a superallowed β^- transition (electron capture),

$B_{gs}(F) = 2T = 1$.

The log ft values for the transitions to the ^{7}Be ground state and the ^{7}Be first excited state are 3.32 and 3.55, respectively [Ajzenberg-Selove, 1988]. The log ft value for the ^{7}Be excited state is obtained from the mirror transition ^{7}Be (1/2$^-$) -> ^{7}Li (3/2$^-$). The B(GT) values are calculated using the equation [Chou, 1993]

$$ft = \frac{6139 \pm 7}{B(F) + (1.264 \pm 0.002)^2 B(GT)}. \tag{7.45}$$

Therefore, the $B_{gs}(GT) = 1.213 \pm 0.006$ and $B_{ex}(GT) = 1.083 \pm 0.005$. The equations (7.43) and (7.44) can then be written as

$$\sigma(^7Be_{gs}) = \sigma(\Delta S = 0) + (1.213 \pm 0.006)\sigma(\Delta S = 1) \tag{7.46}$$

$$\sigma(^7Be_{ex}) = (1.083 \pm 0.005)\sigma(\Delta S = 1). \tag{7.47}$$

The ^{7}Be particles from the (^{7}Li,^{7}Be) reaction measured in coincidence with 430 keV γ-rays consist of only the transitions to the ^{7}Be excited state, while the ^{7}Be measured in singles consist of the transitions to the ^{7}Be ground state and the excited state. Therefore, the ratio of the cross sections of ^{7}Be coincidence to ^{7}Be singles can be given by

$$\frac{\sigma(coincidence)}{\sigma(singles)} = \frac{\sigma(^7Be_{ex})}{\sigma(^7Be_{gs}) + \sigma(^7Be_{ex})}. \tag{7.48}$$

Therefore,

$$\frac{\sigma(coincidence)}{\sigma(singles)} = \frac{(1.083 \pm 0.005)\sigma(\Delta S = 1)}{\sigma(\Delta S = 0) + (2.296 \pm 0.008)\sigma(\Delta S = 1)}. \tag{7.49}$$

For non-spin-flip transitions, $\sigma(\Delta S = 1) = 0$. Therefore,

$$\frac{\sigma(coincidence)}{\sigma(singles)} = 0, \tag{7.50}$$

and for spin-flip transitions, $\sigma(\Delta S = 0) = 0$. Therefore,

$$\frac{\sigma(coincidence)}{\sigma(singles)} = 0.472 \pm 0.003. \tag{7.51}$$

The spin-flip and non-spin-flip contributions to the resonances can therefore be decomposed by measuring the ^{7}Be in coincidence with 0.43 MeV γ-rays which gives the cross section of the transition ^{7}Li -> ^{7}Be$_{ex}$, the quantity $\sigma(^7Be_{ex})$.

CHAPTER 8

DISCUSSION AND DWBA ANALYSIS

8.1 Comparison between observed and known states in the residual nuclei

The results from the present work will be compared with the other published data in this section. The ratios of coincidence to singles cross sections of the states observed in the present work will also be discussed. The ratios are listed in tables 6.1 to 6.5 (see chapter 6). Tables 8.1 to 8.5 list the excitation energies and energy widths of the states observed in the present work, and the known excitation energies and spin and parity assignments from other work. The excitation energies are given relative to the ground states of the residual nuclei. The listed widths include the corrections from the experimental energy resolution of the spectrograph.

8.1.1 The ^{6}Li(^{7}Li,^{7}Be)^{6}He reaction

The states observed in ^{6}He are listed in table 8.1. The coincidence to singles ratios for the 0^{+} ground state and the 2^{+} state at 1.9 MeV are 46% and 44%, respectively (see table 6.1). Therefore, transitions to these states are identified as pure spin-flip transitions in agreement with the known spin-parity assignments including that of the 1^{+} ground state of ^{6}Li. The resonances at 5.6 MeV and 14.2 MeV have coincidence to singles ratios of 38%. Transitions to these two states must therefore be predominantly spin-flip transitions with possible small contributions from non-spin-flip components. A "soft giant dipole" resonance has been predicted [Suzuki, 1991] at low excitation energy, and the possible existence of such a resonance has been reported at about 6 MeV [Sakuta, 1994]. However,

the observed transition to the 5.6 MeV state is predominantly a spin-flip transition which contradicts such an interpretation. The broad resonance at excitation energy of 22.7 MeV has a coincidence to singles ratio of 48%. Therefore, the transition to this state must again be a pure spin-flip transition. The angular distributions of the cross sections to the states at 0.0 MeV and 1.9 MeV of figure 6.3 have been subjected to a DWBA analysis which is discussed in section 8.2.

E_x (MeV) (present work)	Γ (MeV) (FWHM) (present work)	E_x (MeV) [Ajzenberg-Selove,1988]	Γ (MeV) [Ajzenberg-Selove,1988]	J^π
gs		gs	$\tau_{1/2}$=806.7± 1.5 ms	0^+
1.93±0.03		1.797±0.025	0.113±0.02	(2^+)
5.6±0.3	12±1			
14.2±0.3	6.5±0.4	13.6±0.5	broad	$(1^-, 2^-)$
		15.5±0.5	4±2 MeV	
22.7±0.3	14±1	25±1	8±2 MeV	
		(32)	<2MeV	
		(36)	<2MeV	

Table 8.1 States in ^{6}He.

8.1.2 The $^{12}C(^7Li,^7Be)^{12}B$ reaction

The results of the present work are compared with known states in ^{12}B in table 8.2. The state at 2.2 MeV listed in table 6.2 is the sum of several low-lying discrete states which could not be resolved due to the finite resolution of the spectrograph. Therefore, this "state" is not listed in the table 8.2. The transition to the ^{12}B ground state is a pure spin-flip transition, since the spin and parities of the ground states of ^{12}C and ^{12}B are 0^+ and

1^+, respectively. The cross section ratio of coincidence to singles for this state, 42%, agrees within uncertainties with the ratio for a pure spin-flip transition, which is 47.2%. The state observed at 4.8 MeV corresponds to the known 2^- state at 4.5 MeV. The transition to this spin-dipole state is a spin-flip transition. The measured ratio of coincidence to singles for this state is 40% agrees with this. The state observed at excitation energy of 6.9 MeV could be the known giant dipole resonance (1^-) at 7.7 MeV. It was found that the spin dipole resonance is also situated at about the same excitation energy. The ratio of coincidence to singles for this state is 37%. This indicates that observed transition is comprised mostly of the spin dipole resonance, but seem also to contain small giant dipole resonance contributions. The ratio of the coincidence to singles for the state observed at 10.45 MeV is 16%, which indicates that this transition is mostly non-spin-flip with only small contributions from a spin-flip component. The state observed at excitation energy of 12.8 MeV has the coincidence to singles ratio of 53%. The ratio for pure spin-flip transition is 47.2%. This value is slightly higher than the maximum possible ratio due to the uncertainties of the cross sections. The angular distributions of the cross sections to the ground state of ^{12}B of figure 6.6 has been subjected to a DWBA analysis which is discussed in section 8.2.

E_x (MeV) (present work)	Γ (MeV) (FWHM) (present work)	E_x (MeV) [Ajzenberg-Selove,1990]	Γ (MeV) [Ajzenberg-Selove,1990]	J^π [Ajzenberg-Selove,1990]
gs		gs	$\tau_{1/2}$=20.20± 0.02 ms	1^+
4.84±0.04	0.65±0.02	4.46	broad	2^-
6.93±0.05	2.43±0.09	7.7	1.9±0.1	1^-
10.45±0.08	2.4±0.3	(11.08)		
12.8±0.02	10.8±0.3	(13.4±0.1)	broad	

Table 8.2 States in ^{12}B.

8.1.3 The $^{90}Zr(^{7}Li,^{7}Be)^{90}Y$ reaction

Table 8.3 gives the results of the present work for the states observed in ^{90}Y. The GT, SM, GD, SD, GQ and SQ denote the Gamow-Teller resonance, the spin monopole resonance, the isovector giant dipole resonance, the spin dipole resonance, the isovector giant quadrupole resonance and spin quadrupole resonance, respectively. The state observed at excitation energy of 3.5 MeV could correspond to the state observed at 2.7 MeV by other authors with the (n,p) reaction [Raywood, 1990; Conde, 1992]. The state at excitation energy of 6.1 MeV with energy width of 9.3 MeV could corresponds to a spin dipole resonance at 5.5 MeV reported by others [Raywood, 1990; Conde, 1992]. The giant dipole resonance was theoretically predicted at excitation energy of 5.9 MeV which agrees with the observed excitation energies. The state at 10.0 MeV corresponds to the spin dipole resonance at 10.0 MeV reported by other authors [Raywood, 1990; Conde, 1992]. A 2^+ giant quadrupole resonance and the 2^+ component of the spin quadrupole resonance were theoretically predicted at energies of 17.3 MeV and 17.5 MeV, respectively. A spin dipole resonance was reported experimentally [Conde, 1992] at the energy of 16.0 MeV which corresponds to the state observed at 16.1 MeV in the present work. This resonance could therefore be the spin-dipole resonance or a superposition of the predicted 2^+ giant quadrupole or the 2^+ component of the spin quadrupole resonance.

The coincidence to singles cross section ratios for the states at excitation energies of 3.5 MeV, 6.1 MeV, 10.0 MeV, and 16.1 MeV are 100%, 41%, 32%, and 19%, respectively. For heavier targets, the coincidence spectra contain not only the contributions from the 430 keV γ-rays from the deexcitation of ^{7}Be, but also the γ-rays from the deexcitaton of excited states in the residual nuclei. The γ-ray spectra of BGO detectors for heavier targets do in fact not display a strong photopeak of 430 keV γ-rays (see figure 5.6). Therefore, the cross section ratios of coincidence to singles do not provide reliable

information about spin-flip and non-spin-flip contributions to the cross sections for heavier targets.

E_x (MeV) (present work)	Γ (MeV) (FWHM) (present work)	E_x(MeV) [Conde,1992] (n,p)	E_x(MeV) [Raywood, 1990] (n,p)	E_x(MeV) [Auerbach, 1983,1984] (Theory)	J^π
3.5±0.4	3.1±0.5	2.7	2.7		(GT)
6.1±0.3	9.3±0.9	5.5	5.5		(SD)
				5.9	1^- (GD)
10.0±0.5	11±1	11.0	10.0	10.4	2^- (SD)
			15.5		1^+ (SM)
16.1±0.8	17±2	16.0			(SD)
				17.3	2^+ (GQ)
				17.5	2^+ (SQ)

Table 8.3 States in ^{90}Y.

8.1.4 The ^{120}Sn(^{7}Li,^{7}Be)^{120}In reaction

The resonances observed in ^{120}In are listed in table 8.4. Four resonances were observed, but three resonances at excitation energies of 1.12 MeV, 6.0 MeV and 11.5 MeV have not been observed before. The GM, GD and GQ in the last column denote the isovector giant monopole resonance, the isovector giant dipole resonance, and the isovector giant quadrupole resonance, respectively. The state at excitation energy of 1.12 MeV appears to be the giant dipole resonance, theoretically predicted to be at 1.2 MeV. The state at excitation energy of 11.5 MeV appears to be the giant quadrupole resonance predicted at this excitation energy. The state at 17.2 MeV is an isovector giant monopole resonance, theoretically predicted to be at 17.1 MeV. It was observed by several other authors [Berat, 1989, 1993; Erell, 1986; Krivine, 1980] at excitation energies from 14.7 to 18.5 MeV.

The ratios of coincidence to singles cross sections for the states at 1.12 MeV, 6.0 MeV, 11.5 MeV, and 17.2 MeV are 40%, 46%, 25%, and 53%, respectively. These ratios do not provide reliable information about spin-flip and non-spin-flip nature of the resonances due to the coincidence with the γ-rays from the deexcitations of the residual nucleus (see section 8.1.3).

The limited angular distributions shown in figure 6.10 for the transitions to the four states of table 8.4 have not been subjected to a DWBA analysis. However, the shapes seem to confirm transitions with small ΔL for the states at 1.12 MeV and 17.2 MeV in ^{120}In.

E_x (MeV) (present work)	Γ (MeV) (FWHM) (present work)	E_x(MeV) [Berat, 1989] (^{13}C,^{13}N)	E_x(MeV) [Erell, 1986] (π^-,π^0)	E_x(MeV) [Krivine, 1980]	E_x(MeV) [Auerbach, 1983,1984] (Theory)	J^π
1.12±0.09	1.3±0.2				1.2	1^- (GD)
6.0±0.2	5.2±0.7					
11.5±0.5	9.1±0.8				12.7	2^+ (GQ)
17.2±0.3	17±1	14.7	16.0	18.5	17.1	0^+ (GM)

Table 8.4 States in ^{120}In.

8.1.5 The ^{208}Pb(^{7}Li,^{7}Be)^{208}Tl reaction

The results of the present work together with the other published data are listed in table 8.5. The GM, SM, GD, SD, GQ, and SQ denote the isovector giant monopole resonance, the spin monopole resonance, the isovector giant dipole resonance, the spin dipole resonance, the isovector giant quadrupole resonance, and the spin quadrupole resonance, respectively. The state observed at 2.7 MeV may represent a superposition of the states predicted at excitation energies of 1.9 MeV, the giant dipole resonance, and 3.4

MeV, the spin dipole resonance. The resonance observed at 5.1 MeV corresponds to the resonance observed in the (n,p) reaction [Moinester, 1989]. The state observed at 8.4 MeV may represent a superposition of the 2^+ and 3^+ components of the spin quadrupole resonance, theoretically predicted at energies of 8.8 MeV and 8.3 MeV, respectively. The strongly excited state observed at excitation energy of 13.0 MeV seems to corresponds to a resonance observed at 13.6 MeV in (n,p) [Moinester, 1989]. It could represent the spin monopole resonance predicted at 13.5 MeV or the high-energy fragment of the giant monopole resonance. The spin monopole resonance was predicted to be at excitation energy of 13.5 MeV. The predictions for the giant monopole resonance display fragmentation with a low-energy fragment predicted at an excitation energy of about 6 MeV, and a high-energy fragment predicted at an excitation energy of about 14 MeV. It appears that the high-energy fragment of the giant monopole resonance has been seen in (^{13}C,^{13}N) reaction [Berat, 1993; Lhenry, 1994] at excitation energy of 16.5 MeV, and the low-energy fragment was seen in (π^-,π^0) reaction [Erell, 1986] at excitation energy of 7.0 MeV. It is not clear why no resonance is seen in the present work near 16.5 MeV, while another resonance is observed at 20 MeV.

The ratios of coincidence to singles cross sections for the states at the excitation energies of 0.0 MeV, 2.7 MeV, 5.1 MeV, 8.4 MeV, 13.0 MeV, and 20 MeV are 10%, 45%, 17%, 35%, 8%, and 28%, respectively. These ratios do not provide reliable information about the spin-flip and non-spin-flip components of the transitions since coincidence spectra contain the coincidence with the γ-rays from the deexcitation of the residual nucleus (see section 8.1.3).

E_x (MeV) (present work)	Γ (MeV) (FWHM) (present work)	E_x(MeV) [Moinester, 1989] (n,p)	E_x(MeV) [Berat, 1993] [Lhenry, 1994] (^{13}C,^{13}N)	E_x(MeV) [Auerbach,1983, 1984] (Theory)	J^π
				1.9	1^- (GD)
2.7±0.3	4.1±0.7				
				3.4	1^- (SD)
5.1±0.3	3.5±0.4	5.1			
				6.8	2^- (SD)
				7.1	(GQ)
8.4±0.4	3.9±0.4			8.3	3^+ (SQ)
				8.8	2^+ (SQ)
13.0±0.7	8.1±0.8	13.6		13.5	0^- (SM)
			16.5	11.3	0^+ (GM)
20±1	8.2±0.8				

Table 8.5 States in ^{208}Tl.

8.2 DWBA analysis

Differential cross sections for states in ^{6}He and ^{12}B were calculated using the fully microscopic, finite-range, distorted-wave approximation code FOLD [Cook, 1988] as described in chapter 7. The present calculations were performed with the 50 MeV and 100 MeV t-matrix interactions of Franey and Love [Love, 1981] and the modified M3Y interaction of F. Petrovich et al.[Petrovich, 1982]. The calculated cross sections for the M3Y interaction fits slightly better with the experimental cross sections and are shown below.

The spectroscopic amplitudes for the projectile systems and the target systems are calculated using the shell-model code OXBASH [Brown, MSUCL 524]. The Cohen-Kurath (8-16) POT (CKPOT), and Cohen-Kurath (6-16) two-body matrix element (CKI)

interactions were used to calculate the projectile and target transition densities [Cohen, 1965]. These Cohen-Kurath wave-functions consist of $1p_{3/2}$ and $1p_{1/2}$ orbits. The calculated spectroscopic amplitudes were different for the two interactions, but the structure of the angular distributions of the cross sections is similar. The calculations with CKI interaction agrees better with the experimental cross sections for the ground state of ^{6}He, while the calculations with CKPOT interaction fits better for the ground state of ^{12}B.

The Woods-Saxon radial wave-functions were calculated using the code WSAW based on a program by F. Petrovich. The single-particle binding energy for the $1p_{3/2}$ orbit was set to the separation energy of the experimental ground state, and that for the $1p_{1/2}$ orbit was assumed to be the experimental ground state separation energy minus the energy gap between the $1p_{3/2}$ and $1p_{1/2}$ orbits. The spin-orbit potential strength was taken as 7.0. The Wood-Saxon radial wave-functions, and therefore the calculated cross sections are very sensitive to the single-particle binding energies. It was found, for example, that the relative L=0 and L=2 contributions for the transition to the 2^+ state in ^{6}He changed by a factor of about 67 with a change in the binding energy for the $1p_{1/2}$ orbital in ^{6}He by only 1.8 MeV.

The optical model potentials are obtained from fitting elastic scattering data of the $^{12}C(^{7}Li,^{7}Li)^{12}C$ reaction at 350 MeV [Nadasen, 1995]. The following optical model parameters were used, V=107.8 MeV, r_0=0.749 fm, a_0=0.853 fm, W=37.9 MeV, r_w=0.911 fm, a_w=0.757 fm and r_c=0.654 fm. Here, $R_x=r_x\,(A_t^{1/3} + A_p^{1/3})$. The same optical model parameters were used for both entrance and exit channels in both reactions, $^{6}Li(^{7}Li,^{7}Be)^{6}He$ and $^{12}C(^{7}Li,^{7}Be)^{12}B$.

The angular distributions of the cross sections for the ground state of ^{6}He (0^+), the 1.9 MeV state in ^{6}He (2^+), and the ground state of ^{12}C (1^+) are shown in the figures 8.1, 8.2 and 8.3, respectively. The dashed curves are the components for all possible combinations of L, J_p and J_t, where L, J_p and J_t are the total angular momentum transfer to the relative motion, to the projectile system and to the target system, respectively. The

solid curve is the sum of all the possible combinations of L, J_p and J_t normalized to the experimental data. The normalization factors, N, are listed in tables 8.7(a) and 8.7(b).

The discussion of the normalization factors requires the knowledge of the calculated and experimental Gamow-Teller strengths B(GT). The B(GT) values extracted from the computer code FOLD differ by factors of 0.7 to 4.4 from the experimental B(GT) values. The experimental B(GT) values are extracted from the experimental log ft values of the respective β-decays using the equation [Chou, 1993]

$$ft = \frac{6139 \pm 7}{B(F) + (1.264 \pm 0.002)^2 B(GT)}. \qquad (8.1)$$

The log ft values for the β-decays $^{6}He_{gs}(0^+)$ -> $^{6}Li_{gs}(1^+)$, $^{7}Be_{gs}(3/2^-)$ -> $^{7}Li_{gs}(3/2^-)$, $^{7}Be_{ex}(1/2^-)$ -> $^{7}Li_{gs}(3/2^-)$, and $^{12}B_{gs}(1^+)$ -> $^{12}C_{gs}(0^+)$ are 2.910 ±0.002, 3.32, 3.55, and 4.066 ±0.002 [Ajzenberg-Selove, 1988, 1990], respectively. The log ft for $^{7}Be_{ex}(1/2^-)$ -> $^{7}Li_{gs}(3/2^-)$ was obtained from the mirror transition of $^{7}Be_{gs}(3/2^-)$ -> $^{7}Li_{ex}(1/2^-)$. The experimental and calculated B(GT) values and the ratio of (expt./calc.) are listed in tables 8.6(a) and 8.6(b). The calculated cross sections were then multiplied by the product of the ratios of B(GT)exp to B(GT)calc. for the target system and the projectile system $\left(\frac{B(GT)exp.}{B(GT)calc.}\right)_{projectile} \times \left(\frac{B(GT)exp.}{B(GT)calc.}\right)_{target}$, denoted by BGTPROD. The corrected cross sections were multiplied by an additional factor N to normalize to the experimental cross sections. Tables 8.7(a) and 8.7(b) give the values of BGTPROD and the normalization factor N for the calculations with CKI and CKPOT interactions, respectively.

	B(GT) exp.	B(GT) calc.	$\frac{B(GT)exp.}{B(GT)calc.}$
^{7}Li --> $^{7}Be_{gs}$	1.213±0.006	1.5855	0.7652
^{7}Li --> $^{7}Be_{ex}$	1.083±0.005	1.2840	0.8434
^{6}Li --> $^{6}He_{gs}$	1.58±0.01	0.3416	4.3577
^{12}C --> $^{12}B_{gs}$	0.990±0.009	0.6483	1.5274

Table 8.6(a) Experimental and calculated B(GT) for the CKI interaction.

	B(GT) exp.	B(GT) calc.	$\frac{B(GT)exp.}{B(GT)calc.}$
^{7}Li --> $^{7}Be_{gs}$	1.213±0.006	1.5545	0.7804
^{7}Li --> $^{7}Be_{ex}$	1.083±0.005	1.2375	0.8751
^{6}Li --> $^{6}He_{gs}$	1.58±0.01	0.4682	3.3655
^{12}C --> $^{12}B_{gs}$	0.990±0.009	0.6342	1.5613

Table 8.6(b) Experimental and calculated B(GT) for the CKPOT interaction.

	BGTPROD.	N
$^{6}Li(^{7}Li,^{7}Be_{gs})^{6}He_{gs}$	3.3344	0.6
$^{6}Li(^{7}Li,^{7}Be_{ex})^{6}He_{gs}$	3.6753	0.6

Table 8.7(a) Product of the ratios B(GT)exp/B(GT)calc. for the reaction and normalization factors for N the CKI interaction.

	BGTPROD.	N
$^{12}C(^{7}Li,^{7}Be_{gs})^{12}B_{gs}$	1.2185	1.4
$^{12}C(^{7}Li,^{7}Be_{ex})^{12}B_{gs}$	1.3663	1.4

Table 8.7(b) Product of the ratios B(GT)exp/B(GT)calc. for the reaction and normalization factors N for the CKPOT interaction.

The calculated angular distribution for the 1.9 MeV state (2^+) in ^{6}He is normalized to the experimental data without any correction for the B(GT) values, since it is not a pure Gamow-Teller transition. The normalization for this state was 2.0.

The angular distribution of the ^{6}He ground state of figure 8.1 has L = 0, L = 2 and L = 4 contributions to the cross section. The L = 4 contribution is not as significant as those for L = 0 and L = 2. The contribution from the transition ^{7}Li -> ^{7}Be$_{ex}$ is comparable to that from the ^{7}Li -> ^{7}Be$_{gs}$ transition. The experimental data for the ground state agree very well with the DWBA calculations. The minima in the highly diffractive L = 0 contributions are filled in by L = 2 contributions. The result confirms the 0^+ spin-parity assignment of the ^{6}He ground state.

The angular distribution of the 1.9 MeV state is compared in figure 8.2 with the DWBA calculations for this 2^+ state. The first excited state in ^{6}He has spin and parity of 2^+, situated at the excitation energy of 1.797 ± 0.025 MeV [Ajzenberg-Selove, 1988]. The distribution is mainly from the L = 2 terms. The spectroscopic amplitudes lead to L = 2 contributions which dominate strongly over the L = 0 contributions at all the angles. The L = 4 and L = 6 contributions to the cross section become significant for the angles above θ_{cm} = 8. The calculated angular distribution falls off with increasing angle more rapidly than the experimental distribution. This behavior is not understood, but may be related to the sensitivity of the various contributions to the binding energies of the transferred nucleons.

The calculated angular distribution of the ^{12}B ground state shown in figure 8.3 is mainly from the L = 0 and L = 2 terms with minor contributions from the L = 4 term. The calculated distribution agrees very well with the experimental data confirming the 1^+ spin and parity of the ground state. It is for this reason that it was felt justified to renormalize all other small-angle points based on the calculated angular distribution.

The experimental angular distributions of the cross sections for the other states in ^{6}He and ^{12}B will be analyzed and published at a later date.

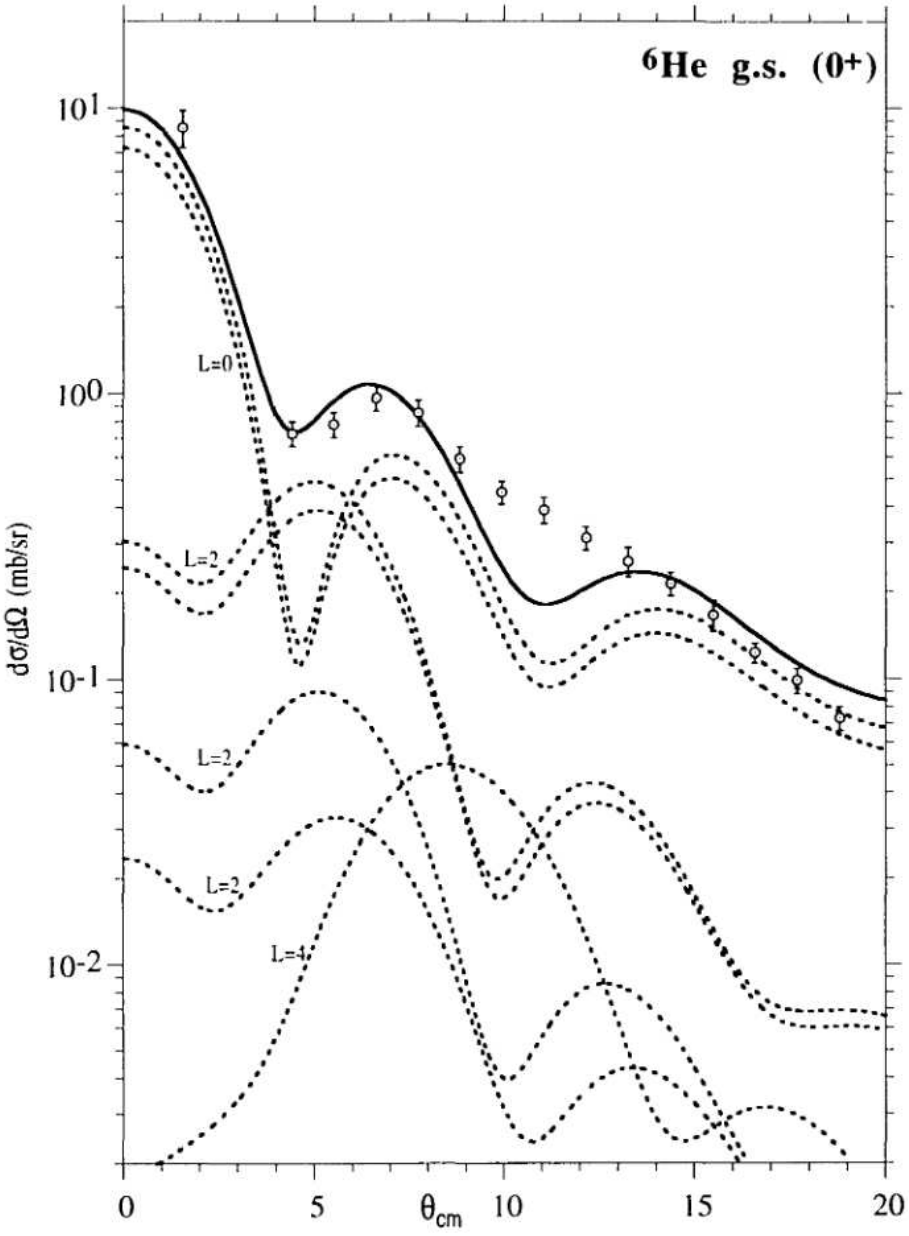

Figure 8.1 Angular distribution of the cross sections of the ground state of ^{6}He.

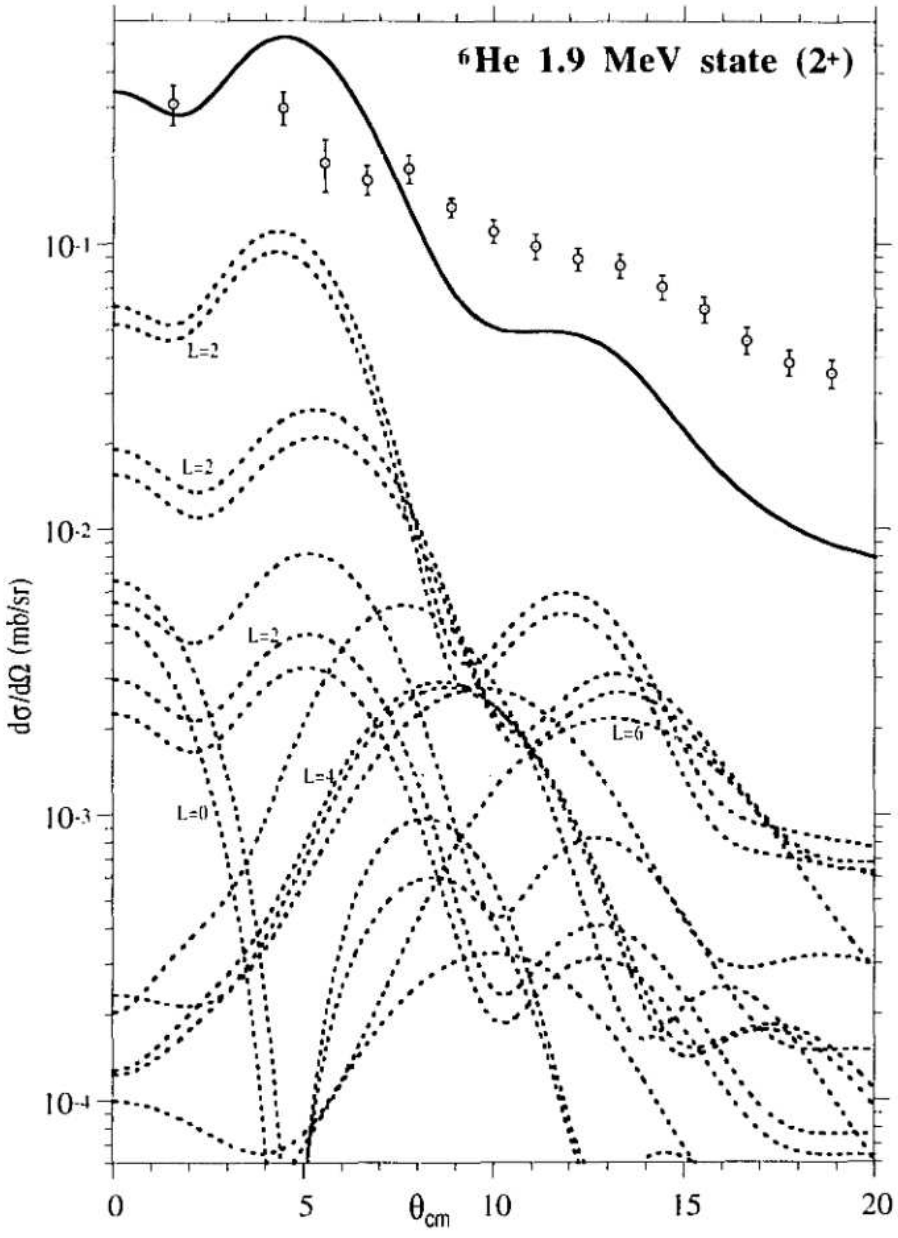

Figure 8.2 Angular distribution of the cross sections of the 2^+ state in ^{6}He.

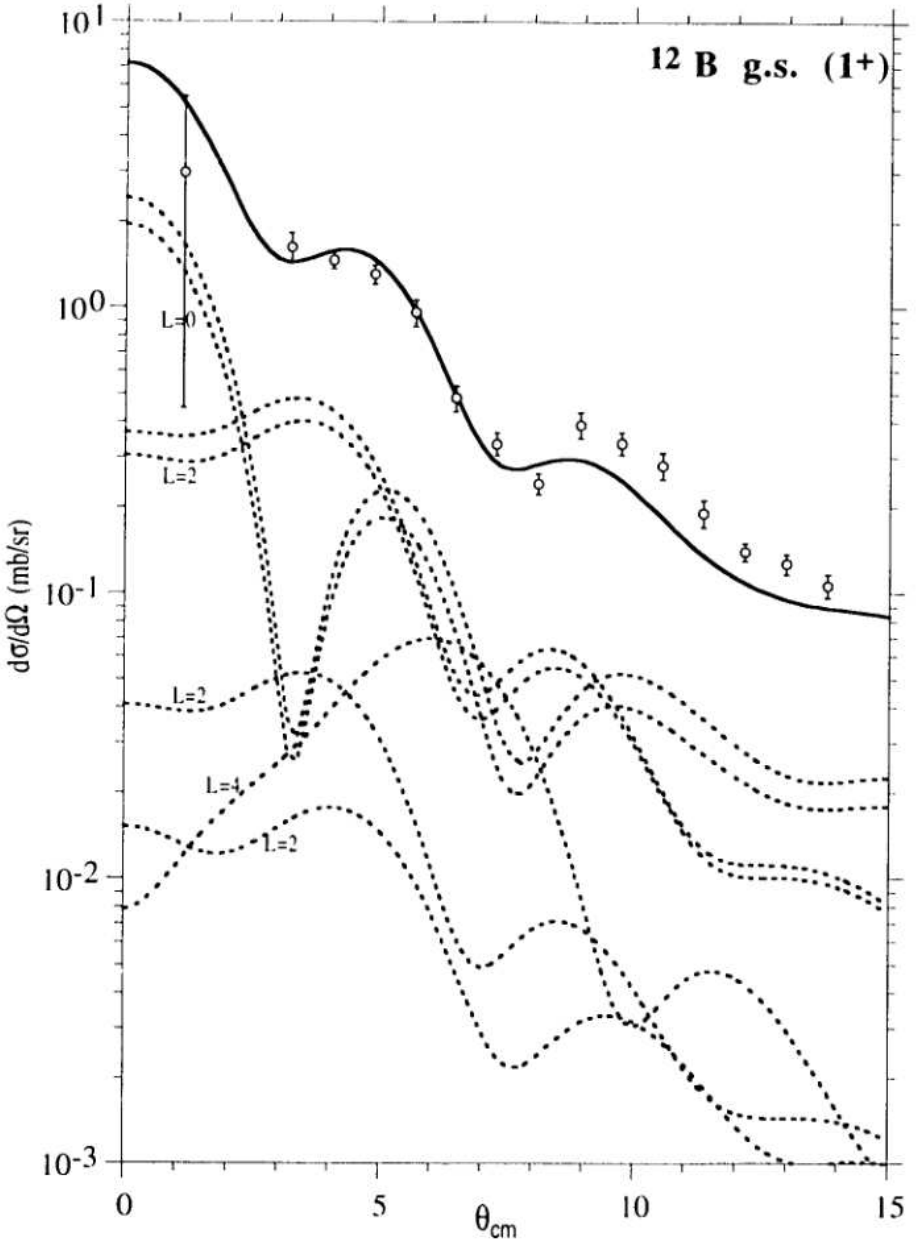

Figure 8.3 Angular distribution of the cross sections of the ground state of ^{12}B.

CHAPTER 9

CONCLUSIONS

The present work describes an investigation of isovector giant resonances using (^{7}Li,^{7}Be) charge-exchange reactions at 50 MeV/u. Charge-exchange reactions selectively excite isovector resonances. Therefore, (^{7}Li,^{7}Be) charge-exchange reactions are useful spectroscopic tools to investigate isovector giant resonances.

Transitions to several discrete states and 20 giant resonances were observed in the nuclei ^{6}He, ^{12}B, ^{90}Y, ^{120}In, and ^{208}Tl. Only about 13 of these resonances have been seen in other charge-exchange reactions, and at most 12 of the resonances observed in the present work seem to correspond to theoretically predicted resonances. The new resonance observed in ^{6}He at 5.6 MeV is of special interest because a "soft giant dipole resonance" with $J^{\pi} = 1^{-}$ has been predicted for this "neutron-halo" nucleus at low excitation energy. However, it was observed in the present work that the transition to this resonance displays spin-flip characteristics which contradicts such an interpretation. Furthermore, the angular distribution for this transition resembles that for the transition to the ground state of ^{6}He which therefore favors a $J^{\pi} = 0^{+}$ assignment. Angular distributions of the cross sections for the transitions to states in ^{6}He and ^{12}B were measured. Selected angular distributions were compared with theoretical predictions using the fully microscopic, finite-range, distorted-wave-Born-approximation code FOLD. Excellent agreement was observed for the transitions to the ground states of ^{6}He and ^{12}B.

The spin-flip and the non-spin-flip components of giant resonances can be extracted by detecting the ^{7}Be ejectile in coincidence with the 430 keV Doppler-shifted γ-rays from decay in flight of the excited ^{7}Be. The cross section ratios obtained for coincidence and

singles events provides a signature for the spin-flip characteristics of the observed resonances. However, this procedure was possible only for the light targets, because excitations of the residual nuclei for the heavier targets produced additional γ-rays. BGO detectors are also sensitive to neutrons which can interfere with the detection of the 430 keV γ-rays. The measured coincidence spectra for the light targets represent transitions with $\Delta S = 1$. Spectra for $\Delta S = 0$ can in principle be extracted. This was not done, though, in the present work due to limited statistics. Future use of γ-ray detectors with low neutron detection efficiency or the capability of neutron-γ pulse-shape discrimination will eliminate the interference with neutrons.

The use of neutron detectors which permit pulse-shape discrimination between neutrons and γ-rays will be useful to investigate giant resonances due to several reasons: (1) giant resonances decay via neutron emission; therefore, detecting the ^{7}Be in coincidences with neutrons will provide information about the resonances such as the excitation energies, widths, and the cross sections; (2) low-lying discrete states below the neutron threshold will not appear in the neutron-coincidence spectra. Furthermore, the non-resonant background will be reduced when coincidences with neutrons are required. Therefore, the cross sections and the parameters of giant resonances can be obtained with improved precision.

All ^{7}Be spectra show a hydrogen peak due to hydrogen contamination of the targets. It is therefore desirable to use targets with reduced hydrogen contamination. Special care has been taken to manufacture the targets for the experiments #93018-1 and #93018-2 to reduce hydrogen (water) contamination. The spectra in those experiments show indeed less hydrogen contamination and therefore they have less uncertainties due to the subtraction of hydrogen.

The S320 medium-resolution magnetic spectrograph has an energy resolution of only about 1.5 MeV. Therefore some of the low-lying states in the residual nuclei could

not be resolved. Future work will make use of the S800 high-resolution magnetic spectrograph now under construction.

BIBLIOGRAPHY

BIBLIOGRAPHY

[Ajzenberg-Selove, 1988] F. Ajzenberg-Selove, Nucl. Phys. A490(1988)1.

[Ajzenberg-Selove, 1990] F. Ajzenberg-Selove, Nucl. Phys. A506(1990)75.

[Annakkage, 1994] T. N. Annakkage, J. Jänecke, K. Pham, D. A. Roberts, G. P. A. Berg and J. S. Winfield, Nucl. Instr. and Meth. A353(1994)24.

[Antony, 1988] M. S. Antony, J. Britz and A. Pape, Atomic Data And Nuclear Data Tables 40(1988)9.

[Auerbach, 1983, 1984] N. Auerbach and A. Klien, Phy. Rev. C30(1984)1032, Nucl. Phys. A395(1983)77, Phy. Rev. C27(1983)1818, Phy. Rev. C28(1983)2075.

[Baldwin, 1947] G. C. Baldwin and G. S. Klaiber, Phys. Rev. 71(1947)3.

[Baldwin, 1948] G. C. Baldwin and G. S. Klaiber, Phys. Rev. 73(1948)1156.

[Berat, 1989] C. Berat, M. Buenerd, J. Chauvin, J. Y. Hostachy, D. Lebrun, P. Martin, J. Barrette, B. Berthier, B. Fernandez, A. Miczaika, W. Mittig, E. Stiliaris, W. von Oertzen, H. Lenske and H. H. Wolter, Phys. Lett. B218(1989)299.

[Berat, 1993] C. Berat, M. Buenerd, J. Y. Hostachy, P. Martin, J. Barrette, B. Bertheier, B. Fernandez, A. Miczaika, A. Villari, H. G. Bohlen, S. Kubono, E. Stiliaris and W. von Oertzen, Nucl. Phys. A555(1993)455.

[Blomgren, 1991] J. Blomgren, Ph. D. thesis, Uppsala University, Sweden (1991).

[Bohlen, 1988] H. G. Bohlen, B. Gebauer, D. Kolbert, S. Kubono, W. von Oertzen, P. O. Pellegrin, E. Stiliaris, M. Wilpert, T. Wilpert, H. Lenske, H. H. Wolter, A. Miczaika, N. Alamanos, J. Barrette, B. Berthier, B. Fernandez, C. Berat, M. Buenerd, J. Y. Hostachy, P. Martin and W. Mittig, Nucl. Phys. A488(1988)89c.

[Brady, 1983] F. Brady, G. A. Needham, J. L. Romero, C. M. Castaneda, T. D. Ford, J. L. Ullmann and M. L. Webb, Phys. Rev. Lett. 51(1983)1320.

[Brown, MSUCL 524] B. A. Brown, A. Etchegoyen and W. D. M. Rae, MSUCL report number 524 (unpublished).

[Chou,1993] W. T. Chou, E. K. Warburton and B. A. Brown, Phys. Rev. C47(1993)163.

[Cohen, 1965] S. Cohen and D. Kurath, Nucl. Phys. 73(1965)1.

[Cook, 1984] J. Cook, K. W. Kemper, P. V. Drumm, L. K. Fifield, M. A. C. Hotchkis, T. R. Ophel and C. L. Woods, Phys. Rev C30(1984)1538.

[Cook, 1988] J. Cook and J. A. Carr, computer program FOLD, Florida State University, 1988 (unpublished); this is based on the code originally used in [Pertovich,1977], modified as described in [Cook, 1984], with additions to handle the Wood-Saxon radial wave-functions.

[Erell, 1986] A. Erell, J. Alster, J. Lichtenstadt, M. A. Moinester, J. D. Bowman, M. D. Cooper, F. Irom, H. S. Matis, E. Piasetzky and U. Sennhauser, Phys. Rev. C34(1986)1822.

[Fox, 1985] R. Fox, R. Au, A. Van der Molen, B. Pollack, T. Glynn, IEEE Trans. on Nucl. Sci. NS-32 #4 (1985)1286.

[Fox, 1989] R. Fox, R. Au, A. Van der Molen, IEEE Trans. on Nucl. Sci. NS-36 #5 (1989)1562.

[Gareev, 1988] F. A. Gareev, Y. A. Glukhov, S. A. Goncharov, V. V. Danichev, A. S. Dem'yanova, S. N. Ershov, G. S. Kazacha, A. A. Ogloblin, N. I. Pyatov, S. B. Sakuta and S. A. Fayans, Sov. J. Nucl. Phys. 48(1988)773.

[Goldhaber, 1948] M. Goldhaber and E. Teller, Phys. Rev. 74(1948)1046.

[Goodman, 1980] C. D. Goodman, "The (p,n) reaction and the nucleon-nucleon force" (eds. C. D. Goodman, S. M. Austin, S. D. Bloom, J. Rapaport and G. R. Satchler), Plenum Press (1980).

[Goodman, 1981] C. D. Goodman, Comm. Nucl. Part. Phys. 10(1981)117.

[Harakeh, 1977] M. N. Harakeh, K. van der Borg, T. Ishimatsu, H. P. Morsch, A. van der Woude and F. E. Bertrand, Phys. Rev. Lett. 38(1977)676.

[Häusser, 1983] O. Häusser, M. A. Lone, T. K. Alexander, S. A. Kushneriuk and J. Gascon, Nucl. Instr. and Meth. 213(1983)301.

[Haxel, 1949] O. Haxel, J. H. D. Jensen, and H. E. Suess, Phys. Rev. 75(1949)1766.

[Haxel, 1950] O. Haxel, J. H. D. Jensen, and H. E. Suess, Z. Phys. 128(1950)295.

[Jury, 1979] J. W. Jury, B. L. Berman, D. D. Faul, P. Meyer, K. G. McNeill and J. G. Woodworth, Phys. Rev. C19(1979)1684.

[Krivine,1980] H. Krivine, J. Treiner and O. Bohigas, Nucl. Phys. A336(1980)155.

[Lewis, 1972] M. B. Lewis and F. E. Bertrand, Nucl. Phys. A196(1972)337.

[Lhenry, 1994] I. Lhenry, D. Beaumel, S. Fortier, S. Gales, H. Laurent, J. M. Maison, F. Azaier, Y. Blumenfeld, J. Guillot, H. Langevin-Joliot, T. Suomijarvi, G. M. Crawley, J. Finck and J. Stasko, Nouvelles du GANIL No 52 (1994).

[Love, 1981] W. G. Love and M. A. Franey, Phys. Rev. C24(1981)1073.

[Mayer, 1948] M. G. Mayer, Phys. Rev. 74(1948)235.

[Mayer, 1949] M. G. Mayer, Phys. Rev. 75(1949)1969.

[Mayer, 1950] M. G. Mayer, Phys. Rev. 78(1950)16.

[Moinester, 1989] M. A. Moinester, A. Trudel, K. Raywood, S. Yen, B. M. Spicer, R. Abegg, W. P. Alford, N. Auerback, A. Celler, D. Frekers, O. Hausser, R. L. helmer, R. Henderson, K. H. Hicks, K. P. Jackson, R. G. Jeppesen, N. S. P. King, S. Long, C. A. Miller, M. Vetterli, J. Watson and A. I. Yavin, Phys. Lett. B230(1989)41.

[Nadasen, 1995] A. Nadasen, J. brusoe, J. Farhat, T. Stevens, J. Williams, J. S. Winfield, R. E. Warner, F. D. Becchetti, J. W. Jänecke, T. Annakkage, D. Roberts, J. Bajema and H. S. Govinden, Phys. Rev. C(1995).

[Nakayama, 1990, 1987] S. Nakayama, T. Yamagata, K. Yuasa, M. Tanaka, M. Inoue, T. Itahashi and H. Ogata, Phys. Lett. B246(1990)342, Phys. Lett. B195(1987)316.

[Nakayama, 1990] S. Nakayama, T. Yamagata, K. Yuasa, M. Tanaka, H. G. Bohlen, H. Lenski, H. H. Wolter, M. Inoue, T. Itahashi and H. Ogata, Nucl. Phys. A507(1990)515.

[Nakayama, 1991] S. Nakayama, T. Yamagata, M. Tanaka, M. Inoue, K. Yuasa, T. Itahashi, H. Ogata, N. Koori and K. Shima, Nucl. Instr. and Meth. A302(1991)472.

[Nakayama, 1992] S. Nakayama, T. Yamagata, M Tanaka, M. Inoue, K. Yuasa, T. Itahashi, H. Ogata, N. Koori, K. Shima and M. B. Greenfield, Phys. Rev. C46(1992)1667, Nucl. Phys. A538(1992)627c.

[Perey, 1976] C. M. Perey and F. G. Perey, Atomic Data And Nuclear Data Tables, 17(1976)3.

[Petrovich, 1977] F. Petrovich and D. Stanley, Nucl. Phys. A275(1977)487.

[Petrovich, 1984] F. Petrovich, R. J. Philpott, A. W. Carpenter and J. A. Carr, Nucl. Phys. A425(1984)609.

[Pitthan, 1971] R. Pitthan and T. Walcher, Phys. Lett. 36B(1971)563.

[Raywood, 1990] K. J. Raywood, B. M. Spicer, S. Yen, S. A. Long, M. A. Moinester, R. Abegg, W. P. Alford, A. Celler, T. E. Drake, D. Frekers, P. E. Green, O. Hausser, R. L. Helmer, R. S. Henderson, K. H. Hicks, K. P. Jackson, R. G. Jeppesen, J. D. King, N. S. P. King, C. A. Miller, V. C. Officer, R. Schubank, G. G. Shute, M. Vetterli, J. Watson and A. I. Yavin, Phys. Rev. C41(1990)2836.

[Roberts, 1994] D. Roberts, Private communication (1994).

[Sakuta, 1994] S. B. Sakuta, A. A. Ogloblin, O. Y. Osadchy, Y. A. Glukhov, S. N. Ershov and F. A. Gareev, Europhysics Letters (1994).

[Satchler, 1983] R. G. Satchler,"Direct Nuclear Reactions", Clarendon Press (1983).

[Steinwedel, 1950] H. Steinwedel and J. H. D. Jensen, Z. Naturforschung 5a(1950)413.

[Sterrenburg, 1980] W. A. Sterrenburg, S. M. Austin, R. P. DeVito and A. Galonsky, Phys. Rev. Lett. 45(1980)1839.

[Suzuki, 1991] Y. Suzuki, Nucl. Phys. A528(1991)395.

[Van der Woude, 1987] A. Van der Woude, Prog. Part. Nucl. Phys. 18(1987)217.

[Weizsäcker, 1935] C. F. Weizsäcker, Z. Phys. 96(1935)431.

[Winfield, 1992] J. S. Winfield and H. van der Plich, "The S320 spectrograph manual", NSCL (1992).

[Winfield, 1994] J. Winfield, D. J. Morrissey and J. Kelley, "The A1200 users manual", NSCL (1994).

[XSYS, 1988] IUCF internal report, 1988. The original version was developed at Triangle Universities Nuclear Laboratory (1998).

[Youngblood, 1977] D. E. Youngblood, C. M. Rosza, J. M. Moss, D. R. Brown and J. D. Bronson, Phys. Rev. Lett. 39(1977)1188.

[Youngblood, 1978] D. E. Youngblood, C. M. Rosza, J. M. Moss, D. R. Brown and J. D. Bronson, Phys. Rev. C15(1978)1644.